Research Paper

GEOSPHERE

GEOSPHERE; v. 13, no. 2

doi:10.1130/GES01428.1

31 figures; 3 tables; 3 supplemental files

CORRESPONDENCE: gav4@buffalo.edu

CITATION: Valentine, G.A., Cortés, J.A., Widom, E., Smith, E.I., Rasoazanamparany, C., Johnsen, R., Briner, J.P., Harp, A.G., and Turrin, B., 2017, Lunar Crater volcanic field (Reveille and Pancake Ranges, Basin and Range Province, Nevada, USA): Geosphere, v. 13, no. 2, p. 391–438, doi:10.1130/GES01428.1.

Received 12 September 2016
Revision received 15 November 2016
Accepted 3 January 2017
Published online 24 February 2017

Lunar Crater volcanic field (Reveille and Pancake Ranges, Basin and Range Province, Nevada, USA)

Greg A. Valentine[1], Joaquín A. Cortés[2,3], Elisabeth Widom[4], Eugene I. Smith[5], Christine Rasoazanamparany[4], Racheal Johnsen[5], Jason P. Briner[1], Andrew G. Harp[1], and Brent Turrin[6]

[1]Department of Geology, 126 Cooke Hall, University at Buffalo, Buffalo, New York 14260, USA
[2]School of Geosciences, The Grant Institute, The Kings Buildings, James Hutton Road, University of Edinburgh, Edinburgh, EH 3FE, UK
[3]School of Civil Engineering and Geosciences, Newcastle University, Newcastle, NE1 7RU, UK
[4]Department of Geology and Environmental Earth Science, Shideler Hall, Miami University, Oxford, Ohio 45056, USA
[5]Department of Geoscience, 4505 S. Maryland Parkway, University of Nevada Las Vegas, Las Vegas, Nevada 89154, USA
[6]Department of Earth and Planetary Sciences, 610 Taylor Road, Rutgers University, Piscataway, New Jersey 08854-8066, USA

ABSTRACT

The Lunar Crater volcanic field (LCVF) in central Nevada (USA) is dominated by monogenetic mafic volcanoes spanning the late Miocene to Pleistocene. There are as many as 161 volcanoes (there is some uncertainty due to erosion and burial of older centers); the volumes of individual eruptions were typically ~0.1 km³ and smaller. The volcanic field is underlain by a seismically slow asthenospheric domain that likely reflects compositional variability relative to surrounding material, such as relatively higher abundances of hydrous phases. Although we do not speculate about why the domain is in its current location, its presence likely explains the unusual location of the LCVF within the interior of the Basin and Range Province. Volcanism in the LCVF occurred in 4 magmatic episodes, based upon geochemistry and ages of 35 eruptive units: episode 1 between ca. 6 and 5 Ma, episode 2 from ca. 4.7 to 3 Ma, episode 3 between ca. 1.1 and 0.4 Ma, and episode 4, ca. 300 to 35 ka. Each successive episode shifted northward but partly overlapped the area of its predecessor. Compositions of the eruptive products include basalts, tephrites, basanites, and trachybasalts, with very minor volumes of trachyandesite and trachyte (episode 2 only). Geochemical and petrologic data indicate that magmas originated in asthenospheric mantle throughout the lifetime of the volcanic field, but that the products of the episodes were derived from unique source types and therefore reflect upper mantle compositional variability on spatial scales of tens of kilometers. All analyzed products of the volcanic field have characteristics consistent with small degrees of partial melting of ocean island basalt sources, with additional variability related to subduction-related enrichment processes in the mantle, including contributions from recycled ocean crust (HIMU source; high-μ, where μ = $^{238}U/^{204}Pb$) and from hydrous fluids derived from subducted oceanic crust (enriched mantle, EM source). Geochemical evidence indicates subtle source heterogeneity at scales of hundreds of meters to kilometers within each episode-scale area of activity, and temporary ponding of magmas near the crust-mantle boundary. Episode 1 magmas may have assimilated Paleozoic carbonate rocks, but the other episodes had little if any chemical interaction with the crust. Thermodynamic modeling and the presence of amphibole support dissolved water contents to ~5–7 wt% in some of the erupted magmas. The LCVF exhibits clustering in the form of overlapping and colocated monogenetic volcanoes that were separated by variable amounts of time to as much as several hundred thousand years, but without sustained crustal reservoirs between the episodes. The persistence of clusters through different episodes and their association with fault zones are consistent with shear-assisted mobilization of magmas ponded near the crust-mantle boundary, as crustal faults and underlying ductile deformation persist for hundreds of thousands of years or more (longer than individual episodes). Volcanoes were fed at depth by dikes that occur in en echelon sets and that preserve evidence of multiple pulses of magma. The dikes locally flared in the upper ~10 m of the crust to form shallow conduits that fed eruptions. The most common volcanic landforms are scoria cones, agglomerate ramparts, and 'a'ā lava fields. Eruptive styles were dominantly Strombolian to Hawaiian; the latter produced tephra fallout blankets, along with effusive activity, although many lavas were likely clastogenic and associated with lava fountains. Eroded scoria cones reveal complex plumbing structures, including radial dikes that fed magma to bocas and lava flows on the cone flanks. Phreatomagmatic maar volcanoes compose a small percentage of the landform types. We are unable to identify any clear hydrologic or climatic drivers for the phreatomagmatic activity; this suggests that intrinsic factors such as magma flux played an important role. Eruptive styles and volumes appear to have been similar throughout the 6 m.y. history of the volcanic field and across all 4 magmatic episodes. The total volume and time-volume behavior of the LCVF cannot be precisely determined by surface observations due to erosion and burial by basin-fill sediments and subsequent eruptive products. However, previous estimates of a total volume of 100 km³ are likely too high by a factor of ~5, suggesting an average long-term eruptive flux of ~3–5 km³/m.y.

INTRODUCTION

Intraplate volcanism has long been a topic of research focused on basalt petrogenesis and upper mantle composition and structure, due to relatively low degrees of crustal overprinting on geochemical signatures and, in many cases, abundant mantle xenoliths (e.g., Wörner et al., 1986; Farmer et al., 1989;

Lum et al., 1989; Menzies, 1989; Luhr et al., 1995; Witt-Eickschen and Kramm, 1998; Gazel et al., 2012; Cousens et al., 2013; McGee and Smith, 2016). A growing body of literature in the past decade has also focused on physical processes of intraplate volcanoes, including magma ascent, relationships with crustal structure, and eruption (see reviews by Valentine and Gregg, 2008; Németh, 2010; Le Corvec et al., 2013a, 2013b; integrated case studies by Le Corvec et al., 2013c; Murcia et al., 2016). Recent work has been partly aimed at assessing the potential hazards associated with eruptions in monogenetic volcanic fields (e.g., Ort et al., 2008; Valentine and Perry, 2009; Houghton et al., 2006; Németh et al., 2012), but also has been driven by the increasing recognition of the complexity of these small volcanoes, which were traditionally thought to be simple and well understood (e.g., Houghton and Schmincke, 1986; Ort and Carrasco-Nuñez, 2009; Genareau et al., 2010; Martí et al., 2011; Bolós et al., 2012; van Otterloo et al., 2013; Pedrazzi et al., 2016).

Several fundamental questions arise in the study of intraplate, dominantly monogenetic, volcanic fields. (1) Are the mantle magma sources homogeneous or are they heterogeneous in time and space for a given field? (2) Are there relationships between magma sources, clusters, and preexisting crustal structures, and why? (3) What are the characteristics of the transition from crustal magma transport, mainly via dikes, to eruptions at the surface? (4) How do individual volcanoes grow and feed various eruptive processes? (5) Are there relationships between source characteristics and the scales and eruptive styles of individual volcanoes, and the time-volume behavior of the volcanic field? Here we report an integrated study of the late Miocene–Pleistocene Lunar Crater volcanic field (LCVF) in central Nevada (USA) that is aimed at exploring these general questions. We present new geologic maps of the field, build upon previous geochronological and petrogenetic studies including a reassessment of mantle sources through time and space, and summarize the time-space distribution of volcanism, relationships with crustal structures, hypabyssal plumbing of the volcanoes, volcano types, and eruptive styles. We interpret data related to these individual aspects of the volcanic field, and conclude by interpreting relationships between them where such can be defined. We also briefly summarize the evolution of the volcanic landscape over several million years, and then compare the LCVF with nearby volcanic fields.

Monogenetic volcanism is defined differently, so we first clarify our terminology. Consistent with Valentine and Connor (2015), we use the term monogenetic for volcanoes that have only one eruptive episode, after which they become extinct. An eruptive episode may span time scales of weeks to decades (see Wood, 1980; Luhr and Simkin, 1993). A monogenetic event encompasses any processes within a given eruptive episode. Our definition has no implications regarding the volume, number, or composition of magma batches that might feed a monogenetic event. Many eruptions, in the sense of individual explosions or periods of sustained activity of a given style (e.g., fountaining, effusion), typically occur within the context of a monogenetic eruptive episode; thus our definition does not imply a single eruptive process. We distinguish between volcanoes, also referred to as centers, and vents. An individual volcano can have multiple vents during a single monogenetic eruptive episode. An additional issue that sometimes arises in the literature is how to distinguish monogenetic volcanoes from polygenetic volcanoes that undergo multiple eruptive episodes separated by dormant periods (e.g., Németh, 2010). This distinction can be ambiguous because in a volcanic field there is always a chance that a new monogenetic volcano will form within the footprint of a previous one; as described herein, this is especially common where the volcanoes form dense, long-lived clusters. In our view, polygenetic volcanism typically requires a single sustained magma plumbing system in the crust that produces multiple eruptive episodes. Thus in the absence of petrologic evidence for sustained magma reservoirs shared by colocated centers of different ages, we assume that colocated volcanoes are simply overlapping monogenetic volcanoes. We understand that at some point the distinction between monogenetic and polygenetic volcanism is rather subjective, but this issue has no impact on the work presented here. We also distinguish eruptive episodes at individual volcanoes from magmatic episodes on the scale of the volcanic field. In the case of the LCVF we have identified four major magmatic episodes, each of which includes many monogenetic volcanoes. These large-scale episodes are each characterized by a specific range of volcano ages and by similar magma compositions.

REGIONAL CONTEXT

The interior of the western United States is dotted with intraplate volcanic fields (Fig. 1) that individually contain between one and a few hundred Quaternary monogenetic volcanoes. Most of these fields are located near the edges of the actively extending Basin and Range Province (e.g., Smith and Luedke, 1984; Parsons, 1995), such as along the margin of the stable cratonic block that forms the Colorado Plateau, along the eastern front of the Sierra Nevada (California), or in the Rio Grande Rift (an eastern extension of Basin and Range).

The LCVF is relatively isolated from other major volcanic fields and is centrally located within the Basin and Range Province. Prior to the basaltic volcanism that is our focus, the area underwent voluminous ignimbrite-forming eruptions during the Oligocene to early Miocene, associated with the central Nevada caldera complex, and subsequent basaltic andesitic volcanism that continued through the mid-Miocene (Best et al., 2013, 2016). These older volcanic rocks are underlain by a thick sequence of Paleozoic carbonate and clastic sediments; the crystalline basement is Proterozoic in age (Menzies, 1989). Extensional tectonics, accompanied by formation of north- to north-northeast–trending Basin and Range topography, has been active since the Oligocene. Crustal thickness is ~30–35 km, similar to most of the Basin and Range Province, but heat flow in the area of the LCVF is relatively low (<62 mW/m^2, the so-called Eureka low; Thompson and Burke, 1974; Sass et al., 1994; Parsons, 1995). The lithosphere beneath the LCVF is estimated to be 60–75 km thick (Li et al., 2007; Levander and Miller, 2012). High-resolution P and S wave tomography of the western United States by the transportable array component of the EarthScope USArray (www.usarray.org/) provides an image of the upper

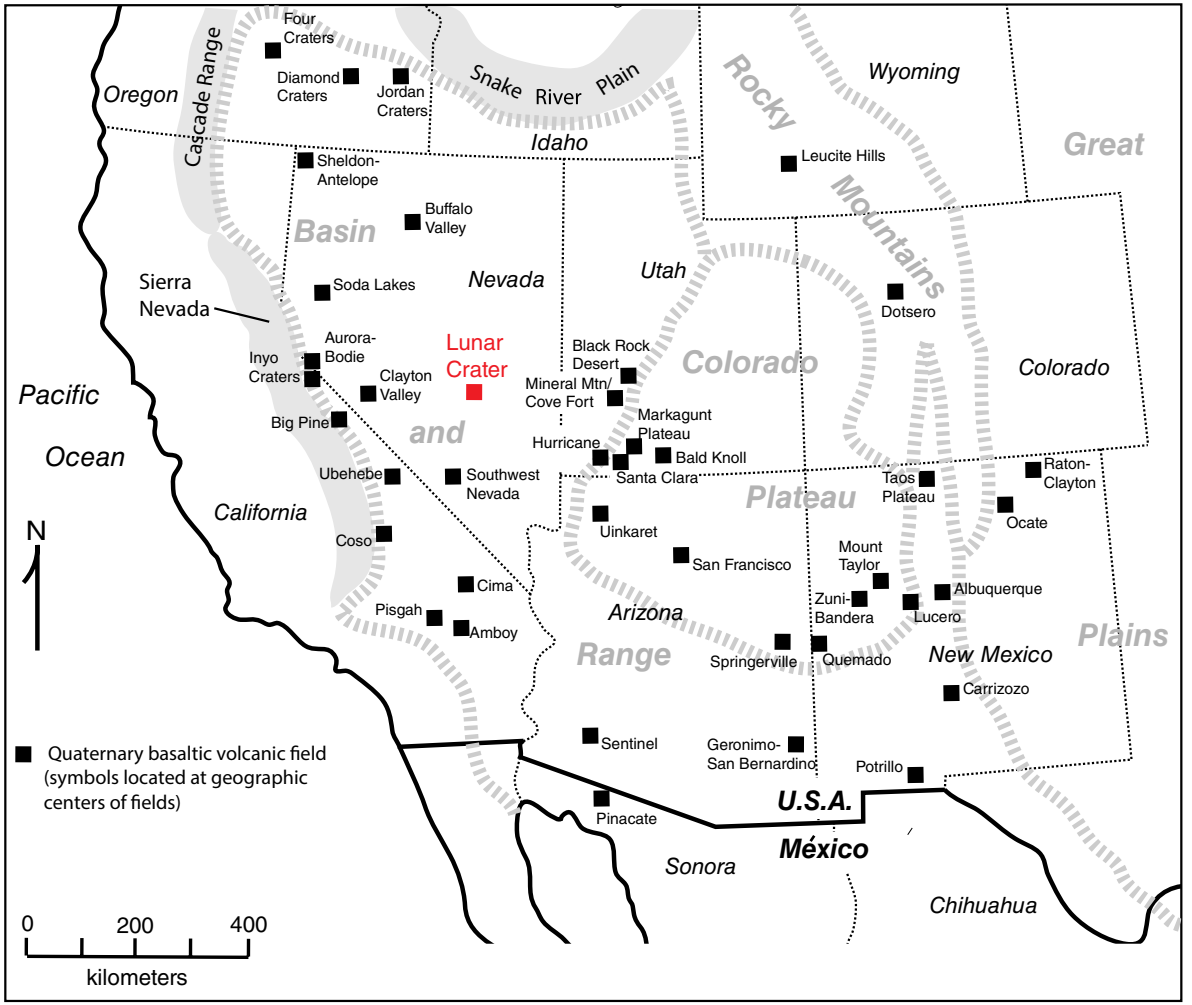

Figure 1. Simplified map of the southwestern United States showing locations and names of intraplate volcanic fields that have been active during the Quaternary. Not included are arc-related (Cascade Range) fields or those related to the Yellowstone hotspot track (Snake River Plain). Lunar Crater volcanic field is highlighted in red. Dashed lines outline geographic provinces that host the volcanic fields (Basin and Range, Colorado Plateau, Rocky Mountains, and Great Plains).

mantle in the region (Schmandt and Lin, 2014). A profile through the youngest part of the LCVF (Fig. 2) indicates that the field is underlain by a domain of relatively slow upper mantle, suggesting the presence of some melt due to upwelling and/or volatile enrichment; the relatively low heat flow at the LCVF leads us to favor the latter. The slowest part of this domain correlates well with estimated melting depths for Pleistocene LCVF volcanoes (Cortés et al., 2015). Although we do not speculate about why the domain is in its current location, its presence likely explains the unusual location of the volcanic field within the interior of the Basin and Range Province.

LCVF

Most of the LCVF is expressed on the surface as an ~90-km-long, ~5–15-km-wide belt of volcanoes exposed on and around two mountain ranges (Fig. 3, but see following discussion about the field boundaries). The older late Miocene–Pliocene part of the field is mainly in the Reveille Range and adjacent Kawich Valley (Fig. 4), and the younger Pliocene–Pleistocene part extends northeastward into the Pancake Range (Fig. 5). Note that the name Pancake Range is used for a belt of ignimbrite mesas and uplifted structural blocks, but in detail

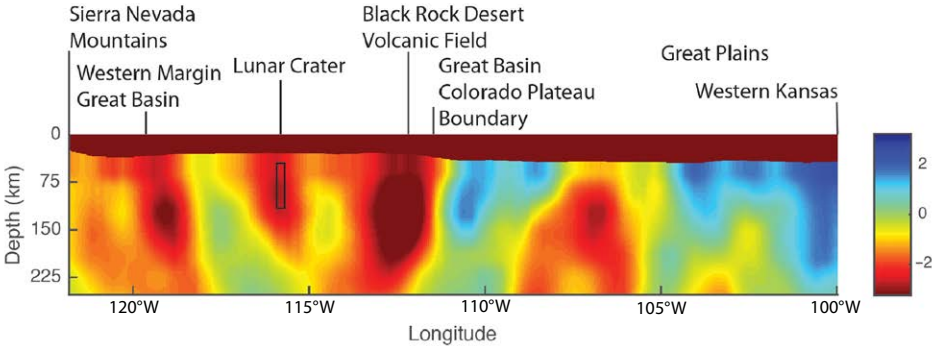

Figure 2. Tomographic profile across the western United States at lat 38°30′N latitude based on relative P wave velocities (Schmandt and Lin, 2014). Major physiographic features along the profile are labeled (cf. Fig. 1); see Figure 3 for location of lat 38°30′N with respect to the Lunar Crater Volcanic Field (LCVF). Colors reflect the percent difference between measured and model P wave velocities; warm colors (e.g., reds, oranges, yellows) are seismically slow areas, whereas cooler colors (e.g., purples, blues, greens) denote seismically fast mantle. The brown filled top of the profile represents the Earth's crust. The LCVF is directly above an irregularly shaped low-velocity domain. The rectangle represents the range of melting depths calculated by Cortés et al. (2015) and is directly within the low-velocity domain; the width of the box is approximately the width of the volcanic field at this latitude. Similar low-velocity domains underlie the western and eastern margins of the Great Basin (i.e., the Basin and Range Province), also locations of Quaternary volcanism.

it includes low-lying areas such as the Lunar Lake basin, where many of the Pleistocene volcanoes are situated. Basalts (loosely referring to trachybasalts, tephrites, basanites, and basalts sensu stricto) and very minor volumes of relatively evolved compositions erupted beginning ca. 6 Ma (Foland and Bergman, 1992; Yogodzinski et al., 1996) and continued to the Marcath eruption, ca. 35 ka (Table 1), indicating that the LCVF is essentially an active field that is in a period of dormancy between monogenetic events. The field contains 142–161 monogenetic volcanoes (46–65 in the Reveille Range with uncertainty related to extensive surface modification and erosion there, and 96 in the Pancake Range), most of which consist of a pyroclastic construct (cone or rampart) and an attendant lava field. Three small centers in the Reveille Range are trachyandesite to trachyte domes and lavas (Yogodzinski et al., 1996), but most are highly eroded scoria cones and mesa-capping lava fields (e.g., Hintz and Valentine, 2012; Harp and Valentine, 2015). The Pancake Range volcanoes also include four maars, two of which are associated with pristine to partly eroded scoria cones or elongate agglomerate ramparts from the same monogenetic events (Valentine et al., 2011; Amin, 2013; Valentine and Cortés, 2013), and the poorly exposed remnant of one tuff cone.

Geochronology

The ages of lavas in the LCVF have been compiled in four studies. The first was by Kargel (1987); these K-Ar results were summarized along with isotopic data by Foland and Bergman (1992). Naumann et al. (1991) reported K-Ar ages for the northern part of the Reveille Range and, along with Yogodzinski et al. (1996), suggested that volcanism there occurred in two episodes (before 5 Ma, and ca. 4.7–3 Ma) that were also chemically and petrographically distinct. A third set of ages was presented by Dickson (1997) and by Stickney (2004), and the fourth set is our work. Previous determinations by Kargel (1987) are not included in our discussion because they were whole-rock K-Ar analyses that tended to return older ages (especially for the Pleistocene rocks) that are not consistent with the more recent work, although Kargel's dates appear consistent with most stratigraphic relationships in terms of relative ages. For example, while Kargel (1987) correctly identified the Marcath eruption (described in the following) as the youngest in the volcanic field, his age is ca. 350 ka, which is inconsistent with the ca. 38–35 ka ages determined by independent methods (surface exposure and $^{40}Ar/^{39}Ar$) and with the pristine morphology of the lavas and cone. The older ages of Kargel (1987) might be related to inclusions and megacrysts that are common in the lavas. The Stickney (2004) ages, which focus on the northern approximately one-third of the Pancake Range, are not included because we found inconsistencies between the reported values and stratigraphic relationships in the field.

Table 1 summarizes our ages along with those of Dickson (1997) and Naumann et al. (1991), a total of 35 eruptive units (lavas, feeder dikes, and plugs) as well as 3 duplicate analyses by the different authors. All but one of these determinations is based on groundmass plagioclase, using either K-Ar analyses for the late Miocene–Pliocene rocks, or $^{40}Ar/^{39}Ar$ analyses for the younger rocks. The exception is Lunar Crater maar, where limited ejecta exposures and phreatomagmatic eruption mechanisms resulted in very little juvenile material that could be used for $^{40}Ar/^{39}Ar$ analyses. Here we applied the cosmogenic ^{10}Be surface exposure dating method, analyzing quartz phenocrysts from the Miocene rhyolitic ignimbrite that was ejected onto the tephra ring as ballistic blocks and exposed in the crater wall after having been buried by 3.82 Ma basalts (sample GVLC13–50; Table 1). The age of Lunar Crater maar is bracketed between ca. 72 ka (the minimum age from ^{10}Be exposure dating [Supplemental Table[1]]) and 190 ka (the age of the youngest lava that the Lunar Crater maar ejecta appears to overlap; sample LC12–85; Table 1). This range of ages, especially toward the younger portion of the range, is consistent with a qualitative estimate based upon morphology and soil development (Valentine et al., 2011).

Volcanism in the LCVF has gradually shifted northward since initial activity in the Reveille Range, a direction that is oblique to the North American plate motion and therefore not a hotspot track. During any given time window volcanoes formed apparently randomly (in time) over a significant fraction of the total area (Fig. 6; Naumann et al., 1991; Foland and Bergman, 1992). We have identified four episodes of magmatism, two of which were originally discussed

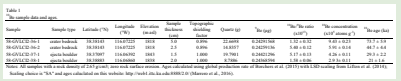

[1]Supplemental Table. Analytical data and calculations related to the ^{10}Be age determinations at Lunar Crater maar. Please visit http://dx.doi.org/10.1130/GES01428.S1 or the full-text article on www.gsapubs.org to view the Supplemental Table.

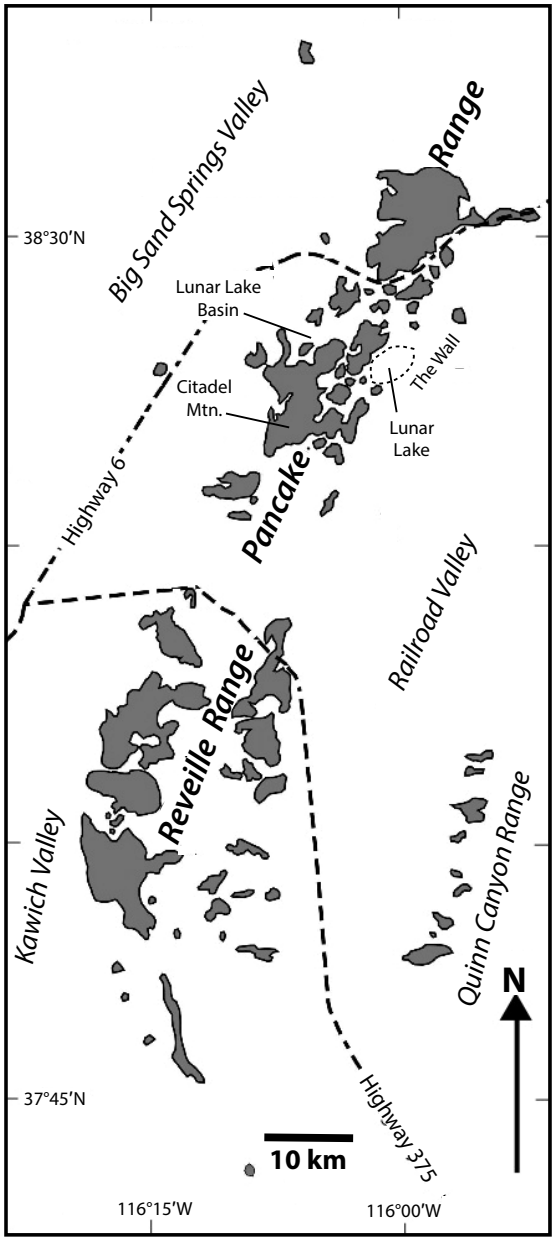

Figure 3. Simplified map of Lunar Crater volcanic field rocks (late Miocene–Pleistocene; shaded) and major geographic features (modified from Foland and Bergman, 1992; copyright 1992 by the American Nuclear Society, LaGrange Park, Illinois). The Grant Range, mentioned in the text but not shown in this map, extends to the northeast of the Quinn Canyon Range.

by Naumann et al. (1991) and Yogodzinski et al. (1996), based upon age, geochemistry, and petrographic similarities. Episode 1 (ca. 6–5.1 Ma) appears to have been restricted to the Reveille Range, probably extending 20–25 km farther south than indicated in Figure 6, where similar basaltic rocks occur but have not been dated (see Fig. 4). Where episode 1 is in contact with episode 2 rocks the contact is an unconformity, and episode 1 clasts are included in isolated fanglomerates around paleohighs that hosted some of the episode 2 centers, consistent with a significant time break between the episodes. Episode 2 (ca. 4.7–3 Ma) is prevalent in the northern Reveille Range and southern Pancake Range, probably extending ~10 km farther north than indicated in Figure 6; small, faulted remnants of a vent structure and lava flows occur around the edge of the Lunar Lake basin (a half-graben within the Pancake Range; Fig. 5) that are petrographically and morphologically similar to episode 2 lavas (e.g., Broken Cone; Hintz and Valentine, 2012) but these were not analyzed. It is possible that additional episode 2 lavas are subsided and buried in Lunar Lake basin, and that these might fill the apparent ~1.9 m.y. gap between episodes 2 and 3 (Fig. 6). Episodes 3 and 4 (1.1–0.4 Ma and 0.3–0.035 Ma, respectively) overlap each other spatially, as well as the northern extent of episode 2, in the Pancake Range.

Spatial Distribution of Volcanoes and Structural Relationships

Defining Boundaries

Definition of the boundaries of the LCVF is difficult due to subsidence of basins on either side of the Reveille and Pancake Ranges. It is likely that some basaltic centers occur in these basins but are buried by alluvial fill, and that the volcanic field is not as narrow as it appears from a surface geologic map, especially in its southern part. The presence of a small number of basaltic centers in the Quinn Canyon and Grant Ranges on the east side of Railroad Valley (Fig. 3) that have degrees of erosion and geochemistry similar to those of episode 1 and 2 centers in the Reveille Range (Emery, 2012) suggests that volcanism may have been continuous across that basin during late Miocene–Pliocene time. A line of three small, eroded, mostly buried cones occurs in the Kawich Valley to the west of the southern Reveille Range, along with a partly buried lava field (Fig. 4). These features suggest the possibility of additional buried volcanoes in that basin.

In the Pancake Range (Fig. 5) the eastern boundary of the volcanic field can be reasonably well defined and corresponds to the eastern, normally faulted margin of Lunar Lake basin (an escarpment referred to as the Wall; Ekren et al., 1972). The Big Sand Springs Valley that borders the northwestern part of the field might contain some buried basaltic centers. Drill core from a well located in Big Sand Springs Valley, ~5 km northwest of the Marcath cone, intersected basaltic lava intercalated with alluvium at a depth of 43–53 m (Ekren et al., 1974). The northern boundary of the volcanic field is abrupt, with a stepped transition from dense clusters of cones to none at all.

GEOLOGIC MAP OF THE SOUTHERN LUNAR CRATER VOLCANIC FIELD, REVEILLE RANGE, NEVADA

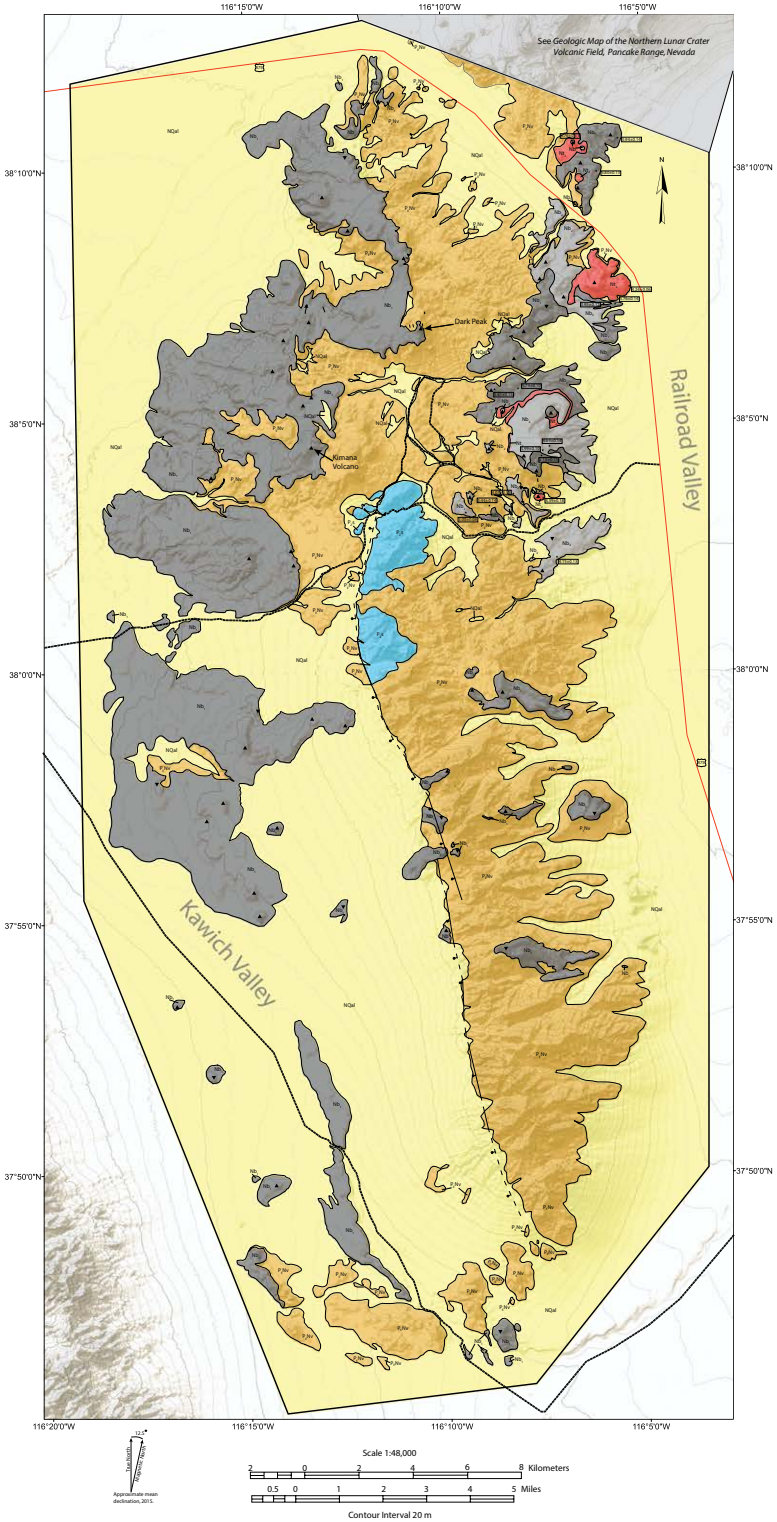

NQal ALLUVIUM, COLLUVIUM, AND EOLIAN DEPOSITS (Quaternary and Pliocene). Consolidated and unconsolidated gravel, sand, and silt. Includes alluvial fans, playa sediments, ephemeral stream sediments, slopewash, talus, and sand ramps.

Nb_2 LAVA FLOWS AND PYROCLASTIC DEPOSTIS OF EPISODE 2 (Pliocene). Tephrites, basalts, and trachybasalts with abundant millimeter-sized olivine phenocrysts and variable proportions of plagioclase and clinopyroxene phenocrysts. Centimeter-sized megacrysts include plagioclase and clinopyroxene with common gabbro inclusions. Cones and ramparts are highly eroded remnants, and lava fields have smooth surfaces and have incised edges. K-Ar ages range from 4.64 to 2.97 Ma (Table 1).

Nt_2 TRACHYTE DOMES, LAVAS, PYROCLASTIC DEPOSITS (Pliocene). Two trachyte lava flows and one small trachyandesite (tristanite) lava dome with associated breccias and tuff breccias. Fine grained texture with abundant 1-2 mm sanidine phenocrysts. K-Ar ages are 4.39 and 4.24 Ma (Table 1).

Nb_1 LAVAS, DIKES, AND PYROCLASTIC DEPOSITS OF EPISODE 1 (Late Miocene to Pliocene). Basalts and trachybasalts with abundant millimeter-sized olivine phenocrysts and variable proportions of plagioclase and pyroxene phenocrysts. Centimeter-sized megacrysts are plagioclase. Cones and ramparts are highly eroded with exposed dikes. Lava fields have smooth surfaces and form inverted topography. K-Ar ages range from 5.94 to 5.13 Ma (Table 1).

P_tNv UNDIFFERENTIATED OLDER VOLCANIC ROCKS (Oligocene-early Miocene). Mainly rhyolitic tuffs with minor rhyodacitic porphyry intrusions, rhyolite flows, surge deposits and intermediate lava flows associated with nearby calderas.

P_pS UNDIFFERENTIATED MARINE SEDIMENTARY ROCKS (Paleozoic). Carbonate and clastic sedimentary rocks, mostly dolomite and limestone, with minor quartzite and shale.

Geologic Contact

Normal fault, dashed where approximately located, ball on downthrown side

Vent

Vent, approximately located

Basaltic Dike

Sample location and age (Ma)

Highway

Dirt Road

Figure 4. Geologic map of Reveille Range emphasizing Lunar Crater volcanic field basaltic rocks. The Reveille Range includes products of episodes 1 and 2. Map is based upon our own work plus information from Naumann et al. (1991) and Martin and Naumann (1995). See Figure 5 for Geologic Map of Northern Lunar Crater Volcanic Field, Pancake Range, Nevada. For the full-sized version of Figure 4, please visit http://dx.doi.org/10.1130/GES01428.S2 or the full-text article on www.gsapubs.org.

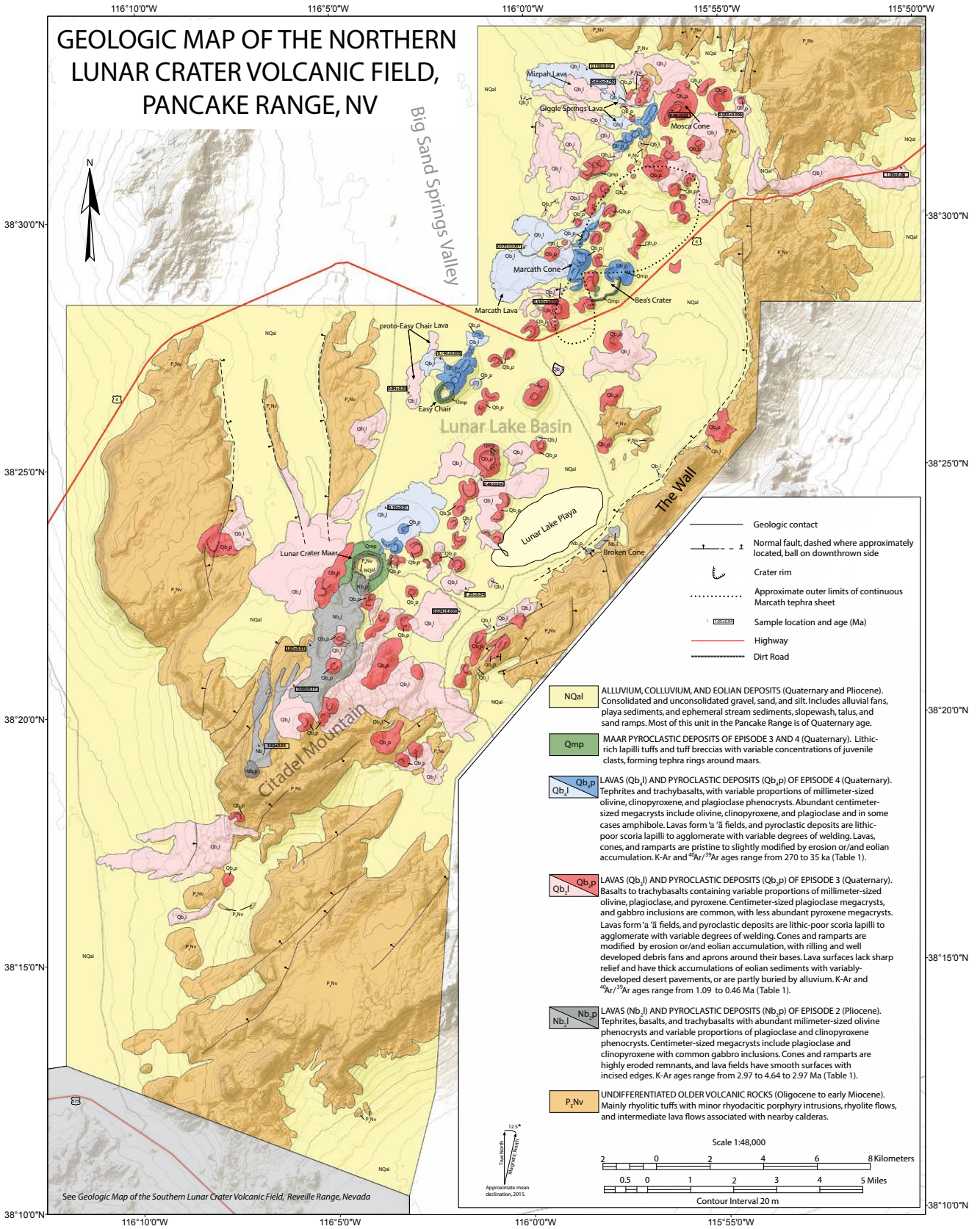

Figure 5. Geologic map of the Pancake Range emphasizing Lunar Crater volcanic field basaltic rocks. The Pancake Range includes products of episodes 2–4. Map is based upon our own work plus information from Snyder et al. (1972), Ekren et al. (1972), and Dickson (1997). For the full-sized version of Figure 5, please visit http://dx.doi.org/10.1130/GES01428.S3 or the full-text article on www.gsapubs.org.

TABLE 1. AGE DETERMINATIONS FOR LUNAR CRATER VOLCANIC FIELD

Sample	Lat* (°N)	Long* (°W)	Preferred age (Ma ± 1σ)	Comments, analytical method	Source
Pancake Range basaltic lavas of episode 4 with plagioclase, amphibole, olivine, pyroxene megacrysts.					
LC10-23	38°29.446′	116°00.043′	0.035 ± 0.007	Marcath lava (compare with ^{36}Cl and ^{10}Be exposure age, 0.038 ± 0.01 Ma; Shepard et al. [1995]). ^{40}Ar/^{39}Ar groundmass plagioclase.	This paper†
GV-LC12-36-1	38°22.891′	116°04.359′	≥0.072 ± 0.004 <0.19 ± 0.01	Lunar Crater maar minimum age determined by ^{10}Be exposure dating of quartz from rhyolitic ignimbrite exposed in crater wall; overlapping of Lunar Crater tephra ring onto lava of LC12-85 defines maximum age.	This paper††
LC10-01	38°32.267′	115°57.340′	<0.08	Relatively young looking lava field near northern edge of volcanic field (informally named Giggle Springs lava). ^{40}Ar/^{39}Ar groundmass plagioclase.	Cortés et al. (2015)§
LCN-20A	38.552°	244.019°	0.130 ± 0.07	Same flow as LC10-01 above, Giggle Springs lava. K-Ar groundmass plagioclase.	This paper**
LC11-71	38°26.846′	116°01.912′	0.140 ± 0.005	Easy Chair lava. ^{40}Ar/^{39}Ar groundmass plagioclase.	Valentine and Cortés (2013)§
LC12-85	38°23.986′	116°03.715′	0.19 ± 0.01	Relatively young looking lava field just north of Lunar Crater maar (cf. with ^{36}Cl exposure ages of ≥0.600 to 0.224 ± 0.043 Ma; Shepard et al. (1995)). ^{40}Ar/^{39}Ar groundmass plagioclase.	This paper†
GVLC13-53	38°23.231′	116°03.918′	0.27 ± 0.02	Uppermost lava and/or spatter rampart exposed in Lunar Crater maar. ^{40}Ar/^{39}Ar groundmass plagioclase	This paper†
Pancake Range basaltic lavas of episode 3 with variable megacrysts of plagioclase and sparse pyroxene, and commonly gabbro inclusions; ^{40}Ar/^{39}Ar groundmass determinations					
GVLC13-35-1	38°24.809′	116°01.117′	0.46 ± 0.04	Major lava unit covering much of area on west side of Lunar Lake. ^{40}Ar/^{39}Ar groundmass plagioclase.	This paper†
LC11-63	38°32.130′	115°54.982′	0.583 ± 0.006	Unnamed widespread lava near northeastern edge of field (north of Highway 6). ^{40}Ar/^{39}Ar groundmass plagioclase.	This paper§
LC10-05	38°32.691′	115°58.277′	0.620 – 0.740	Older lava field near northern edge of field, informally named Mizpah basalt. ^{40}Ar/^{39}Ar groundmass plagioclase.	Valentine and Cortés (2013)§
LCN-3	38.367°	243.970°	0.624 ± 0.005	Cone and lava field ~1.5 km southeast of Lunar Crater maar. ^{40}Ar/^{39}Ar groundmass plagioclase.	This paper**
LC37-96	38°20′23″	116°05′56″	0.66 ± 0.17	R-cone flow on Citadel Mountain. ^{40}Ar/^{39}Ar groundmass plagioclase.	Dickson (1997)
LC11-48	38°26.383′	116°02.748′	0.84 ± 0.03	Proto–Easy Chair lava that underlies Easy Chair lava. ^{40}Ar/^{39}Ar groundmass plagioclase.	Rasoazanamparany et al. (2015)†
LC12-79	38°32.144′	115°56.125′	0.88 ± 0.02	Dike in prominent red scoria cone (informally named Mosca cone) near northern edge of volcanic field. ^{40}Ar/^{39}Ar groundmass plagioclase.	This paper†
LCN-15	38.474°	244.010°	0.930 ± 0.070	Older lava ~1.5 km southwest of main Marcath vent. K-Ar groundmass plagioclase.	This paper**
LCN-10	38.376°	243.973°	1.05 ± 0.04	Lava vented from cone ~3.4 km east of Lunar Crater maar. K-Ar groundmass plagioclase.	This paper**
LCN-18	38.517°	244.162°	1.09 ± 0.08	Lava flow that extends eastward from Black Rock Pass, into Railroad Valley. K-Ar groundmass plagioclase.	This paper**
Pancake Range basaltic lavas of episode 2 containing plagioclase and pyroxene megacrysts and gabbro inclusions, representing northward migration of episode 2 volcanism from Reveille Range; ^{40}Ar/^{39}Ar determinations					
LC17-96	38°23′08″	116°04′27″	2.97 ± 0.03	Same lava as GVLC13-51. ^{40}Ar/^{39}Ar groundmass plagioclase.	Dickson (1997)
GVLC13-51	38°23.213′	116°03.946′	3.07 ± 0.02	Lava overlying GVLC13-50 in Lunar Crater maar. ^{40}Ar/^{39}Ar groundmass plagioclase.	This paper†
GVLC13-50	38°23.206′	116°03.945′	3.81 ± 0.01	Oldest lava exposed in Lunar Crater maar. ^{40}Ar/^{39}Ar groundmass plagioclase.	This paper†
LC40-96	38°21′30″	116°05′39″	3.82 ± 0.03	Same lava as GVLC13-50. ^{40}Ar/^{39}Ar groundmass plagioclase.	Dickson (1997)
LC38-96	38°19′37″	116°06′53″	3.82 ± 0.03	H-cone, Citadel Mountain. ^{40}Ar/^{39}Ar groundmass plagioclase.	Dickson (1997)
Reveille Range basaltic lavas of episode 2 (Naumann et al., 1991) containing plagioclase, pyroxene, and/or amphibole megacrysts, and gabbro inclusions; and two trachyte lavas.					
R8-1-27-LN	38°3′10″	116°9′23″	3.00 ± 0.08	Basalt plug. K-Ar groundmass plagioclase determinations.	Naumann et al. (1991)
R9-1-46-LN	38°10′30″	116°6′30″	3.76 ± 0.11	Basalt lava. K-Ar groundmass plagioclase determinations.	Naumann et al. (1991)
R9-1-58-LN	38°7′17″	116°5′45″	3.95 ± 0.12	Basalt lava. K-Ar groundmass plagioclase determinations.	Naumann et al. (1991)
R8-1-18-LN	38°4′20″	116°7′24″	3.99 ± 0.10	Basalt lava. K-Ar groundmass plagioclase determinations.	Naumann et al. (1991)
R8-1-2-LN	38°3′30″	116°8′20″	4.03 ± 0.12	Basalt lava. K-Ar groundmass plagioclase determinations.	Naumann et al. (1991)
R8-1-19-LN	38°2′15″	116°7′10″	4.15 ± 0.13	Basalt lava. K-Ar groundmass plagioclase determinations.	Naumann et al. (1991)
R8-1-43-LN	38°7′45″	116°5′20″	4.24 ± 0.06	Trachyte lava. K-Ar groundmass plagioclase determinations.	Naumann et al. (1991)
R8-1-16-LN	38°3′18″	116°8′52″	4.39 ± 0.18	Small trachyandesite (tristanite) lava dome. K-Ar groundmass plagioclase determinations.	Naumann et al. (1991)
R8-1-13-LN	38°4′23″	116°7′18″	4.64 ± 0.14	Basalt plug. K-Ar groundmass plagioclase determinations.	
Reveille Range basaltic lavas of episode 1 (Naumann et al., 1991) containing plagioclase megacrysts; K-Ar groundmass plagioclase determinations					
R8-1-17-LN	38°4′15″	116°7′24″	5.13 ± 0.15	Basalt lava. K-Ar groundmass plagioclase determinations.	Naumann et al. (1991)
R8-1-24-LN	38°3′18″	116°8′52″	5.44 ± 0.14	Basalt dike. K-Ar groundmass plagioclase determinations.	Naumann et al. (1991)
R8-1-29-LN	38°5′39″	116°8′40″	5.61 ± 0.15	Basalt plug. K-Ar groundmass plagioclase determinations.	Naumann et al. (1991)
R8-1-28-LN	38°5′40″	116°8′5″	5.74 ± 0.10	Basalt lava. K-Ar groundmass plagioclase determinations.	Naumann et al. (1991)
R9-1-57-LN	38°7′15″	116°5′45″	5.76 ± 0.14	Basalt lava. K-Ar groundmass plagioclase determinations.	Naumann et al. (1991)
R9-1-48-LN	38°9′48″	116°6′2″	5.80 ± 0.13	Basalt lava. K-Ar groundmass plagioclase determinations.	Naumann et al. (1991)
R9-1-56-LN	38°10′33″	116°5′30″	5.94 ± 0.14	Basalt plug. K-Ar groundmass plagioclase determinations.	Naumann et al. (1991)

*Locations from original data sources.
†Analytical details in Heizler (2014).
§Analytical details in Heizler (2013).
**Age determination by B.D. Turrin.
††See Supplemental Table (footnote 1 in text).

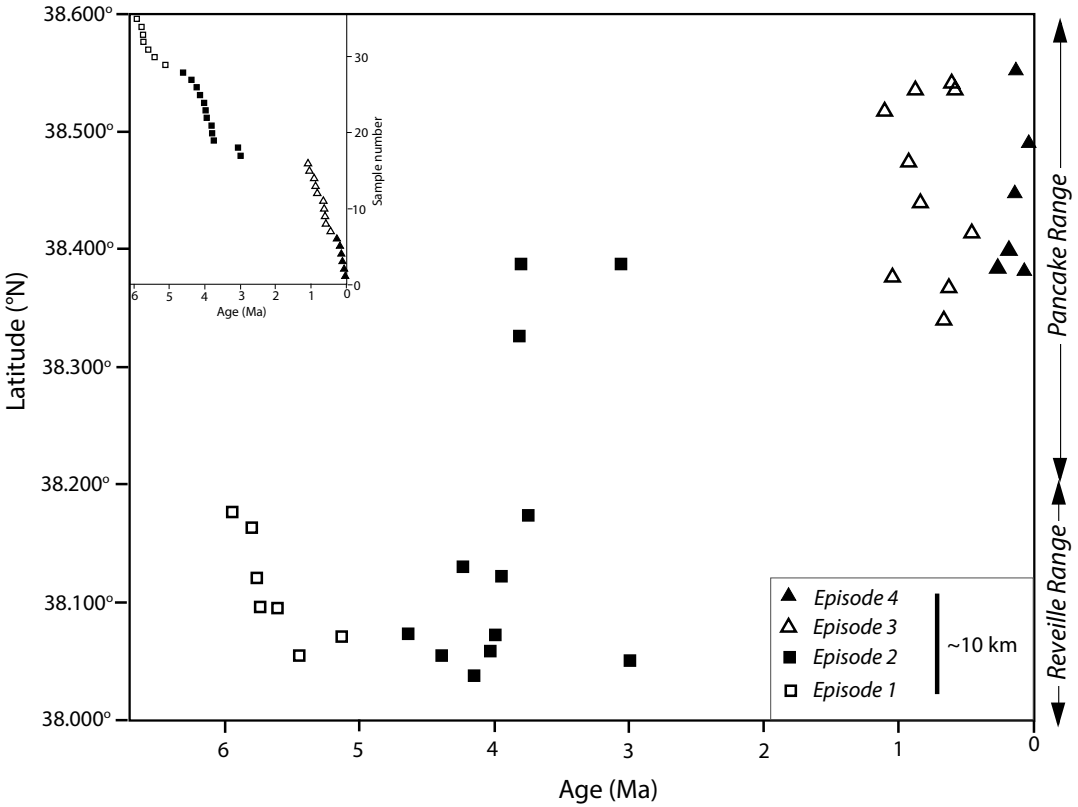

Figure 6. Age data for 35 samples from the Lunar Crater volcanic field plotted against latitude (see Table 1). Samples from the Reveille Range (south of 32.2°N, and all older than 3 Ma) are K-Ar dates, while samples from Pancake Range north of 38.2°N) are $^{40}Ar/^{39}Ar$ dates. During any individual episode, volcanism occurred seemingly randomly over a broad area ranging from ~20 to 50 km along the axis of the field. Note that the volcanic field extends ~25 km southward from the latitudes plotted; most volcanism in that area was likely part of episode 1, but was not sampled. The time gap between episodes 2 and 3 might be due to lack of sampling as well subsidence and burial of older basaltic rocks in the Lunar Lake basin (within the Pancake Range). The distance gap between episode 2 lavas in Reveille Range and those in the Pancake Range might reflect lack of sampling as well as relatively sparse occurrence of basaltic volcanoes between the two ranges (there is an ~10 km gap with no volcanoes). Inset shows distribution of sample ages. Note that the age of Lunar Crater maar age is plotted here as 70 ka.

Pancake Range Clustering and Alignments

Tadini et al. (2014) conducted a formal analysis of vent clustering and alignment for the Pancake Range, and the age data provide additional insight. Most volcanoes in the Pancake Range occur in clusters, while ~20% of the volcanoes are isolated (>~1 km from nearest neighbor). Some clusters are quite dense; one at the northern end of the field contains 12 separate cones within a 5 km² area. Scoria cones commonly overlap within such clusters because their individual basal diameters are ~400–1500 m. Two dated volcanoes within ~500 m of each other in the northernmost cluster have ages of ca. 130 ka and 740–620 ka (Giggle Springs and Mizpah lavas, respectively; Table 1; Cortés et al., 2015; Rasoazanamparany et al., 2015). The youngest volcano in the field, Marcath, is on top of older cones, and the flow paths of its lavas were strongly influenced by cone-cluster topography. In the cluster that includes Easy Chair volcano, the field evidence suggests approximately co-located vents for eruptions ca. 840 ka (proto–Easy Chair; Table 1) and 140 ka. Thus the clusters repeatedly underwent monogenetic eruptions over periods of many hundreds of thousands of years. We do not interpret this to be evidence of a polygenetic volcano in the sense of having a sustained magma feeding and crustal reservoir system over tens or hundreds of thousands of years, because in both the cases specified, the two eruptions (Mizpah-Giggle Springs and proto–Easy Chair-Easy Chair) have significantly different source geochemistry (Rasoazanamparany et al., 2015). Rather, these are random intersections of event locations within clusters. Similar long-term reuse of clusters was documented in the San Francisco volcanic field (Arizona; Conway et al., 1997). It is likely that there are many other such situations in the LCVF that were not dated, or where later events completely buried the products of earlier ones. We also note that the ca. 140 ka Easy Chair eruption was quite complex, producing a series of agglomerate ramparts, two central scoria cones, and a maar crater, all apparently within the context of a single monogenetic event (Valentine and Cortés, 2013). The term monogenetic volcanism does not imply simple, isolated volcanoes.

The volcanic field as a whole is elongated ~N30°E. Clusters within the Pancake Range are also preferentially elongated in this direction, as are many craters and nearly all eruptive fissures and ramparts (Tadini et al., 2014). Thus ~N30°E is a preferred orientation for processes at a range of length scales. Tadini et al. (2014) summarized broad relationships between the orientations of volcanism and structures in the host rocks (mainly Oligocene–early Miocene volcanics) and Quaternary tectonics. The current maximum horizontal principal stress in the region, based mainly upon focal mechanisms of earthquakes on normal faults, is also oriented ~N30°E (Heidbach et al., 2008). Quaternary faults in the region surrounding the LCVF have a similar, but broader, range of strikes; most are between north-south and N60°E. Older faults trend closer to north-south or north-northwest–south-southeast, reflecting earlier stress fields within the Basin and Range (older than ca. 10 Ma; Zoback et al., 1981), or have orientations more closely related to Oligocene–Miocene caldera structures.

Relationships of Preexisting Structures, Vents, and Feeder Dikes in the Pancake Range

Although burial by young volcanic products has obscured relationships between faults and vents, there are some locales in the Pancake Range where it is clear that vents are colocated with preexisting faults. These are mainly around the periphery of the field, where volcanoes are relatively isolated, so it is possible that the vent-fault relationships there do not hold in the more concentrated parts of the volcanic field (see Tadini et al., 2014). Near the southwestern (Fig. 7A) and southern edges of the Pancake Range scattered vents are located on normal faults associated with the hinge side of the Lunar Lake half-graben and with the southern escarpment of the Citadel Mountain structural block. Four vents are prominently located along the escarpment bounding the east side of Lunar Lake basin (the Wall; Figs. 7B, 7C). In some of these cases the vent-hosting faults have been active since the eruptions, and in others it is not clear (the latter are morphologically younger volcanoes, likely associated with episode 3). Previously workers have inferred the presence of buried faults from elongations and alignments of cones and ramparts (e.g., Scott and Trask, 1969; Snyder et al., 1972), but we do not make this inference without direct evidence for displacement before and/or after volcanic activity at a given location.

For a feeder dike to occupy a fault plane, the magma pressure in the dike must be sufficient to overcome the minimum compressive stress, σ_3, plus the added components of stress due to the strike and dip of the fault plane (compared to being a vertical plane perpendicular to σ_3 in the regional extensional setting; Delaney et al., 1986; Valentine and Krogh, 2006; Gaffney et al., 2007). In general, faults occupying vents in the Pancake Range, and by inference their feeder dikes, occur where the host faults have the north-northeast trend that is shared by vent alignments and the volcanic field elongation, rather than where faults have orientations that differ from the Quaternary principal stress orientations. The preference of feeder dikes for faults striking perpendicular to the Quaternary σ_3 indicates that magmas did not have large overpressures. It is likely that the ascending dikes were captured by faults in the upper few hundred meters of the crust, where the component of overburden pressure acting on the fault planes was low enough for the low magma pressures to overcome it (see Valentine and Krogh, 2006; Gaffney et al., 2007). In this sense the faults did not represent pathways or weaknesses for magmas to follow from depth, as is often inferred when volcanoes are located on faults, but rather represent coincidences where a feeder dike was sourced beneath a favorably oriented fault (e.g., Valentine and Perry, 2006).

The northernmost part of the field (Fig. 7D) appears to have concentrated basaltic volcanism in a small graben-like domain, bounded by approximately north-south–trending blocks of Oligocene–early Miocene volcanic rocks, that is now partly filled with basalt. This ~3-km-wide domain extends ~5 km north-northeast beyond the limit of basaltic volcanism, forming a complex belt of normally faulted blocks of Oligocene–early Miocene ignimbrites (see northern edge of geologic map; Fig. 5). To the south-southeast the domain apparently plunges toward the larger half-graben of the Lunar Lake basin and disappears beneath basaltic lavas and sedimentary fill. Most of the volcanoes in the Lunar Lake basin occur along the south-southeast projection of the graben-like domain; however, some volcanoes might be subsided and buried beneath the basin, leaving us with only a partial picture of volcano distribution. The western horst of the graben-like domain in turn formed an ~100-m-high escarpment bounding the edge of Big Sand Springs Valley. Basaltic volcanism has been intense along this escarpment and most of the episode 4 products have vented along it (e.g., Giggle Springs and Marcath volcanoes) or its projection beneath the Lunar Lake basin (e.g., Easy Chair volcano and Lunar Crater maar). Small normal faults have displaced episode 3 lavas to the west of the escarpment, indicating concurrent extensional deformation and volcanism.

Reveille Range

Although formal analysis of clustering and alignments has not been conducted for the Reveille Range volcanoes, it is clear that they share some common elements with those in the Pancake Range, especially the tendency for centers to occur in clusters (Fig. 4). Individual clusters in the northeastern part of the range underwent both episode 1 and 2 volcanism, with age differences of ~1–2 m.y. (e.g., compare age of sample R8–1-17-LN, ca. 5.13 Ma, with that of nearby but stratigraphically higher sample R8–1-18-LN, ca. 3.99 Ma; Table 1). Vents, in the forms of highly eroded cone and agglomerate rampart remnants, are concentrated on either side of the range and some of these are clearly related to the range-bounding, north-northwest–trending fault along the western side (Fig. 4). The line of isolated vents in the Kawich Valley to the west has a similar orientation and might be associated with a buried, inactive fault. Other volcanoes might be colocated with preexisting structures; for example, Dark Peak, a cone remnant in the north-central part and along the crest of the Reveille Range, is centered within 200 m of an older caldera rim (Harp and Valentine, 2015).

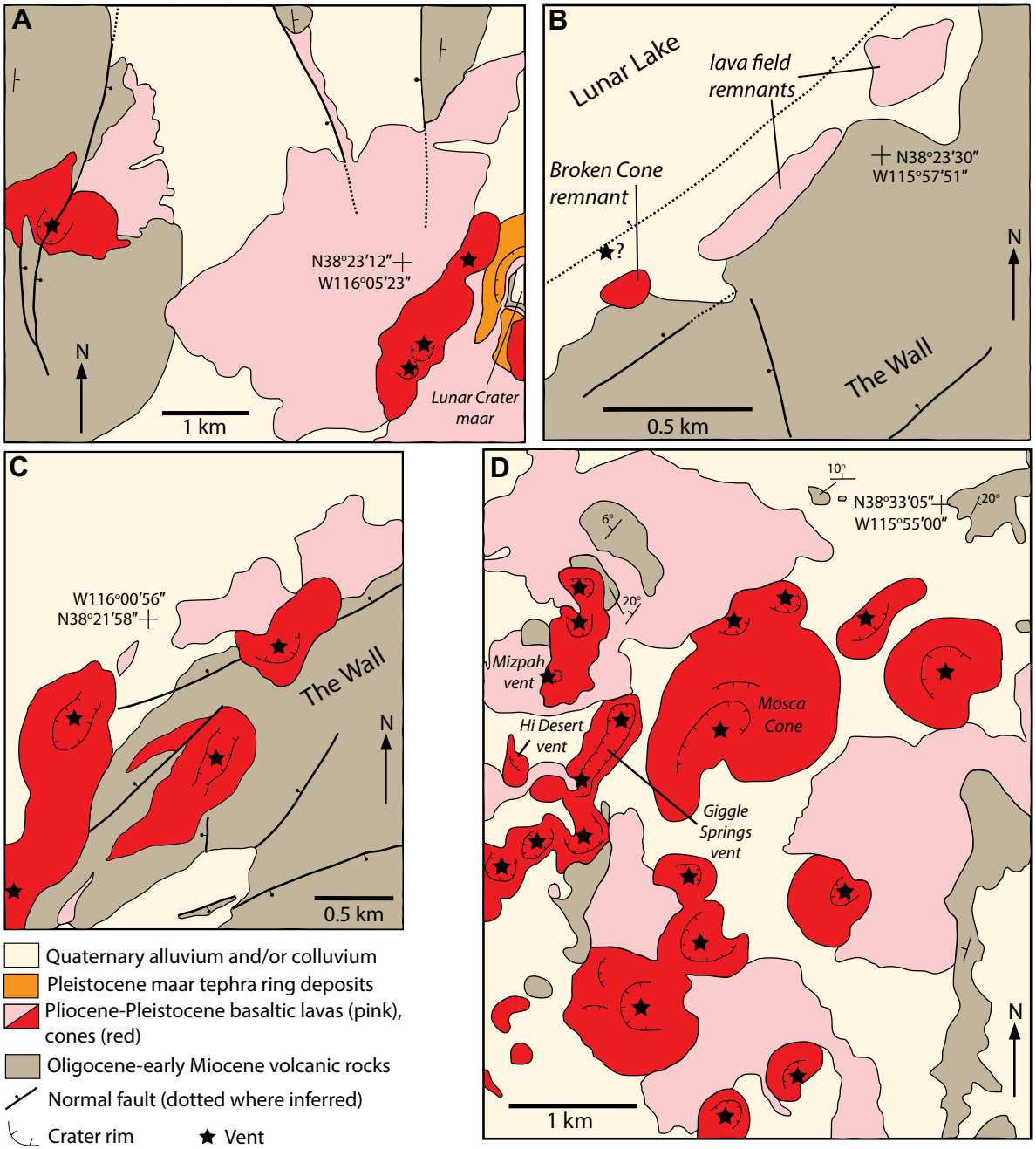

Figure 7. Simplified geologic maps of example sites in the Pancake Range that illustrate relationships between vents and preexisting structures. A-C are based upon Ekren et al. (1972), Snyder et al. (1972), and our mapping. (A) Vents to the west of Lunar Crater maar. The westernmost is intersected by a fault that has been active since the scoria cone eruption. Two of the vents just to the southwest of the maar are on the projections of faults, as well as along the north-northeast–south-southwest–trending side of the Citadel Mountain block. (B) Broken Cone is the remnant of a cone and lava field, most of which is inferred to have been displaced downward along the Lunar Lake basin–bounding fault and buried by basin fill (see Hintz and Valentine, 2012). The exact vent location is not known, but likely coincided at least approximately with the fault. We place this volcano in episode 2 based upon its hand specimen petrography and morphology. (C) One vent is on the main fault that forms the Wall (escarpment that bounds the eastern margin of Lunar Lake basin), and another along its projection. It is not clear if there has been movement along the fault since these two volcanoes formed. (D) The northernmost part of the Lunar Crater volcanic field. Here the spatial density of vents is relatively high and lavas bury most structures, but outcrops of older Paleogene–Neogene volcanics on either side of the area suggest the possibility of a small north-south–trending graben. Basaltic volcanoes have nearly filled the graben, and many vents occur along its western horst, which forms an escarpment bounding the large Big Sand Springs Valley to the west.

Petrology and Geochemistry—Magma Sources and Ascent

Data Sources

Representative major and trace element analyses for the four eruptive episodes were compiled from Yogodzinski et al. (1996), Dickson (1997), Cortés et al. (2015), and Rasoazanamparany et al. (2015). Previously published Sr, Nd, and Pb isotope data for samples from episode 1 (Yogodzinski et al., 1996) and episodes 3 and 4 (Rasoazanamparany et al., 2015) were also compiled for comparison in this study. In addition to these previously published data, we performed new Sr, Nd, and Pb isotope analyses of subset of episode 2 basalt samples that were originally reported by Yogodzinski et al. (1996). Sample leaching, dissolution, chemical purifications, and mass spectrometry were performed following the procedures used previously for the episode 3 and 4 sample isotopic analyses (detailed in Rasoazanamparany et al., 2015), in order for these data sets to be directly comparable. Relatively minor differences between the new data and the previous results of Yogodzinski et al. (1996), likely due to differences of acid leached versus nonleached samples, respectively, indicate that the isotopic data sets for all four magmatic episodes can be meaningfully compared to one another.

Summary of Petrologic and Geochemical Data

Episodes 1 and 2. Episodes 1 and 2 were first described in studies of the Reveille Range by Naumann et al. (1991). Episode 1 (ca. 5.9–5.1 Ma; Table 1) products comprise primarily alkalic, hawaiitic basalts containing olivine and plagioclase phenocrysts and megacrysts of laboradorite, with whole-rock SiO_2 and MgO contents ranging, respectively, from 45.5 to 49.4 wt% and 3.4 to 6.1 wt% (Yogodzinski et al., 1996). Basalts of episode 2 (ca. 4.6–3.0 Ma; Table 1) are also alkalic, but range from trachybasalt to basanite, and are characterized by megacrysts of plagioclase, clinopyroxene, and/or amphibole and phenocrysts of olivine, plagioclase, clinopyroxene, and Fe-Ti oxides. Most are nepheline-normative, and SiO_2 and MgO both vary widely, from 41.8 to 47.8 wt% and 4.4 to 10.2 wt%, respectively (Figs. 8 and 9; Yogodzinski et al., 1996). Very small quantities of more evolved trachyandesite and trachytes erupted at the beginning of or just prior to episode 2. Gabbro inclusions as much as several centimeters in size also occur in many of these lavas; some localities contain abundant dunite and harzburgite inclusions (Yogodzinski et al., 1996).

Episodes 1 and 2, like the subsequent episodes 3 and 4, have trace element abundances that are similar to ocean island basalts (OIBs), with enrichments relative to primitive mantle in moderately to highly incompatible elements, including relative enrichments in the high field strength elements Nb and Ta, and in light rare earth elements (REEs) relative to heavy REEs (Fig. 10). These data are consistent with an asthenospheric, OIB-like mantle source region for both magmatic episodes. Episode 1 and 2 samples overlap in Zr/Nb (most in a narrow range from 6 to 8, with a few as high as 12 to 14), suggesting that they may share a geochemically similar source; in contrast, a large range in La/Yb ratios (Fig. 11) among samples from episode 1 (12–18) and especially episode 2 (10–25) could be indicative of more variable degrees of source melting (e.g., Cortés et al., 2015).

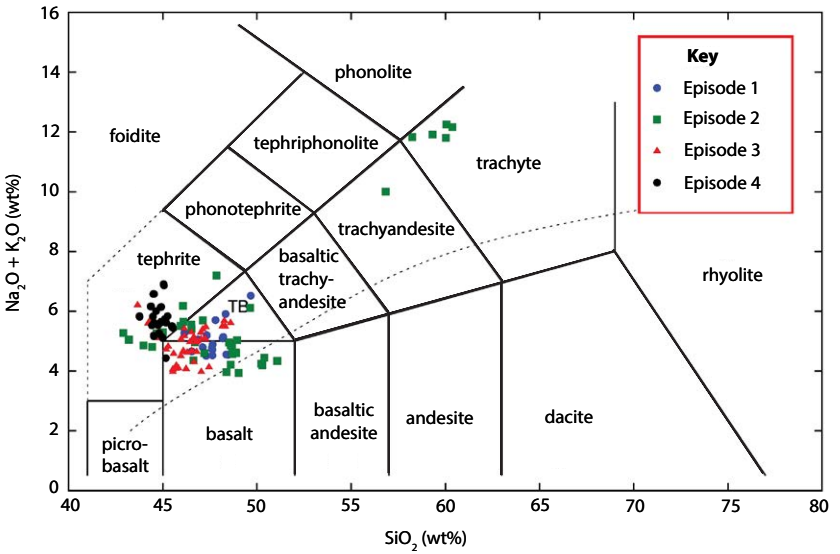

Figure 8. Total alkali-silica (TAS) plot for the four episodes of basaltic volcanism at Lunar Crater volcanic field (Le Maitre, 2002) based upon analyses published by Yogodzinski et al. (1996), Dickson (1997), Cortés et al. (2015) and Rasoazanamparany et al. (2015). TB—trachybasalt.

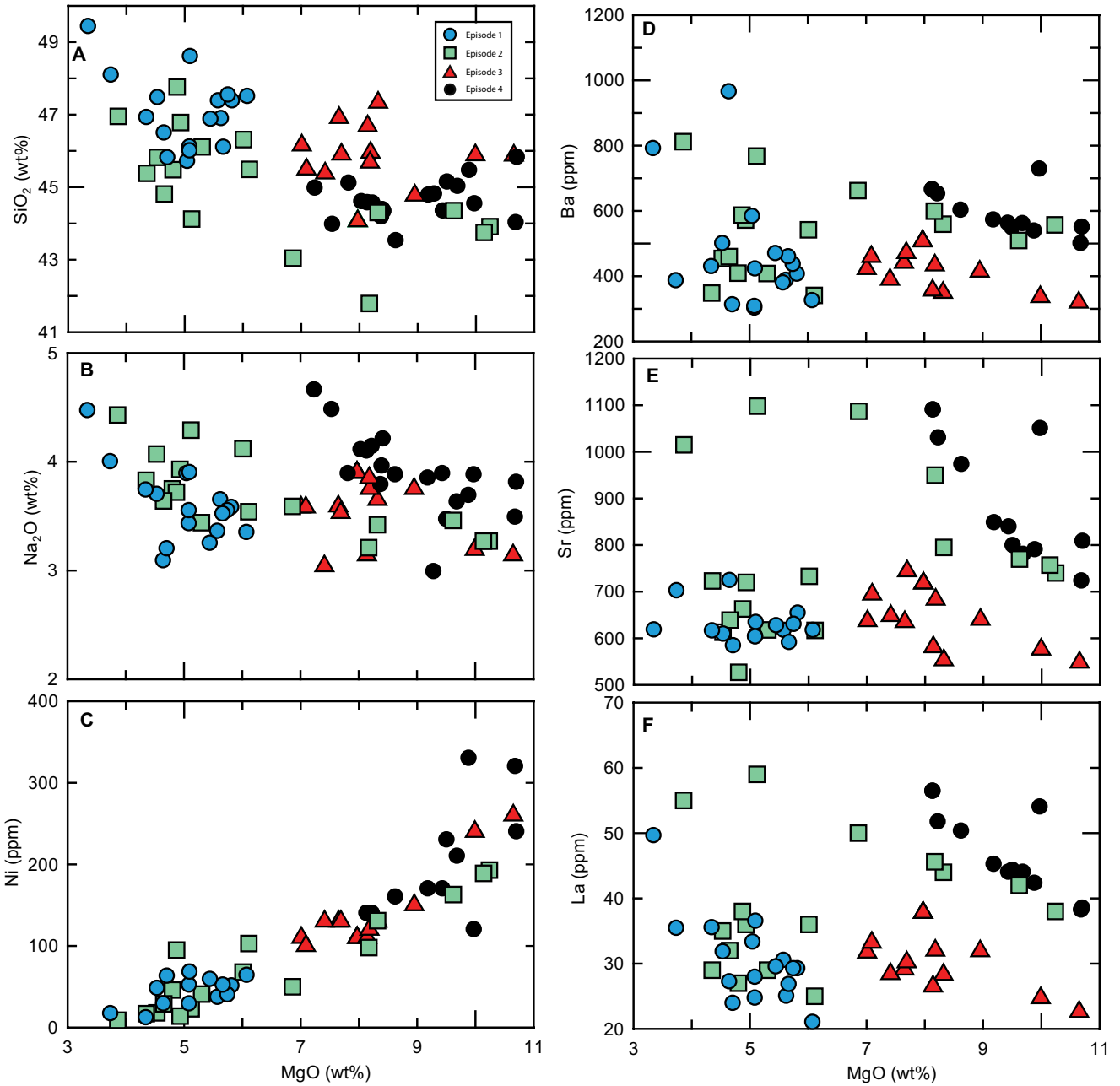

Figure 9. Abundances of SiO_2, Na_2O, and selected trace elements plotted against MgO for all four basaltic episodes at Lunar Crater volcanic field.

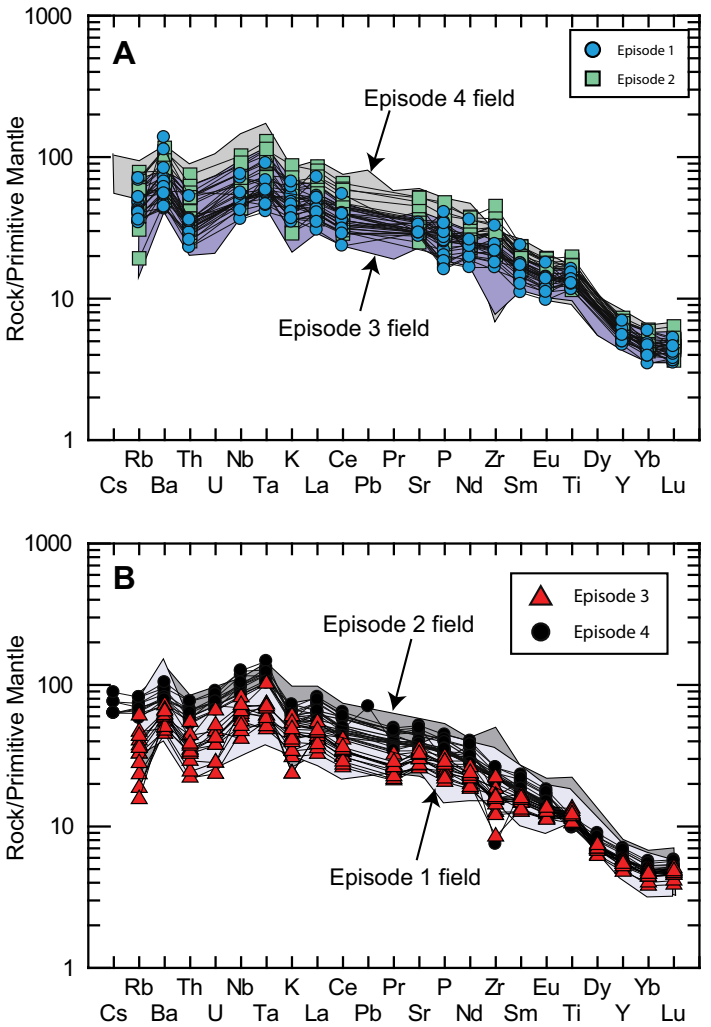

Figure 10. Spider-type plots normalized to primitive mantle, according to Sun and McDonough (1989). (A) Episodes 1 and 2. (B) Episodes 3 and 4.

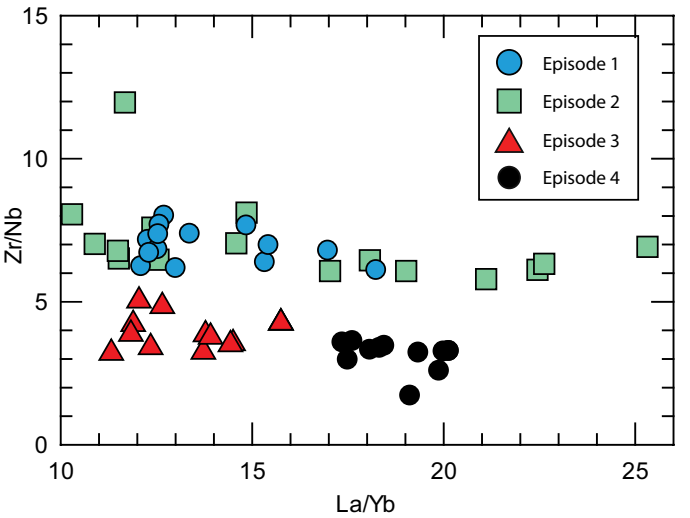

Figure 11. Zr/Nb plotted against La/Yb for Lunar Crater volcanic field basaltic rocks.

The Sr, Nd, and Pb isotope signatures of the episode 1 and 2 basalts likewise exhibit significant ranges. Most pronounced is the range in $^{87}Sr/^{86}Sr$ in episode 1 basalts (0.70427–0.70611) that correlates with a (more modest) variation in Nd isotopes (ε_{nd} +1 to +5; $^{143}Nd/^{144}Nd$ from 0.512680 to 0.512866), including basalts in the Reveille and Quinn Canyon Ranges (Yogodzinski et al., 1996; Emery, 2012). These isotope systematics, which result in a concave downward trend of the episode 1 basalts in Sr-Nd isotope space (Fig. 12), led Yogodzinski et al. (1996) to infer contamination by the thick carbonate section that is beneath much of the volcanic field. Foland and Bergman (1992) showed that Sr and Nd isotopes of basalts in the area are positively correlated with oxygen isotopes ($\delta^{18}O$) and also suggested that older Pliocene basalts in the Reveille Range were contaminated by continental crust.

New whole-rock Sr, Nd, and Pb isotope ratios for episode 2 basalts from the Reveille Range (Table 2) show a substantially more limited variation in $^{87}Sr/^{86}Sr$ (0.70337–0.70351), as well as $^{143}Nd/^{144}Nd$ (0.512810–0.512855) and Pb ($^{206}Pb/^{204}Pb$ = 19.122–19.375; $^{207}Pb/^{204}Pb$ = 15.591–15.615; $^{208}Pb/^{204}Pb$ = 38.770–38.966) isotopic compositions. In comparison to the episode 1 basalts, episode 2 basalts are significantly less radiogenic in Sr, and comparable to or higher in $^{143}Nd/^{144}Nd$ than the most radiogenic of the episode 1 basalts (Fig. 12A). Episode 2 Pb isotope signatures plot on the same trend as episode 1 in $^{206}Pb/^{204}Pb$ versus $^{208}Pb/^{204}Pb$, but most have higher $^{206}Pb/^{204}Pb$ (Fig. 13A). The $^{207}Pb/^{204}Pb$ variations are minimal, but on average, $^{207}Pb/^{204}Pb$ is slightly higher in episode 1 basalts (Fig. 13B); this has been attributed to the influence of crustal assimilation (Yogodzinski et al., 1996). The isotope data, as observed for the trace element data, are consistent with the two magmatic episodes sharing a similar but heterogeneous mantle source, the composition of which is more closely reflected by the episode 2 basalts that, unlike the episode 1 basalts, did not undergo significant crustal assimilation (Yogodzinski et al., 1996, and this study). We did not conduct new analyses on the small volumes of trachyandesite and trachyte that occur in the northeastern part of the Reveille Range. Their ages (Table 1) correspond to early episode 2. Yogodzinski et al. (1996)

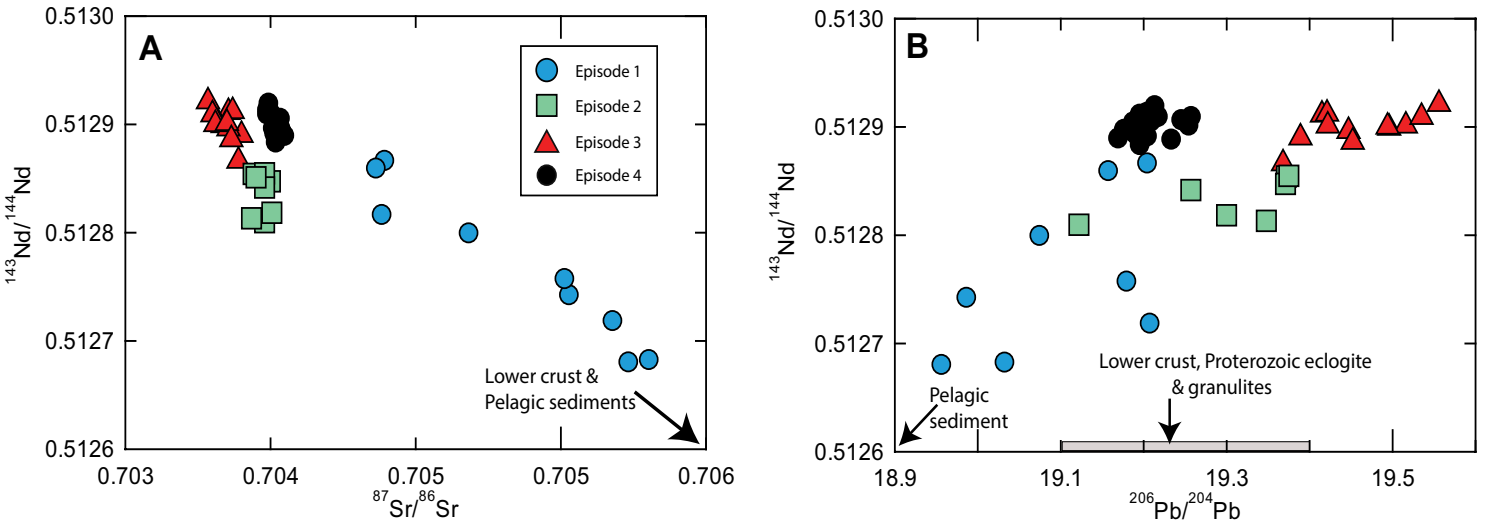

Figure 12. (A) $^{143}Nd/^{144}Nd$ versus $^{87}Sr/^{86}Sr$ for the Lunar Crater volcanic field basalts. (B) $^{143}Nd/^{144}Nd$ versus $^{206}Pb/^{204}Pb$.

assessed these rocks and determined, based mainly upon isotopic evidence, that they were probably evolved from episode 1 basaltic magmas.

Episodes 3 and 4. Episodes 3 and 4 occur only in the Pancake Range. Episode 3 lavas (ca. 1.1–0.4 Ma; Table 1; referred to as the HiMUp group in Rasoazanamparany et al., 2015) (HIMU—high-μ, where $\mu = {}^{238}U/{}^{204}Pb$) range in composition from basalt to trachybasalts (Fig. 8), and are characterized by variable concentrations of plagioclase megacrysts, relatively sparse pyroxene megacrysts, and common gabbro inclusions, with variable proportions of phenocrysts of olivine, plagioclase, and pyroxene. Whole-rock SiO_2 and MgO contents range, respectively, from 44.1 to 48.3 wt% and 7.0 to 10.7 wt%; some samples are close to primitive mantle melt compositions with Ni contents >120 ppm (and as much as 260 ppm) and Cr contents >220 ppm (and as much as 270 ppm) (Rasoazanamparany et al., 2015). Episode 4 (ca. 300 ka; Table 1; referred to as the GEM group in Rasoazanamparany et al., 2015) includes tephrites, basanites, and trachybasalts. They contain conspicuous euhedral megacrysts of plagioclase, pyroxene, olivine, and amphibole in varying proportions, all of which are interpreted as comagmatic with the host lavas, as well as a range of ultramafic inclusions (Bergman et al., 1981; Bergman, 1982; Foland and Bergman, 1992). Phenocrysts are olivine, plagioclase, and pyroxene, also in varying proportions. Whole-rock SiO_2 and MgO contents are similar to those of episode 3, ranging, respectively, from 43.5 to 45.8 wt% and 7.2 to 10.7 wt%.; likewise, some episode 4 samples also approximate primitive mantle melt compositions with Ni contents reaching 360 ppm and Cr contents reaching 820 ppm (Rasoazanamparany et al., 2015).

TABLE 2. WHOLE-ROCK Sr, Nd, AND Pb ISOTOPIC COMPOSITIONS FOR REANALYZED EPISODE 2 ROCKS

Sample	Lat (N)	Long (W)	$^{206}Pb/^{204}Pb$	$^{207}Pb/^{204}Pb$	$^{208}Pb/^{204}Pb$	$^{87}Sr/^{86}Sr$	$^{143}Nd/^{144}Nd$
R8-1-13	38°4.4′	116°7.3′	19.372	15.601	38.894	0.70338	0.512854
R8-1-18	38°4.4′	116°7.4′	19.371	15.600	38.900	0.70350	0.512847
R8-1-19	38°2.4′	116°7.2′	19.384	15.606	38.908	0.70346	0.512855
R8-1-22	38°3.5′	116°9.3′	19.257	15.612	38.862	0.70346	0.512842
R8-1-27	38°3.2′	116°9.4′	19.122	15.606	38.770	0.70346	0.512810
R9-1-46	38°10.5′	116°6.6′				0.70340	0.512851
R8-1-47	38°10.4′	116°6.4′	19.348	15.615	38.966	0.70337	0.521813
R9-1-55	38°8.2′	116°7.7′	19.300	15.591	38.850	0.70351	0.512818

Note: Samples originally reported in Yogodzinski et al. (1996).

Detailed whole-rock and mineral chemistry data from two episode 3 eruptive centers (Cortés et al., 2015) suggest that the magmas may have originated by 3%–5% partial melting of an olivine websterite-lherzolite source at depths of 60–130 km. The magmas partially crystallized at depths of 30–45 km, either while stalled near the base of the crust (30–35 km thick) or during ascent in that depth interval, after having risen directly from source depths (Spera and Fowler, 2009; Rasoazanamparany et al., 2015; Cortés et al., 2015). After ~50% crystallization, the magmas then ascended rapidly to the surface, with no geochemical evidence for crustal contamination. In contrast, episode 4 magmas appear to have crystallized at two levels: first near the base of the crust (30–45 km depth), and second, at mid-crustal levels where, in the case of Marcath, amphibole megacrysts formed and indicate a dissolved water content of 5–7 wt% in magma at that depth (Cortés et al., 2015). Rapid ascent between (and possibly including) crystallization levels is supported by the relatively primitive nature of these magmas and the lack of detectable assimilation of crustal components (Cortés et al., 2015; Rasoazanamparany et al., 2015).

Trace element patterns of episode 3 and 4 lavas are similar to those of episodes 1 and 2, with OIB-like relative enrichments in Nb-Ta, and light REEs relative to heavy REEs. All sample groups largely overlap in their trace element abundance patterns (Fig. 10). However, in detail the episode 3 and 4 lavas differ from one another modestly in their trace element patterns, with episode 4 lavas having on average higher concentrations of highly incompatible trace elements, steeper REE patterns (higher La/Yb), and higher Zr/Hf (Rasoazanamparany et al., 2015), but slightly lower Zr/Nb ratios (Fig. 11) than episode 3 basalts.

Radiogenic isotope data are available for 34 lavas from episodes 3 and 4; a subset of those (19 and 13, respectively) was analyzed for Os and Hf isotopes (Rasoazanamparany et al., 2015). Episode 4 data include 20 samples from Marcath, Giggle Springs, and Easy Chair; episode 3 data comprise 14 samples from Hi Desert, Mizpah, proto–Easy Chair, and 8 unnamed cones. The radiogenic isotope data are consistent with the trace element data in that they likewise reflect OIB-like mantle source signatures. In Sr-Pb isotope space (Fig. 14), the lavas collectively produce a two-component mixing trend between a high

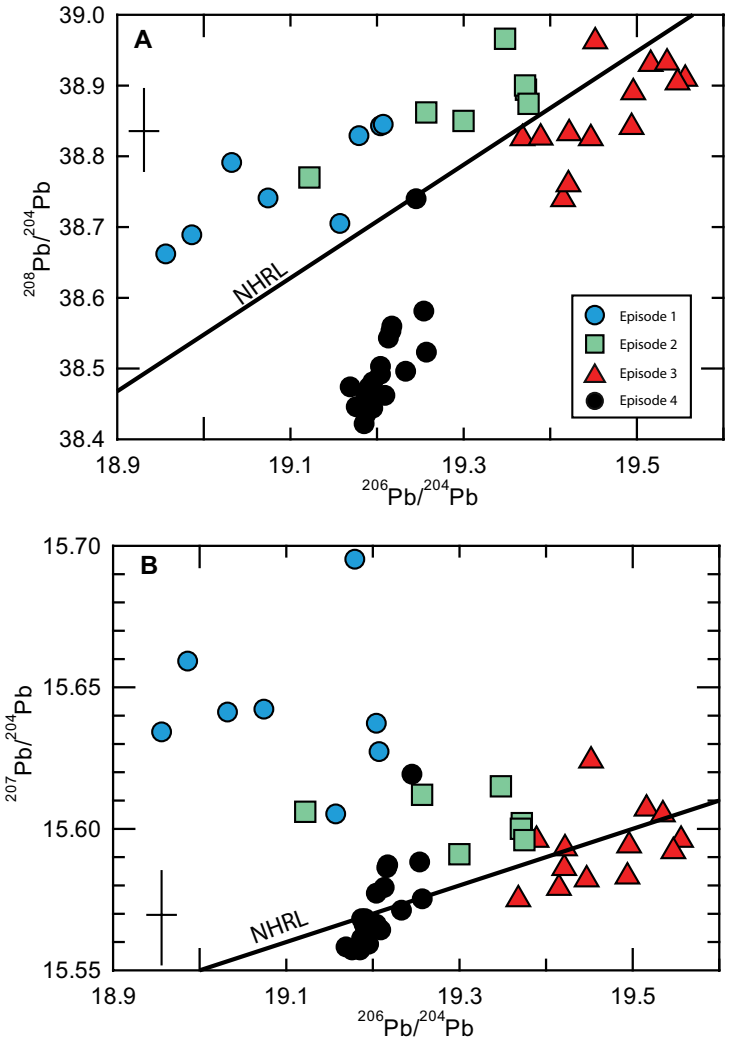

Figure 13. (A) $^{208}Pb/^{204}Pb$ versus $^{206}Pb/^{204}Pb$ for the Lunar Crater volcanic field basalts. (B) $^{207}Pb/^{204}Pb$ versus $^{206}Pb/^{204}Pb$. NHRL—Northern Hemisphere Reference Line.

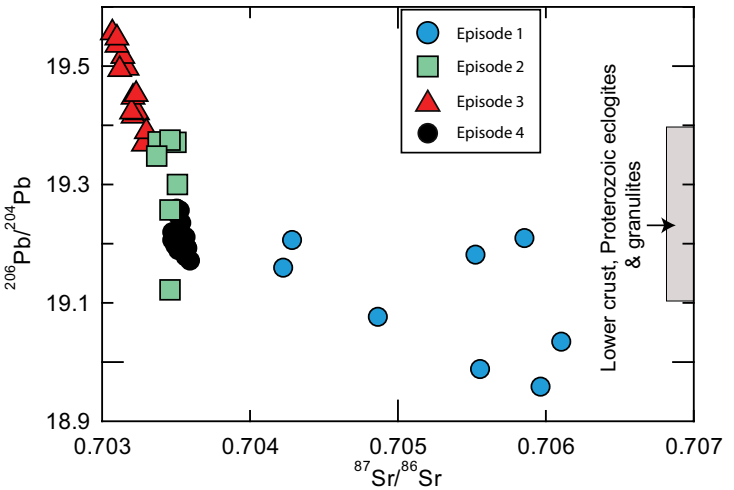

Figure 14. $^{206}Pb/^{204}Pb$ versus $^{87}Sr/^{86}Sr$ for Lunar Crater volcanic field basalts.

$^{206}Pb/^{204}Pb$, low $^{87}Sr/^{86}Sr$ (HIMU type) end member and a low $^{206}Pb/^{204}Pb$, high $^{87}Sr/^{86}Sr$ (EM type) end member that compose the episode 3 and 4 samples, respectively. Based on the combined trace element and radiogenic isotope data, these end members have been interpreted to relate to OIB-type mantle sources, including an asthenospheric HIMU-type source containing a component of recycled, dehydrated oceanic crust, and an EM-type source that likely resulted from introduction of hydrous fluids from subducted oceanic crust that further metasomatized the HIMU-type mantle (Rasoazanamparany et al., 2015).

Synthesis of Petrology and Geochemistry in Magmatic Episodes 1–4

Comparing and contrasting the four magmatic episodes provide constraints on variations through time in magma sources and processes of melt generation, melt-lithosphere interaction, and magma fractionation. Among the four magmatic episodes, MgO contents exhibit a complex temporal relationship, but on average MgO contents increase with time (Fig. 9). Crustal assimilation is only significant in episode 1 (trachybasalts) and in the 4.3 Ma trachytes, as indicated most clearly by variable and highly radiogenic Sr isotope signatures; in contrast, basalts from episode 2, as well as those from episodes 3 and 4, show no evidence for significant crustal contamination (Yogodzinski et al., 1996; Rasoazanamparany et al., 2015). The apparent lack of crustal contamination in episode 2 trachybasalts suggests that episode 2 magmas were able to ascend from source to surface and undergo fractionation with minimal interaction with the crustal basement. The near primitive compositions of many episode 3 and 4 basanites and tephrites, some of which are mantle xenolith bearing, also suggest rapid source to surface transport.

In general, the magmas also become more silica undersaturated with time (Fig. 8), with episode 1 comprising solely basalts and trachybasalts and episode 4 solely basanites (episodes 2 and 3 contain both), consistent with an overall increase in depth of melting and decrease in degree of melting with time. Higher concentrations of incompatible trace elements at a given MgO content for episode 2 basanites relative to trachybasalts (Yogodzinski et al., 1996) are consistent with a lower degree of melting to produce the basanites. Trace element patterns are consistent with OIB-type sources for the magmas from all four episodes (Fig. 10), although subtle compositional differences between episodes are observed. In a Zr/Nb versus La/Yb plot (Fig. 11), episodes 1 and 2 are characterized by high Zr/Nb relative to episodes 3 and 4, and episodes 3 and 4 are largely distinct from one another in both La/Yb and Zr/Nb. Variations in the La/Yb ratio are indicative of variable degrees of melting of a garnet-bearing mantle source, whereas variations in Zr/Nb most likely reflect a heterogeneous source composition and indicate subtle differences in chemistry between the mantle sources tapped during magmatic episodes 1 and 2 compared to that of episode 3, which in turn differs from that of episode 4. Note that the Cortés et al. (2015) model was based solely on major and trace element data, and assumed a single, relatively dry source, thus inferring that variations in La/Yb are due to variable and relatively higher degrees of partial melting (a few percent). In contrast, in Rasoazanamparany et al. (2015), the isotopic variations were interpreted to require distinct and strongly metasomatized mantle sources, such that highly incompatible trace element ratios are influenced by source heterogeneity, resulting in substantially lower (<1%) degrees of melting.

Distinctions between mantle sources tapped during the respective magmatic episodes are further revealed by the highly variable radiogenic isotope signatures observed within and between episodes. In Sr-Pb isotope space (Fig. 14), episode 3 and 4 samples were shown previously to exhibit a negative linear correlation consistent with two-component mixing between a HIMU-type and enriched mantle, EM-type mantle sources, although a gap was apparent in the trend at intermediate isotopic compositions (Rasoazanamparany et al., 2015). The episode 2 basalts have intermediate $^{87}Sr/^{86}Sr$ and $^{206}Pb/^{204}Pb$ isotopic compositions that essentially fill this gap and generally plot along the same, albeit somewhat more scattered, trend (Fig. 14). Episode 1 trachybasalts extend the range of $^{206}Pb/^{204}Pb$ to lower values, but are significantly off the trend toward radiogenic $^{87}Sr/^{86}Sr$. As a group, the episode 1–4 samples therefore appear at first glance to be consistent with two-component mixing between HIMU- and EM-type mantle sources, with episode 1 samples exhibiting widely variable and radiogenic Sr isotope signatures due to assimilation of carbonate-rich upper crust (Yogodzinski et al., 1996). Pb-Pb and Nd-Sr isotope systematics, however, indicate a more complex scenario requiring additional source components to explain the isotopic heterogeneity observed among the four magmatic episodes. In a $^{208}Pb/^{204}Pb$ - $^{206}Pb/^{204}Pb$ diagram (Fig. 13A), for example, the samples plot along two distinct trends that could reflect three-component mixing between a common HIMU-type source and two distinct low $^{206}Pb/^{204}Pb$, low $^{208}Pb/^{204}Pb$ components; $^{207}Pb/^{204}Pb$ variations, although significantly more limited (Fig. 13B), are likewise suggestive of the contribution of at least three compositionally distinct sources. Although the Pb isotope signatures of episode 1 samples could be influenced by crustal assimilation (Yogodzinski et al., 1996), the strong correlation among episode 1 samples between Sr and Nd isotopes (Fig. 12), yet complete lack of correlation between Sr and Pb isotopes (Fig. 14), indicates that the Pb isotope variations of episode 1 basalts were partly controlled by crustal assimilation and partly by source heterogeneity.

Sr-Nd isotope systematics show clearly the impact of carbonate-rich crust assimilation on episode 1 samples, and further highlight the distinctions between episode 2, 3, and 4 basalts, each of which is in a distinct compositional field with steep trends relative to that of episode 1 (Fig. 12). Proterozoic lower crust within the Basin and Range is characterized by radiogenic Sr and unradiogenic Nd and Pb (Kempton et al., 1990), as well as positive $\Delta 8/4$, and thus could contribute to the isotopic variability among episode 2 samples ($\Delta 8/4$ and $\Delta 7/4$ refer to the deviation of a sample from the Northern Hemisphere Reference Line in $^{208}Pb/^{204}Pb$ and $^{207}Pb/^{204}Pb$, respectively, at a given $^{206}Pb/^{204}Pb$; Hart, 1984). However, the common occurrence of mantle xenoliths within the episode 2 basalts suggests a rapid rise from the mantle to the surface without ponding and storage in the crust, arguing against a significant role for crustal assimilation (e.g., Foland and Bergman, 1992; Yogodzinski et al., 1996). Furthermore, assimilation of Proterozoic lower crust has been ruled out for basalts of

episodes 3 and 4, which exhibit behavior in Sr-Nd isotope space similar to that of episode 2 basalts, yet have Os isotope signatures and negative Δ8/4 signatures that are inconsistent with assimilation of local Proterozoic lower crust (Rasoazanamparany et al., 2015).

With the exception of the Sr isotope signatures in episode 1 trachybasalts, the observed trends in Sr-Nd-Pb isotope space are therefore attributed to mixing between at least three isotopically distinct mantle sources, including at least one HIMU-type source with radiogenic $^{206}Pb/^{204}Pb$, high $^{143}Nd/^{144}Nd$, and low $^{87}Sr/^{86}Sr$, and two EM-type mantle sources with low $^{206}Pb/^{204}Pb$, low $^{143}Nd/^{144}Nd$, and, respectively, positive and negative Δ8/4 and slightly different corresponding $^{87}Sr/^{86}Sr$ signatures (Figs. 12 and 13). Whether two slightly different HIMU-type sources are implied by the data trends in Sr-Nd isotope space (Fig. 12A), one associated with episodes 2 and 3, and another with episode 4, is unknown. Nevertheless, the apparent mixing relationships in each magmatic episode between a HIMU-type and an EM-type mantle source are consistent with similar processes affecting the mantle beneath the broad LCVF region, producing heterogeneity on a small spatial scale in which compositionally distinct sources are tapped throughout time and space. Our previous modeling of the Pancake Range basalts, suggesting that subduction-related mantle enrichment processes are responsible for the observed compositional and isotopic variations (Rasoazanamparany et al., 2015), may thus be applied to the larger LCVF region. In this model, mixing between a HIMU mantle source containing ancient recycled oceanic crust and an EM source related by addition of slab-derived hydrous fluid to the HIMU source, produced the compositional variations in the episode 3 and 4 basalts of the Pancake Range. A similar process could produce the isotopic signatures of the second EM-type mantle that contributed to the episode 1 and 2 basalts, if the hydrous fluid in this case contained a minor component derived from pelagic sediment (low $^{206}Pb/^{204}Pb$, positive Δ7/4 and Δ8/4). In this scenario, a regional HIMU-type mantle beneath the Pancake and Reveille Ranges, further metasomatized by compositionally variable subduction-related fluids from slab ± sediment, could explain the geochemical and isotopic signatures that we now identify within the LCVF as a whole.

Shallow Plumbing and Eruptive Products

The long lifetime of the volcanic field and the northward shifting of eruptive activity have resulted in a wide range of erosional exposure. The Reveille Range and walls of Lunar Crater maar expose some feeder dikes, the transition from dike to vent, and the internal plumbing of eroded scoria cone volcanoes. We use the term feeder dike system for dikes below, or laterally away from, the localized upward flaring that is common where vents formed, but in deeply eroded cases we cannot always clearly link such dikes with eruption centers. The plumbing information can be combined with the relatively pristine, younger volcanic surface features and deposits in the Pancake Range to develop an overall picture of the very shallow (uppermost ~150 m) plumbing structures and their relationships to eruption processes.

Feeder Dikes

Reveille Range feeder dikes. Feeder dikes exposed in the Reveille Range typically range between 1 and 3 m wide. One example (Fig. 15) can be traced laterally for ~700 m with an elevation change of 175 m on steep hillsides. In detail the lowest and southernmost exposure is a vertical dike striking N5°E that is ~70 cm wide with local additional widening of as much as 110 cm, similar to higher altitude exposures where the dike is hosted by partly welded Oligocene ignimbrite (Figs. 15A, 15B). In all places where we observed this dike it exhibits vesicle bands that are symmetrically paired with respect to the dike's center plane (Figs. 15A, 15B). We interpret this banding to result from multiple pulses of magma through the dike center, where each pulse would push the partly solidified remains of the preceding pulse to the side (see also Hintz and Valentine, 2012). In detail the dike is a series of en echelon segments that parallel the prominent jointing of the host ignimbrite and likely occupy joints; each segment can typically be traced a few tens of meters, often with minor bends in the trace, and lateral step distances between segments are <10 m. However, 240 m to the north-northeast of Figure 15A, and 45 m higher in altitude, the dike steps ~125 m to the right, and a complex network of smaller (meters to tens of meters long) dikes and sills is present between the en echelon segments. The dike then can be traced clearly up steep slopes where it intrudes ignimbrite and, in the upper parts of the exposure, an eroded scoria cone of episode 1 (Fig. 15C). The dike cuts the scoria cone remnant and postdates it, and might be related to episode 2.

Other feeder dikes exposed in the Reveille Range have less vertical exposure, but are similar in that their total map lengths are several hundred meters, and they consist of en echelon segments that are typically several tens of meters long, and with local small sills and widened zones. One such feeder dike system that is clearly linked with the Dark Peak eruptive center was described in Harp and Valentine (2015); it can be traced ~908 m along an arcuate trend that parallels a nearby Oligocene-age caldera wall structure. The dike varies in width between 1 and 3 m along its trace. Another dike system intrudes (likely Miocene) volcaniclastic rocks and can be traced 630 m (Fig. 16). It forms a set of en echelon segments that is as much as 100 m wide. Individual segments trend between ~N10°W and N15°E, with dips between ~75° and 90° both to the east and west. In detail the dike segmentation occurs on different scales; the larger scale forms 50–200-m-long segments, which are in turn broken into multiple segments of several meters to tens of meters in length (Fig. 16A). It is unclear whether this feeder dike system is related to episode 1 or 2, and it is not directly connected to any preserved eruptive centers.

Magma pressures in Reveille Range feeder dikes. For a dike in equilibrium with a brittle-elastic host medium, magma overpressure (difference between magma pressure, P_m, and horizontal compressive stress perpendicular to the dike plane, here assumed to be the regional σ_3) can be estimated by (Pollard, 1987; Rubin, 1995):

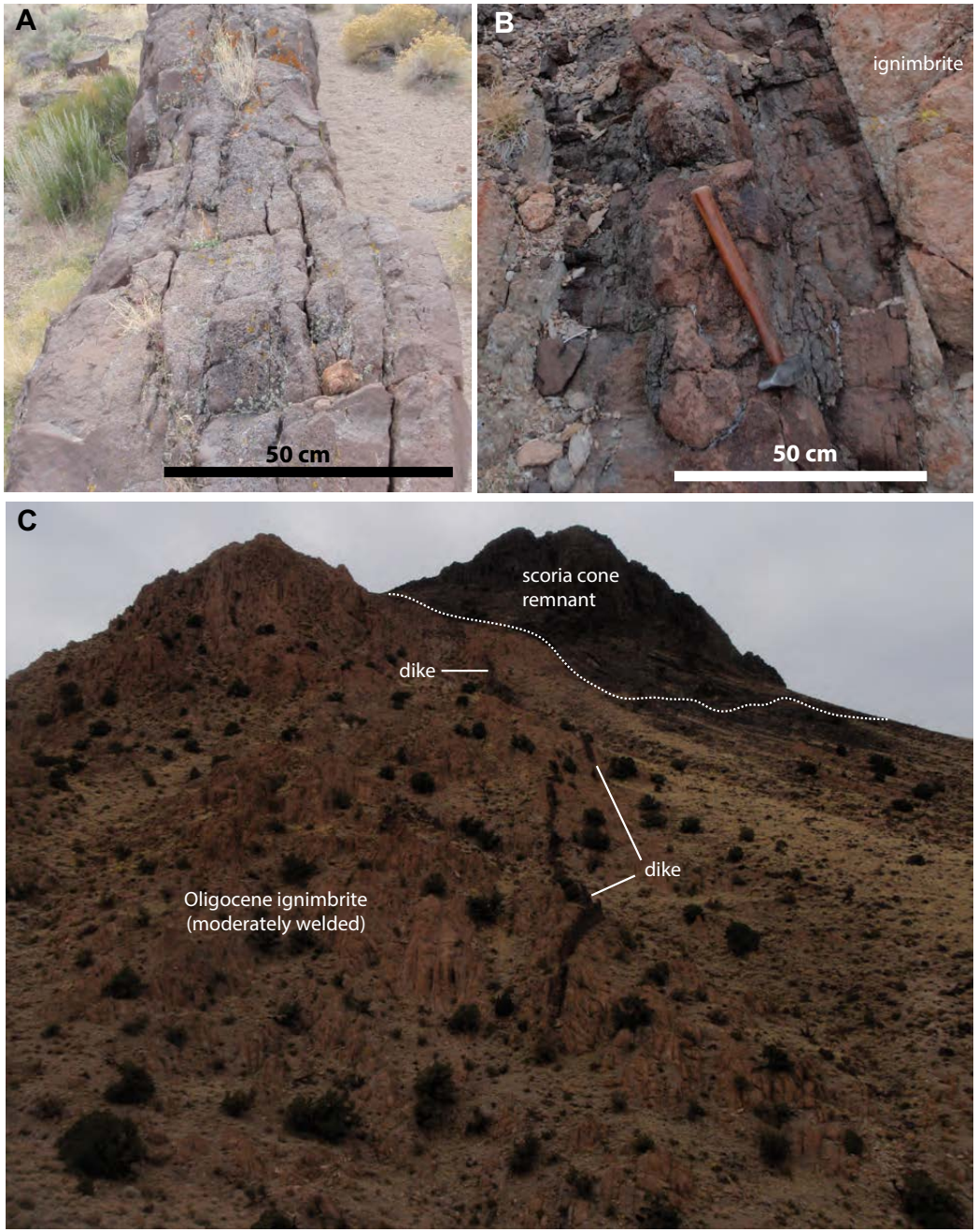

Figure 15. Feeder dike in northeastern Reveille Range. (A) The lowest and southernmost exposure is an ~70-cm-wide, tabular body rising above alluvium (38°03′33.3″N, 116°07′42.2″W, 1773 m altitude). (B) Close-up of dike intruding older ignimbrite (38°03′47.1″N, 116°07′37.5″W, 1839 m altitude). In both A and B the partings and banding are due to paired symmetric bands with different vesicularities and vesicle textures. (C) View northward at the extension of the dike intruding older ignimbrites (tan color) and episode 1 scoria cone remnant (dark outcrops at top of hillside, dotted line along contact). Note that the scoria cone erupted on the top of a steep hill carved into the Oligocene ignimbrite, and its lavas flowed down a paleoslope toward the right of the photograph that was similar to the modern slope. Vertical relief in the photo is ~150 m.

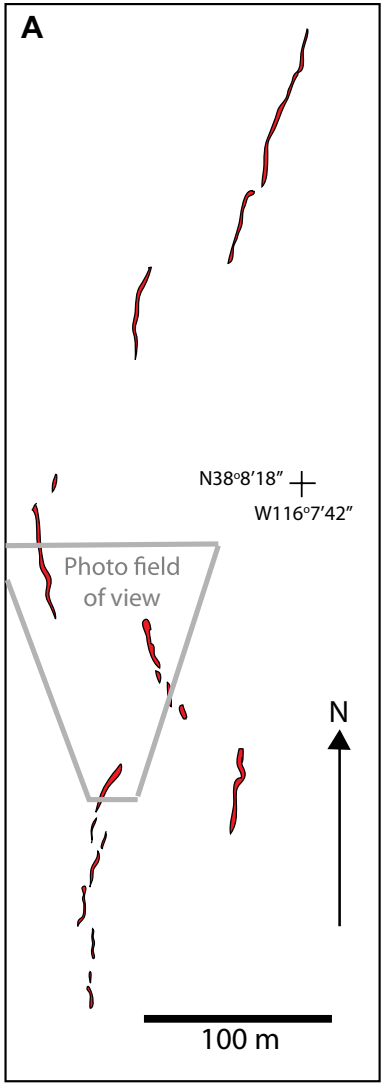

Figure 16. Feeder dike system in northern foothills of the Reveille Range. (A) Detailed map of dike set (red) illustrating en echelon character. Dike widths are typically several decimeters but are ~2 m at the widest locations. The dike system is hosted by volcaniclastic deposits. (B) Photograph showing parts of three en echelon segments (see field of view in A). Bushes in foreground are ~30 cm in diameter.

$$P_m - \sigma_3 = \frac{w}{l} \cdot \frac{\mu}{(1-\nu)}. \quad (1)$$

Here w is the dike half-width and l is its half-length. The second term on the right side of Equation 1 is the host-rock stiffness, which is determined by the shear modulus (μ) and Poisson's ratio (ν). Here we assume that the appropriate value of w is the average dike width measured on individual segments (i.e., not the width of the system of en echelon segments), and l is the length of a feeder dike system. We use these values rather than, for example, the local maximum dike widths, which are strongly influenced by host-rock variability and mechanical erosion of dike walls, and because we infer that the length of a dike system is related to the length of the feeder dike below the level at which it begins to break into small segments. For the feeder dike systems described here the typical value of $w \approx 1$ m, and $l \approx 600$–1000 m, or $w/l = 1$–2×10^{-3}. Elastic

properties of the host materials are not well constrained. For feeder dike systems within this range of *w*/*l*, hosted in moderately welded ignimbrites (e.g., Fig. 15), $\mu \approx 4$–7 GPa and $\nu \approx 0.35$ (reported for silicic tuffs at the Nevada Test Site; see Valentine and Krogh, 2006), or $\mu/(1 - \nu) \approx 6$–11 GPa. These parameter ranges give magma overpressures of 6–22 MPa. Similar feeder dike systems hosted by clastic sedimentary rocks, such as the example in Figure 16, would have overpressures of ~5–10 MPa, assuming $\mu/(1 - \nu) \approx 5$ GPa (e.g., Delaney and Gartner, 1997). In addition to uncertainties in elastic properties or the host rocks, there are many other caveats with this approach, such as (1) its appropriateness for en echelon dike systems rather than distinct, coherent dikes; (2) the assumption of mechanical equilibrium between the dike-filling magma and its elastic host; (3) whether the host medium is truly elastic, or if it can deform inelastically; and (4) whether the final dike dimensions are reflective of the dimensions during dike emplacement (see also Daniels et al., 2012). The latter is especially problematic because paired symmetric banding in the dikes is suggestive of multiple pulses of magma that contributed to the final dike widths, and because relaxation of the host rock as the magma overpressure decays at the end of an emplacement event can modify its shape. Nevertheless, overpressures on the low end of the ranges stated above seem reasonable.

Reveille Range sills. Sills associated with feeder dikes appear to be localized features at the levels of exposure available; it is not clear if these would have affected eruption processes (e.g., with respect to gas segregation processes; Menand and Phillips, 2006), and it is unlikely that they were of sufficient scale to affect petrologic processes such as shallow fractionation or assimilation (e.g., as occurred at Parícutin volcano, Mexico; Erlund et al., 2010). The sills observed along the dike that fed the Dark Peak eruptive center each occur along only ~20 m of dike length, and extend laterally as much as 15 m from the dike (Harp and Valentine, 2015). Sills exposed in cross section (Fig. 17) extend decimeters to ~10 m into the host rocks, ranging in shape from irregular and stubby to thin and tabular. These are similar in scale to small sills observed in the upper ~100 m of feeder dikes at eroded scoria cone volcanoes elsewhere in the region (e.g., Basalt Ridge; Keating et al., 2008) and likely represent the small-volume end of a spectrum of shallow sill sizes and geometries that can form in the upper few hundred meters of crust beneath monogenetic volcanoes (e.g., Valentine and Krogh, 2006; Németh and Martin, 2007; Erlund et al., 2010; Re et al., 2015; Richardson et al., 2015; Muirhead et al., 2016). Mechanisms for such sills include localized changes in the principal stresses along faults, proximity to the free ground surface which allows mechanical transla-

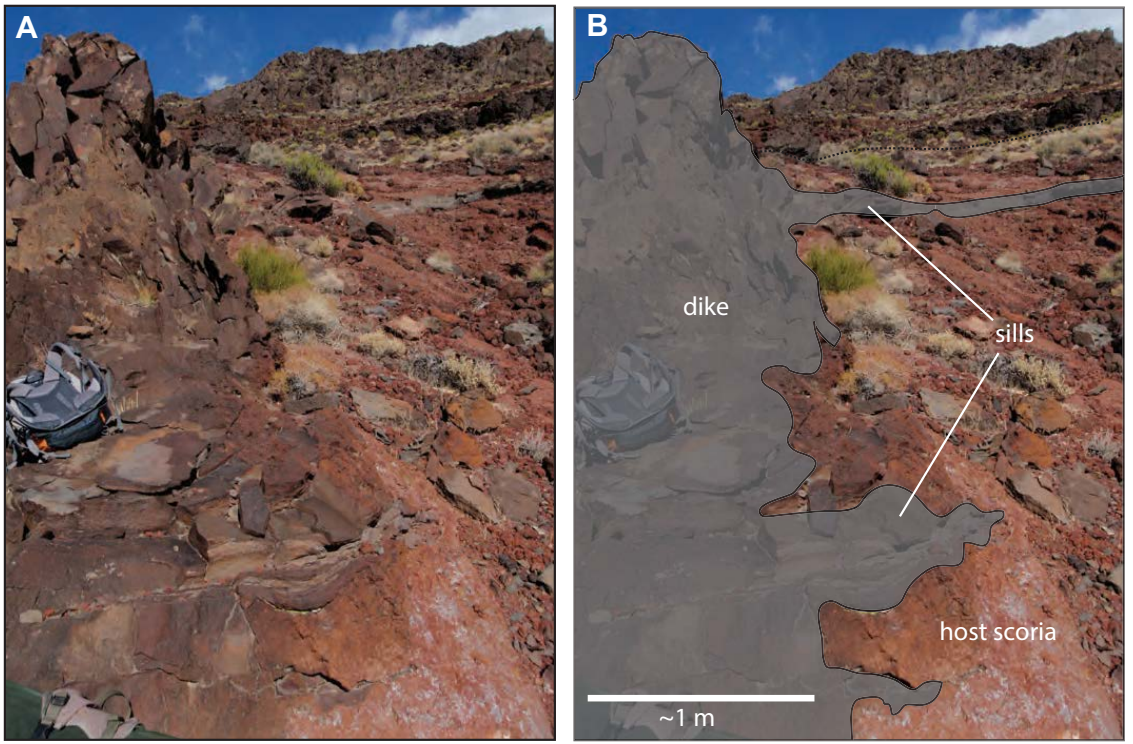

Figure 17. (A) Photograph of local sills extending laterally from a dike in the Reveille Range. This dike is likely related to episode 2 magmatism, intruding into episode 1 scoria deposits (host scoria). Uppermost cliff forming rocks shown in the photograph are related to the scoria cone illustrated in Figures 18E and 18F, and are not intruded by this dike. (B) Gray overlay enhances the details of dike-host contact and sills. Location is 38°4.181′N, 116°8.018′W.

tion of roof rock in addition to elastic deformation, interaction of dikes with bedding plane weaknesses, and others. The complex network of small sills and dikes between (but not connecting, at least with current exposures) en echelon segments of one of the feeder dikes might be related to magma filling in preexisting joints in the host tuff that dilated due to stresses between the segments.

Pancake Range feeder dikes. The younger volcanoes in the Pancake Range do not have exposed feeder dikes, but some inferences on their lengths can be made based upon crater morphologies and the details of individual eruption reconstructions (potential relationships of these dikes with preexisting faults have been discussed). Many, possibly most, scoria cone-forming eruptions begin along a fissure that represents the intersection of the feeder dike with the surface, and as an eruptive event proceeds the magma discharge commonly focuses into one or a few point sources, around which cones build and bury the earlier fissure vents. Most individual scoria cones in the Pancake Range are approximately circular or slightly elongate in plan, with no coeruptive vents beyond the cone perimeters. This means that many initial fissure vents have been completely buried by the cones and their lengths cannot be directly measured, except to say that the cone diameters are the maximum lengths of the early fissures (see also Valentine and Perry, 2006). Many of the scoria cones cluster in elongate patterns, and it can be difficult to determine whether a line of cones is from the same eruptive event, and whether they were fed by the single, contemporaneous dike system. However, through surface mapping we identified six volcanoes that certainly erupted along identifiable fissure vents, forming agglomerate ramparts rather than cones (Table 3). These ranged from 200 to 2500 m long, but the longest ones were composed of three or more en echelon fissure segments (e.g., Easy Chair; Valentine and Cortés, 2013). Assuming that the fissure lengths were similar to the feeder dike lengths (realizing that the feeder dikes might be longer, and that only a portion reached the surface), and width:length ratios were similar to those exposed in the Reveille Range, these fissure lengths suggest dike widths of several decimeters to a few meters beneath Pancake Range volcanoes.

Feeder Dike to Vent Transition and Conduits

Observations. We define the transition from feeder dike to vent to occur where the dike begins to flare as it approaches the Earth's surface. The flared portion is the vent (or conduit, without implication of plan form shape), and may contain any combination of coherent basalt, breccias, and pyroclastic material. Three locations in the LCVF expose volcanic edifices, which allow some inferences on eruption styles, and the transition from feeder dike to vent (Fig. 18). At Dark Peak (Fig. 4; Harp and Valentine, 2015), a remnant of an episode 1 scoria cone, the feeder dike transitions upward from a width of 1.4 m to an ~18-m-wide body containing domains of agglomerate and coherent basalt in the upper 15 m of crust (Figs. 18A, 18B). The Dark Peak eruption is interpreted, based upon its deposits, to have involved Strombolian to Hawaiian explosive styles, along with effusion of extensive lavas.

Excavation and collapse of the Lunar Crater maar exposed a cross section of an agglomerate rampart that extended at least 300 m to the north, approximately perpendicular to the cross section (we reserve the term spatter for deposits composed nearly entirely of fluidal and/or ragged clasts and moderately to densely welded, preferring to use the more general term agglomerate for deposits dominated by bombs but possibly with some blocks, and any degree of welding; Fisher and Schmincke, 1984). The agglomerate rampart is part of episode 4 (sample GVLC13–53; Table 1). At its deepest exposed level, the feeder dike is ~50 cm wide; the outer 15–20-cm-wide margins exhibit paired vesicle bands similar to those described here, but not as clearly developed, while the central portion of the dike consists of discontinuous centimeter- to decimeter-size vesicles and cavities with irregular shapes.

TABLE 3. ELONGATE VENT SYSTEMS

Volcano coordinates* (name if applicable)	Total length of vent system (m)	Comments
38°29′10″N, 115°58′40″W (Marcath)	850	Southern part is 400-m-long spatter rampart; northern part is an elongate cone with breached western side.
38°29′40″N, 115°58′29″W	200	Spatter rampart, possibly related to Marcath eruption but separated from it by ~700 m.
38°32′04″N, 115°56′45″W (Giggle Springs)	700	Three left-stepping en echelon spatter ramparts, each 100–350 m long.
38°31′37″N, 115°57′12″W	500	Line of 6 small 2–5-m-high spatter cones, 3 of which are on the floor of a 250-m-long, elongate crater likely from same eruptive event.
38°26′53″N, 116°01′46″W (Easy Chair)	2500	At least four left-stepping en echelon spatter ramparts, each from 300 to 600 m long; central part covered by two large cones, and southern part disrupted by maar crater.
38°31′00″N, W115°58′23″W	200	Spatter rampart with breached western side.

Note: Only vent systems with high degree of confidence of being from a single monogenetic event are included.
*Coordinates measured at the midpoint of the vent system.

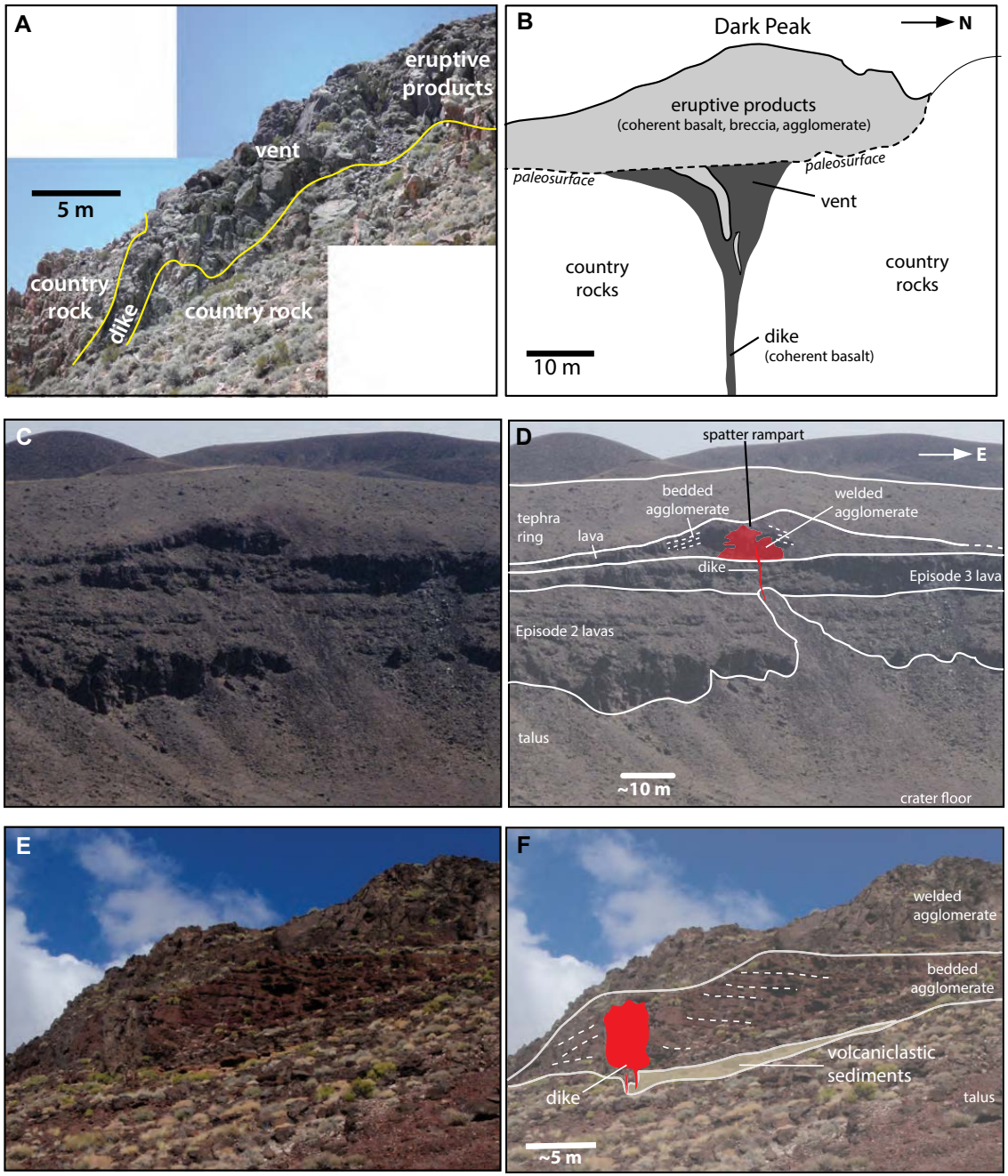

Figure 18. Examples of exposed dike to vent (conduit) transitions. (A) Oblique photo of east-facing side of Dark Peak, a scoria cone remnant (episode 1) showing upper few meters of feeder dike, upward flaring to fill a vent structure, and eruptive products. (B) Simplified sketch of the Dark Peak dike, vent fill, and eruptive products. Both A and B are based upon Harp and Valentine (2015), and are located at 38°06′51″N, 116°10′30″W. (C) Part of the northern crater wall of Lunar Crater maar, which exposed cross section of an episode 4 spatter rampart. (D) Photograph showing thin (~50 cm) subvertical dike that can be traced to ~15 m below the base of the spatter rampart. The dike widens to ~1 m within the upper 2 m of the paleosurface (the top of episode 3 lava), and extends upward and merges with a domain of densely welded agglomerate that grades laterally to bedded, progressively less welded agglomerate, and a lava flow of the same material. Location: 38°23′14″N, 116°03′56″W. (E) Oblique view of an episode 2 scoria cone remnant in the Reveille Range, which was fed by a 30–50-cm-wide, en echelon dike. (F) Photograph showing the dike, which flares to ~4 m width where it intrudes poorly to moderately welded, bedded agglomerate of the cone. Location: 38°04′16″N, 116°08′03″W.

These vesicles and cavities are lined with ropy, fluidal textured basalt. The feeder dike flares to ~2 m width in the upper 2 m below the paleosurface, and extends a few meters into its own eruptive products in the form of densely welded agglomerate with relict clasts (Figs. 18C, 18D). The transition from coherent basalt in the dike to the densely welded agglomerate is gradational over decimeters. The densely welded agglomerate in turn grades outward over a distance of meters into moderately to poorly welded, crudely bedded agglomerate, which is overlain by a lava flow (likely clastogenic) in the outer slopes of the rampart. We interpret the agglomerate rampart to have formed by accumulation of coarse clasts ejected during low fountaining or spattering with fountain heights of a few tens of meters or less (e.g., Parcheta et al., 2012). Magma flux through the narrow feeder dike was probably relatively low, with slugs of gas rising to feed the fountains. Cavities in the central portion of the dike record the final slugs as they were locked in place by the solidifying magma.

An episode 2 vent in the Reveille Range records a similar, very rapid upward transition from a decimeters-wide feeder dike into the edifice that it built (Figs. 18E, 18F). Here the dike flares no more than a few decimeters as it approaches the paleosurface (top of volcaniclastic sediments; Fig. 18F). Above the paleosurface, in the volcanic edifice, it transitions into a 3–4-m-wide body of coherent basalt that probably records a very small lava pond in the crater of the agglomerate cone that accumulated around it. The eruptive processes associated with this feeder dike and vent were likely Strombolian to Hawaiian, similar to the preceding two examples.

Comparison with other dike-to-vent data. A growing body of data shows that the widening of feeder dikes and transitions to vents for Hawaiian and Strombolian eruptions is a very shallow process, limited to the upper ~100 m of crust, and in most reported cases to the upper 20 m (Keating et al., 2008; Geshi et al., 2010; Geshi and Neri, 2014; Valentine, 2012; Friese et al., 2013; Harp and Valentine, 2015; Parcheta et al., 2015; Reynolds et al., 2016). Our observations of this transition in the LCVF are consistent with these published data. This geometry strongly contrasts with the shallow plumbing of volcanoes that likely had similar deep (>1–2 km) feeding systems, but that underwent dominant phreatomagmatic activity and formed large craters such as Lunar Crater maar, with vent structures (diatremes) that can extend downward to 2 km below the surface (White and Ross, 2011; Valentine and White, 2012; Brown and Valentine, 2013). The difference in vent structures between phreatomagmatic- and magmatic volatile–dominated volcanoes is due to strong subsurface magma-water explosions and resulting radially directed stress waves in the former, compared to more gradual upward acceleration of magma or gas slugs in the latter. Unfortunately there are no eroded maar diatremes in the LCVF to provide direct comparisons within the volcanic field.

Edifice Types and Their Internal Structures, and Maar Craters

Four types of volcanoes are well preserved in products of episodes 3 and 4 of the Pancake Range: simple central-vent scoria cones, ramparts, spatter cones and mounds, and maars. Maars are related to explosive phreatomagmatic activity, while the other three types were formed by eruptions that were driven primarily by magmatic volatiles, based upon the overall characteristics of the deposits (e.g., Valentine and Connor, 2015). Eroded cones and ramparts in the Reveille Range expose their internal plumbing structures. Two episode 2 trachytic and trachyandesitic lava domes form a fifth vent type.

Cones, ramparts, and mounds. Central-vent cones are circular to elliptical in plan, and range in basal diameter from ~300 to 1200 m (most are in the range ~600–1000 m), and heights of ~40–200 m. Cones near the smaller end of the size range occur in the Lunar Lake basin and might be partly buried beneath alluvium and playa deposits. Surface processes have substantially modified all but the youngest cones, so their morphology is no longer strictly representative of the primary volcanic processes that produced them. The cones are composed of variably welded agglomerate consistent with Strombolian to Hawaiian eruption processes. Craters that are open on one side are common and often the result of cone fragments having been preferentially rafted away on top of lavas on one side of the cone (e.g., the downhill side if the cone is erupting on a slope or escarpment; e.g., Holm, 1987; Riggs and Duffield, 2008; Valentine et al., 2006, 2007), and/or of the effects of strong wind on pyroclast dispersal. Many older craters may be breached in one quadrant due to posteruptive erosion processes.

Fissure-fed eruptions form elongate agglomerate ramparts. These are typically several hundred meters long and tens of meters high (Table 3) and consist of en echelon ramparts except in the shortest examples. Early eruptive activity at the ca. 35 ka Marcath volcano (Figs. 5, 19A, and 19B) began along a fissure system (Table 3) and built elongate ramparts on either side of the fissures. Activity focused toward the northern end of the system, building a prominent cone that partly buried the earlier formed ramparts; the total volume of cone and rampart is ~4×10^7 m^3 (note that this corrects an earlier reported volume of 9×10^7 m^3 in Johnson et al., 2014, that included a geometry error), which equates to a dense-rock equivalent (DRE) volume of ~2×10^7 m^3, assuming 50% porosity of the deposits. It is unclear whether a physically separate agglomerate rampart just to the north of the main Marcath cone is associated with the same eruption; the petrographic characteristics of the two are similar, but this is not diagnostic because most episode 4 volcanoes are petrographically similar. Easy Chair volcano (ca. 140 ka; Fig. 5) forms the longest set of agglomerate ramparts from a single eruptive event (Figs. 19C, 19D). Its eruption also began along a fissure system (Table 3), and then focused toward the center to build two overlapping scoria cones from which a small lava field emanated. Late explosive phreatomagmatic activity excavated the southern ramparts during maar crater formation (Valentine and Cortés, 2013). The ca. 130 ka Giggle Springs eruption formed low agglomerate ramparts along a 700-m-long fissure system (Table 3; Figs. 5, 19E, and 19F). This eruption did not focus toward a point source, but fed lavas that issued from both ends of the ramparts.

Additional landforms record weakly explosive to nearly purely effusive venting. Some spatter cones and mounds are associated with relatively young scoria cones and record weak, closing phases of eruptive activity. They are typically several meters high and can have steep sides with sharp peaks (e.g., Fig. 20) or more rounded shapes; the latter may have originated as more conical

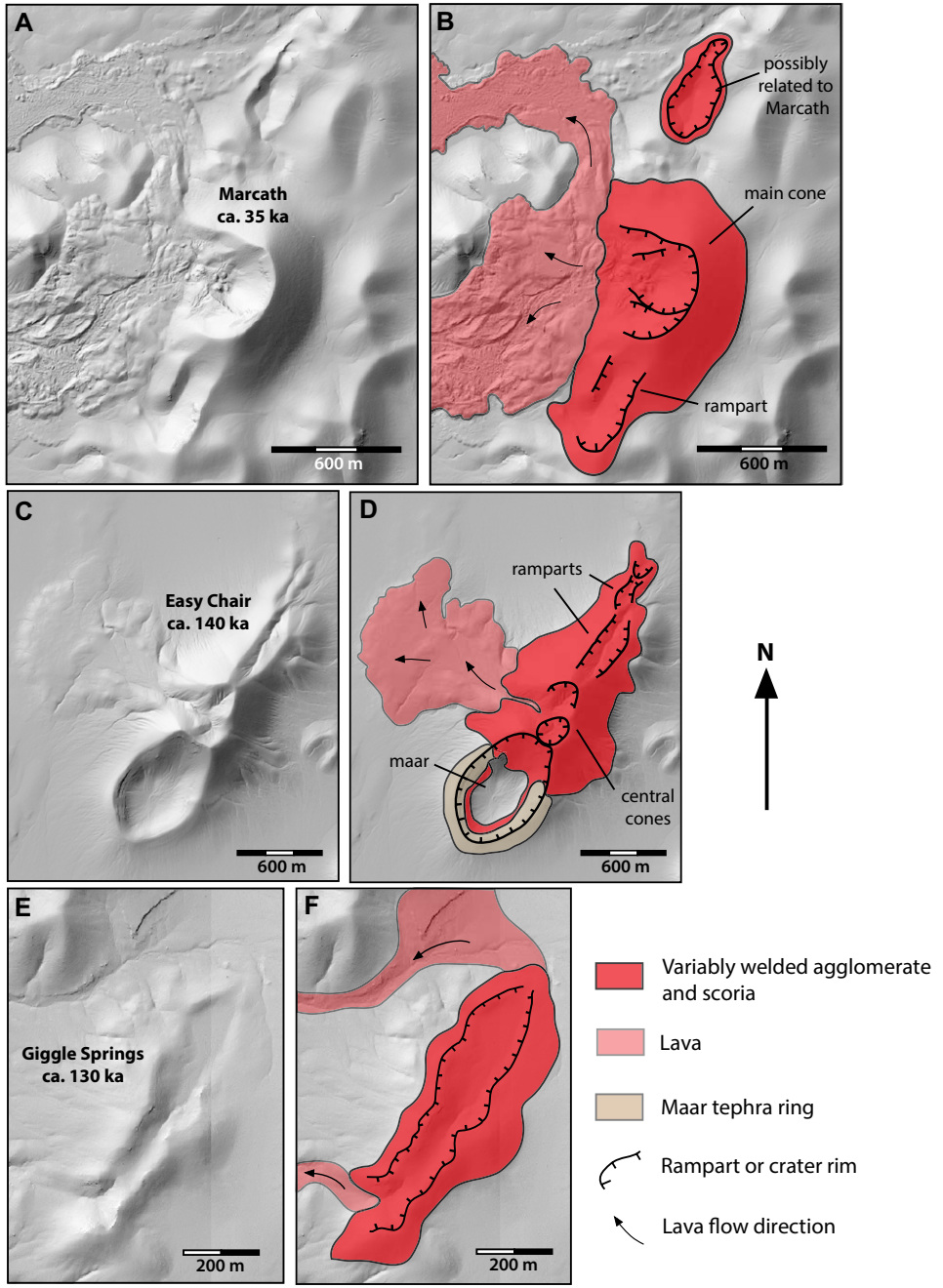

Figure 19. Examples of agglomerate ramparts (see Table 3 for coordinates). (A) Shaded relief map of the Marcath center, which began erupting along an ~850-m-long fissure system (neglecting the isolated rampart to the north, which may or may not be related to the same eruptive event), building a rampart. Eruptive activity eventually focused at the northern end, building the prominent Marcath cone. (B) Eruptive products map of the Marcath center. (C) Shaded relief map of the Easy Chair volcano. (D) Eruptive products map of the Easy Chair volcano. Eruptive activity here began along an ~2500-m-long system of en echelon fissures, building agglomerate ramparts. Activity later focused toward the center of the fissure system, building two high coalesced cones and feeding the small lava field. Phreatomagmatic explosions disrupted the southern part of the fissure system, forming a maar crater. (E) Shaded relief map of the Giggle Springs center. (F) Eruptive products map of the Giggle Springs center. Here, lavas flowed out of the two ends of the eruptive fissure system. Note different scales for each pair of maps.

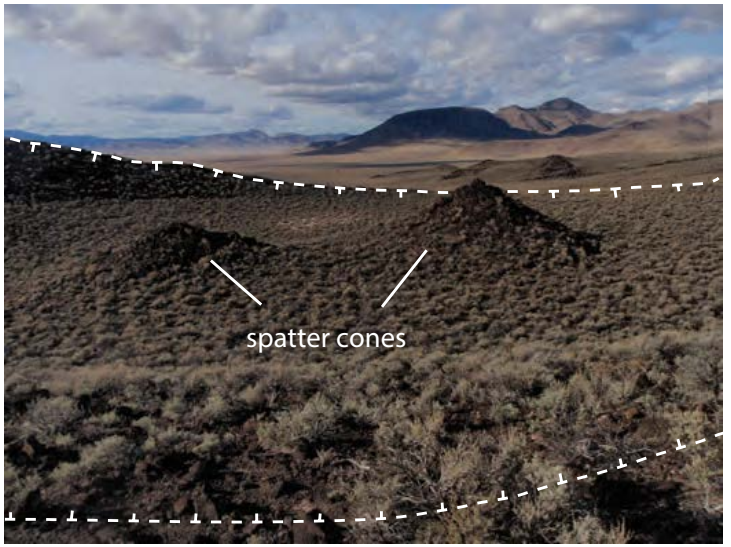

Figure 20. Two spatter cones on the floor of a larger crater (rim shown with dashed line). The largest spatter cone is ~5 m high. Location: 38°31′43″N, 115°57′06″W.

shapes but have partly collapsed and disaggregated. In one case (see Table 3; partly shown in Fig. 20) the spatter cones and/or mounds are arranged in an ~500-m-long line that extends southwestward from the floor of a larger (200 m diameter) crater. One isolated vent, ~2 km north-northeast of the Marcath cone, is an elongate spatter mound or rampart. It forms a very low profile (~5 m high, ~100 m wide) ridge ~200 m long, trending north-northeast, and might have fed a relatively young lava that extends 2.5 km to the southwest and is partly covered by Marcath lava; the large number of overlapping centers in the area and partial blanketing by Marcath tephra and alluvium make it difficult to be certain of the lava's origin. It is probable that there have been other such vents in the LCVF, but they were rapidly obscured by products from other centers due to their low topographic expression.

Internal plumbing of cones and ramparts. Old eroded centers demonstrate that cones and ramparts often have complex internal plumbing. Hintz and Valentine (2012) described the Kimana center, a remnant of a scoria cone (episode 1, Reveille Range; Fig. 4) that had a basal diameter of ~1 km and a probable height of 250–300 m. The summit of Kimana is an ~50-m-diameter area of moderately to densely welded lapilli that we infer records the main vent structure within the cone. Eight dikes and dike sets form a radial pattern around this inferred vent. Although their overall geometry is tabular with near vertical dips, in detail the dikes are composed of many segments that are meters to a few tens of meters long. Typical thicknesses are ~1 m, but the shapes of segments can be quite irregular. This is probably related to the magma, which was variably degassed, crystallized, and therefore of high viscosity, being pushed into unconsolidated scoria and agglomerate (Mathieu et al., 2008; Delcamp et al., 2014). Many of the dikes exhibit paired vesicle bands and internal quench margins, and in some cases have central portions with larger (to ~10 cm), irregularly shaped vesicles. Scoria cone remnant Dark Peak (episode 1, Reveille Range; Fig. 4), described in Harp and Valentine (2015), exposes two irregular dikes within its edifice, in addition to the transition from feeder dike to the main vent (Figs. 18A, 18B). One of these radiates from the main vent and, at its distal end where it neared the outer cone slopes during emplacement, produced bulbous intrusions several meters in size (small cryptodomes; see also Delcamp et al., 2014) and fed lava flows that vented near the cone's base. Other eroded centers in and near the Reveille Range, although not studied in detail, exhibit similar complex internal plumbing with irregular radial dikes and bulbous intrusions.

The radial dikes are interpreted to record lateral intrusion of magma driven by magmastatic pressure when magma levels were relatively high in the cone conduits. Lateral intrusions were particularly facilitated by dense, degassed magma in the conduits, which resulted in larger magmastatic pressures for given magma column heights; in many cases, the intrusion was pulsatory, as recorded by paired vesicle banding, due to pressure fluctuations in the conduits (Hintz and Valentine, 2012; Harp and Valentine, 2015). Alternatively, radial dikes might have resulted from uplift or bulging of the volcanic edifices due to intrusions, a process that opens up radial fractures that could facilitate magma migration and dike formation (van Wyk de Vries et al., 2014). Some of the radial intrusions breached the outer flanks of the cones and fed lavas, similar to those observed in historical scoria cone eruptions (e.g., Parícutin; Luhr and Simkin, 1993). In some ways the internal structures of scoria cones are scaled-down versions of stratovolcano plumbing (e.g., Swanson, 1966; Nakamura, 1977; Poland et al., 2008).

Maars. The fourth type of vents in the LCVF is maars, inferred to have formed by phreatomagmatic explosions. Of the 96 volcanoes in the Pancake Range, 4 maars have been identified (none have been identified in the Reveille Range, but it is possible that any maars there were buried in the surrounding basins). The simplest of these is Lunar Crater maar, which is an ~1100-m-diameter, 130-m-deep, nearly circular crater surrounded by a low-profile tephra ring (Figs. 5 and 21A; Valentine et al., 2011). The pre-maar landscape was a gently north-sloping surface underlain by episode 2 lavas, with episode 3 and 4 lavas, cones, and ramparts. These basaltic rocks are underlain by Oligocene silicic ignimbrites. The floor of the maar crater is ~100 m below the paleosurface, thus exposing the lavas and uppermost ignimbrite in the crater walls as well as the aforementioned rampart (Figs. 18C, 18D), and a scoria cone and dikes in its southern wall (Fig. 21B). Tephra ring deposits are poorly exposed in the crater walls due to colluvium, and are covered by a veneer of eolian sediments beyond the crater rim. The limited exposure exhibits bedded and cross-bedded lapilli tuffs composed almost entirely of clasts derived from the pre-maar lavas; ignimbrite clasts compose as much as 25% of the deposits (Valentine et al., 2011). Blocks as large as 3.3 m were ejected as ballistic clasts and occur within, and litter the surface of, the proximal tephra ring (Valentine et al., 2011).

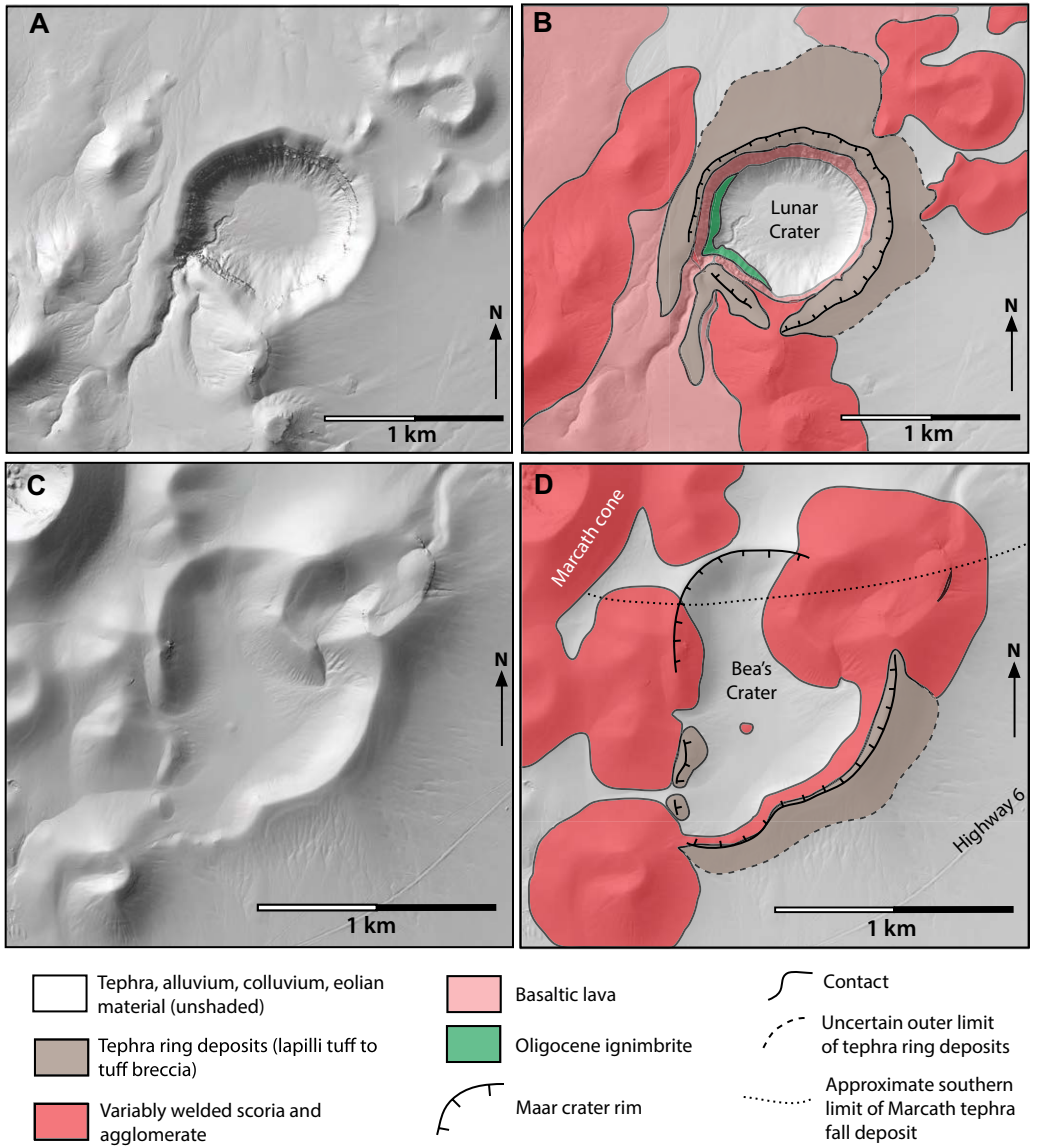

Figure 21. Lunar Crater and Bea's Crater maars (Easy Chair maar is in Figures 19C and 19D). (A) Shaded relief map of Lunar Crater maar. (B) Simple geologic map of Lunar Crater maar showing distribution of tephra ring deposits (distal edge uncertain in most locations). The crater cuts into underlying episode 2 and 4 lavas and older ignimbrite, and into a scoria cone on its southern wall. Dikes (not shown) are exposed in the latter. Coordinates of crater center: 38°23′03″N, 116°04′08″W. (C) Shaded relief map of Bea's Crater. (D) Simple geologic map of Bea's Crater. This is a compound maar with a smaller crater overlapping larger crater to the northeast. The crater cuts previous cone and agglomerate rampart deposits, but the cone that overlaps the northeast quadrant of the crater apparently partially rebuilt itself, forming a rim of agglomerate deposits that extends into the maar crater. Based upon Amin (2013). Coordinates of crater center: 38°28′43″N, 115°57′57″W.

The only clearly juvenile material observed was an occasional thin coating of basalt on ignimbrite clasts. Quartz from in situ exposures of the silicic ignimbrite in the crater wall and blocks on the tephra ring surface were analyzed for cosmogenic ^{10}Be exposure dating, which constrains the minimum age of the maar (Table 1). Lunar Crater maar is partly filled by talus from the crater walls and alluvium brought in by an ephemeral stream that enters the southwest quadrant of the maar.

Another maar, informally referred to as Bea's Crater, preserves a more complex eruptive history (Figs. 5, 21C, and 21D; Amin, 2013). It occurs in the southeastern part of a dense cone and rampart cluster that includes Marcath volcano, and as a result it disrupted at least three earlier edifices. The crater is actually composed of two overlapping craters (~440 m and ~1050 m diameter), the centers of which form a line that is parallel to the dominant north-northeast trend of ramparts and vent alignments in the area. One of the pre-maar volcanoes was an agglomerate rampart system that was likely elongated in the same north-northeast direction as nearby ramparts (such as the early deposits of the Marcath center). Most of this rampart system was located within the footprint of Bea's Crater and was destroyed, but the outer flanks are exposed along the southeast quadrant of the crater wall. The western part of the crater disrupted a cone composed of moderately to densely welded agglomerate that was relatively competent and thus forms small cliffs along the crater wall. Tephra ring deposits are exposed along the southern rim of Bea's Crater, but are covered by younger Marcath tephra in the northern part. The tephra ring deposits are massive to crudely bedded lapilli tuffs with lapilli, bombs, and blocks as large as 1.5 m, all supported in a coarse ash matrix. They are thickest (as thick as 15 m) along the southeastern part of the tephra ring. In most places 70%–80% of the blocks are angular to subangular dense basalt, while the remaining portion consists of angular to subrounded rhyolitic ignimbrite. The crater rim is interrupted by a cone in its northeastern sector. Variably welded agglomerate associated with the cone both underlies and overlies the tephra ring deposits, indicating that pyroclastic fountaining activity at the cone, driven by magmatic volatiles, was contemporaneous with phreatomagmatic maar-forming activity. The cone partly rebuilt itself after the phreatomagmatic activity, extending a new scoria cone rim into the maar (Amin, 2013), and possibly a lava flow, the top of which is exposed on the crater floor.

Easy Chair was mentioned here in the context of agglomerate ramparts (Figs. 5, 19C, and 19D); this ~540-m-diameter maar that formed at the southern end of the ramparts represents one of the closing phases of activity there. Its tephra ring is draped onto the outer rampart slopes that formed earlier in the eruption, and thus it has a steeper surface than many tephra rings. The deposits are similar to those at Lunar Crater and Bea's Crater, comprising crudely bedded lapilli tuffs with blocks derived from underlying rocks, in this case agglomerate associated with the earlier rampart-building phases, and pre–Easy Chair lavas. Clasts derived from older ignimbrites are rare (Valentine and Cortés, 2013). A thin veneer of scoria on top of the tephra ring deposits indicates minor Strombolian activity, probably vented from the central cones in the Easy Chair system, after phreatomagmatic explosions ended.

A final maar-like landform that is inferred to be related to phreatomagmatic or hydrothermal explosions is informally called Middle Maar (coordinates of crater center: 38°25′10″N, 116°01′03″W). This ~550-m-diameter crater is on top of a preexisting cluster of scoria cones, such that its floor is ~100 m above the surrounding valley floor (we refer to it as a maar because in detail its preexisting landscape was the scoria cone cluster). Material that was likely ejected during the crater-forming explosions is limited to one small, 50-m-wide drainage in the outer northeast slopes of the cone cluster. The deposits are crudely bedded and cross-bedded lapilli tuffs with isolated meter-sized blocks. Lapilli and blocks are composed of dense basalt and welded agglomerate, likely derived from the cone cluster through which the crater was excavated. Although deeper seated ignimbrite clasts were not observed in situ in the deposits, they are scattered in the colluvium at the site and probably weathered out of the lapilli tuff. The lack of other outcrops and eolian cover precludes a more detailed understanding of Middle Maar.

Discussion of maar occurrences. The four maars compose ~4% of the total number of centers in the Pancake Range; this is typical for volcanic fields in the intraplate western United States (Valentine and Connor, 2015), and the question arises, were the maars related to unique hydrologic or climatic conditions that promoted subsurface magma-water interaction? The maars are all within a few kilometers of the lowest part of the Lunar Lake basin. Lunar Crater formed in a bedrock setting (bedrock here being older basaltic lavas and Oligocene ignimbrite) ~30 m above the Lunar Lake playa, although its crater floor is lower than the playa surface (Valentine et al., 2011). Bea's Crater is ~5 km north of the playa and its floor is ~80 m above it. Easy Chair, Bea's Crater, and Middle Maar all formed on older clusters of basaltic cones and ramparts that must interfinger with basin sediments. The top of the Oligocene ignimbrites is 200–400 m below the surface (Snyder et al., 1972; Valentine and Cortés, 2013; Amin, 2013). Most of the volcanoes in Lunar Lake basin are expected to share this shallow subsurface geology, but most did not have significant phreatomagmatic activity. Thus it is difficult to speculate about any systematic hydrologic conditions that would have promoted subsurface phreatomagmatic explosions.

Climatic conditions that might have promoted such activity also are difficult to ascertain without better constraints on volcano ages with respect to potential lake stands in the past few hundred thousand years. The 140 ka age of Easy Chair is near the end of Marine Isotope Stage (MIS) 6, which was a relatively cool and wet time in the region, based upon regional paleoclimate records (Winograd et al., 1997; Jiménez-Moreno et al., 2007). One of these records, Devil's Hole, is 220 km to the south, while the other, Bear Lake, is 550 km northeast of the volcanic field. To our knowledge, little paleoclimate research spanning the interval of interest has been published for the interior Great Basin area around the LCVF. The age of Lunar Crater maar, 190–72 ka, spans both MIS 5 (dry) and 6 (wet), although we infer that it more likely occurred during MIS 5, based upon qualitative geomorphic features (Valentine et al., 2011). It is important to note that in the cases of Easy Chair and Bea's Crater, styles of activity alternated within the context of the individual monogenetic

events. This indicates that variables other than local geohydrology or climate, such as magma flux during an event, probably played the major role in determining whether phreatomagmatic or volatile-driven eruptions occurred, given the presence of groundwater (e.g., Houghton et al., 1999; Gutmann, 2002; Valentine and Cortés, 2013).

Lava domes. Remnants of two lava domes of trachytic and trachyandesitic composition occur in the northeastern part of the Reveille Range, and have ages that correspond with early episode 2; they are described briefly here (including brief petrographic descriptions, which are not elsewhere discussed for these minor products of the LCVF). The largest example corresponds to sample R8–1-43-LN (Table 1). Here dense trachyte lava is underlain by massive lapilli tuff with scattered blocks of trachyte lava and older basaltic lithics, possibly recording early explosive activity. The lava is fine grained with dominant sanidine phenocrysts a few millimeters in size in a cryptocrystalline groundmass. The main body of the lava dome is an ~700-m-diameter, irregularly shaped stack of 2 or more trachyte lavas totaling ~100 m thick (centered at N38°07′45″N, 116°06′07″W). We infer that this body corresponds to the vent location for the lavas. Two major lobes or coulees extend 700 and 900 m to the east from this body and a third coulee extends 800 m to the north. The coulees are 70–80 m thick. We infer that viscous trachytic lavas extruded on the eastern flank of the Reveille Range, first forming a thick exogenous lava dome. The two eastern coulees flowed downslope toward the Railroad Valley. The northern coulee might have been diverted around one of the thick early lobes in order to flow northward. A smaller, ~140 m diameter and ~20 m thick, remnant of a trachyandesitic dome is preserved 8 km to the south-southeast (sample R8–1-16-LN; Table 1). Lava in this dome is dense with jointing (meters spacing) that is suggestive of having originated as shear lobe boundaries in some cases. The trachyandesite is fine grained, and contains plagioclase, sanidine (both <5 mm), and clinopyroxene (<3 mm) phenocrysts often with glomeroporphyritic texture. Isolated exposures on the hillside below the dome expose as much as 50 m of trachyandesitic tuff breccia that might record a talus apron around the dome. This small dome grew on a south-facing slope that was underlain by coarse basaltic talus derived from episode 1 volcanoes on an ~200 m paleohigh just 800 m to the north. An additional trachyte lava flow is present beneath episode 2 lavas in the area, but it is only exposed in cross section as an ~10-m-thick massive lava with minor basal flow breccia, and is not discussed further.

Eruptive Products and Processes

Lavas. All lavas that we observed were either emplaced primarily as single ‘a‘ā flows or as compound ‘a‘ā fields. Flow distances for most episode 3 and 4 lavas range from ~1 to 5 km, and volumes are ~3 × 10^7 to 2 × 10^8 m^3 (estimated only for flows whose margins and thicknesses have not been obscured or eroded). Older episode 3 and most episode 1 and 2 lavas are either partly buried or eroded, and have sufficient surface modification to overprint many emplacement-related features.

Marcath lava. The Marcath lava field (Fig. 22) has a bulk volume of ~10^8 m^3 (based upon an average thickness of 15 m), similar to that of the cone and rampart. This corresponds to a DRE volume of ~8 × 10^7 m^3, assuming an average of 20% vesicularity of the lava. The flow field preserves many features related to its emplacement despite its ca. 35 ka age, reflecting the slow initial pace of surface modification of lavas in this high desert setting (e.g., Wells et al., 1985; Valentine and Harrington, 2006; Valentine et al., 2007). Lava emanated from the Marcath cone, which is situated on the edge of the aforementioned ~100-m-high escarpment that steps down to the west toward Big Sand Springs Valley. The lavas flowed westward from the crater into a saddle between the escarpment and a cluster of episode 3 cones, forming the flat-topped lava upland (Figs. 22 and 23A). Lapilli and bombs that blanket the surface, and interstitial eolian sediments, obscure detailed surface textures of the upland.

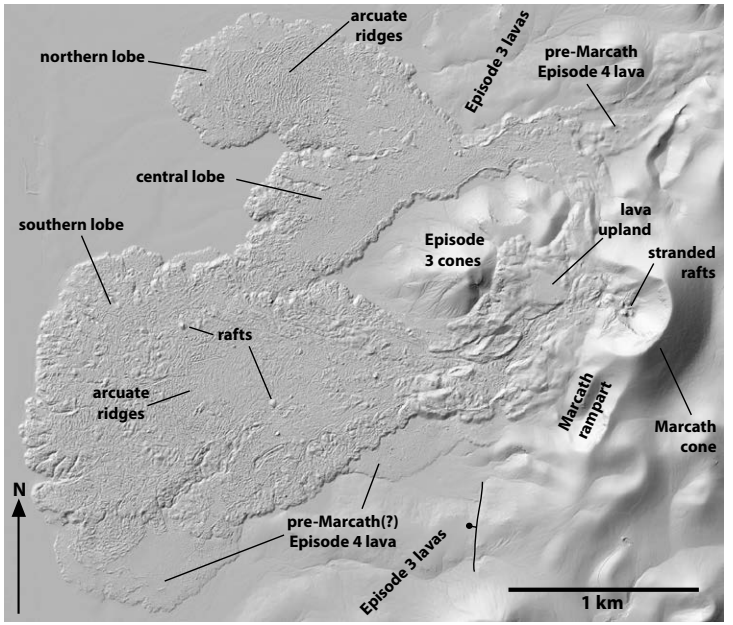

Figure 22. Shaded relief map of Marcath lava field and vent area, from airborne lidar (light detection and ranging) data. Areas labeled Marcath rampart and cone correspond to Figures 19A and 19B. Marcath lava field comprises three parts: (1) lava upland, where flows exiting the vent area stalled and inflated as they were blocked by the older episode 3 cones to the east, and the (2) northern and (3) southern lobes (in order of emplacement) that were initially fed by major breakouts on either side of the lava upland and subsequently directly from the vent. Areas labeled pre-Marcath(?) episode 4 lava adjacent to the southern lobe are low-lying areas with relatively thick eolian cover but otherwise similar petrographic characteristics to Marcath products; it is possible that this lava is also associated with Marcath and that its eolian cover is due to proximity to sediment source and lava surface texture that promotes eolian accumulation compared to other parts of the Marcath lava field. Bumps on the Marcath lava surface are rafted cone fragments; two examples are pointed out. See Table 3 for coordinates.

Figure 23. Marcath lava features. (A) Relatively flat surface of lava upland, with the Marcath cone in background. The surface is covered with scoria lapilli and bombs. Eolian sediments trapped between pyroclasts support grass. (B) Rubbly 'a'ā surface of southern lobe (grasses and bushes in photo are 10–30 cm tall). The Marcath cone is on skyline. (C) Example flow front. Base of flow is covered by eolian sand ramps. Note people for scale.

Depressed areas that occur near the edges of the lava upland are typically a few tens of meters across, and are several meters lower than the main upland surface. Flows first broke out from the northern side of the lava upland, forming an ~120-m-wide channel that fed lava down the escarpment and around the older cones onto the flat valley floor, spreading out to form the northern and central lobes. Subsequent lavas flowed southwestward in similar channels, as narrow as 40 m, to feed the southern lobe, which abuts and conforms to the edge of the central lobe (Fig. 22). The lava surfaces are rubbly 'a'ā (Fig. 23B) and preserve arcuate ridges (also known as ogives, without genetic connotation), ~1 m high, that widen downflow on the major lobes. These ridges are especially clear on the ~700-m-wide central portion of the southern lobe, and an ~500-m-wide central part of the northern lobe (Fig. 22), but vestiges of such large-scale wrinkles are found toward the outer edges of the lobes as well. Linear depressions in the flow surfaces parallel the lateral edges of the

arcuate-ridged portions of the field. Such depressions also occur in the distal hundreds of meters of the lobes, where they roughly parallel flow directions. Smaller lobes around the edge of the lava field extend tens of meters outward onto the desert floor. The lobate flow margins rise 5–15 m from the desert floor (Fig. 23C).

We infer that lavas first ponded in the saddle to form the lava uplands, possibly inflating, as suggested by the flat surface, as a pāhoehoe sheet (Self et al., 1998). Initial northbound lava may have been sourced from the inflated interior of the lava upland, but eventually lava channels connected directly to the vent area in the crater of the Marcath cone, to which they can be traced (this is especially evident toward the head of the southern lobe). Lavas accelerated down the escarpment through these narrow, 40–120-m-wide channels, promoting their development as ʻaʻā flows. The channels widened to several hundred meters when advancing lavas encountered the relatively flat valley floor. Arcuate ridges suggest broad fluid cores across the channels, and linear depressions along channel edges might result from shear zones along nearly solidified margins (similar to block lavas; Harris and Rowland, 2015). The major lobes grew outward by advancement of smaller lobes around their margins. Lava was fed to these small lobes from the broad fluid cores. In a way, lava emplacement was hybrid between pāhoehoe and ʻaʻā, in that the flows advanced across flat surfaces by advancement of lobes that stacked and interfingered and eventually merged as the broad fluid cores reached a given location; however, the surface textures are those of ʻaʻā.

All three major lobes of Marcath lava have rafts of agglomerate on their surfaces, but they are especially abundant on the southern lobe. The rafts are several meters to 20 m wide and as high as 5 m. They range from coherent bodies of bedded lapilli and bombs with different degrees of welding (Fig. 24A) to crudely bedded or massive, variably welded agglomerate (Fig. 24B), to loose mounds of lapilli and bombs. Some rafts have poorly welded or nonwelded interiors but are partially coated with a decimeters-thick layer of lava (Fig. 24C). We interpret the rafts to be material derived from the cone that was carried away on top of the lavas. The rafts shifted in orientation to varying degrees during transport, and some of them acquired lava coatings as they bobbed and rotated on the flow (accretionary lava balls of Lockwood and Hazlett, 2010). Most rafts are in early stages of degradation, surrounded by talus and coherent chunks that disaggregated from the raft during transport and subsequent weathering.

Rafting records a competition between growth of a cone by accumulation of pyroclasts, and destruction by failure and conveyance of failed material out onto a lava field (e.g., Holm, 1987; Luhr and Simkin, 1993; Sumner, 1998; Gutmann, 2002; Valentine and Gregg, 2008). The final configuration of the Marcath cone features a crater that is open to the west. Rafts might have originated from failure of the western crater wall if the wall existed during phases of eruptive activity. Alternatively, if the crater were open for the duration of activity, the rafts might have originated from periodic collapse of its oversteepened inner walls. Mounds of variably oriented, crudely bedded agglomerate in the crater near the breached side (Figs. 22 and 24D) appear to have been stranded just before exiting the crater, as lava flows waned. These mounds consist of abundant vesicular, fluidal bombs as much as 5 m long, and abundant subspherical dense bombs. The latter have diameters ranging from decimeters to ~1.5 m, and broken examples exhibit concentric layers of densely welded spatter. The cores of these bombs are in many cases simply tightly wound welded spatter, and in other cases are loose scoria lapilli or small bombs; many of them have radial prismatic joints. The subspherical bombs are interpreted to result from rapid accumulation of spatter on steep, unstable slopes. The spatter rolled back toward the vent, accreting material as it traveled (accretionary bombs; Heiken, 1978; Valentine and Cortés, 2013). The presence of large fluidal bombs and accretionary bombs in these stranded rafts is consistent with an origin of the rafts as domains of failed, steep crater walls proximal to the vent.

Comparison with other LCVF lavas. Prior to the Marcath eruption there appears to have been an ~100 k.y. gap in eruptive activity; the next youngest lavas are associated with the Giggle Springs event (ca.130 ka; Table 1). (Note that the Marcath lavas partly buried two other lavas with relatively young surface characteristics, but we did not obtain ages for these.) Thus older lavas have undergone substantially more surface modification that has obscured many details that are present on the Marcath lavas. However, the broad characteristics of all the lavas seem similar, with steep flow fronts of several meters to ~25 m high, lobate margins, and agglomerate rafts. Lavas that were erupted from topographic highs (e.g., the escarpment along the northwestern edge of the volcanic field) formed narrow, 40–100-m-wide channels on slopes of more than a few degrees, which broadened to several hundred meters width as the lavas spread onto flat (~1° or less) valley floors. Lavas erupted from vents in low-relief areas such as Lunar Lake basin spread immediately upon leaving their sources to form broad lava platforms around the cones, similar to those in the Crater Flat basin 200 km to the south (Valentine et al., 2006). Most lava fields have at least a few agglomerate rafts, in various stages of disaggregation, on their surfaces. The Giggle Springs lava field in particular has numerous rafts and most of them have lava coatings. This lava field was fed by two narrow channels, ~30 and 50 m wide, that curved between older cones on their way down the escarpment; perhaps relatively high speeds and turning flow promoted rotation of rafted domains such that they were coated with lava. Older episode 1 and 2 lavas are typically eroded around their edges and exhibit cross-sectional characteristics typical of ʻaʻā lavas, with rubbly tops and bottoms and dense cores. Where exposed, lavas that are proximal to their vents often have abundant relict, flattened clast shapes that are commonly sheared and deformed (e.g., Valentine and Cortés, 2013; Harp and Valentine, 2015). These textures do not generally occur in medial and distal exposures.

The general similarities of lava fields in the LCVF may suggest similar lava flow dynamics for most of the eruptions, with relatively high effusion rates to promote ʻaʻā flows but relatively short flow durations, probably on the order of months in most cases, reflecting the relatively small volumes, 3×10^7 to 2×10^8 m^3, of the lavas (compare with the lava volume of 7×10^8 m^3 for the historical Parícutin lavas, Mexico; Ort et al., 2008). Development of ʻaʻā was also promoted where lavas flowed down slopes such as the escarpment near the

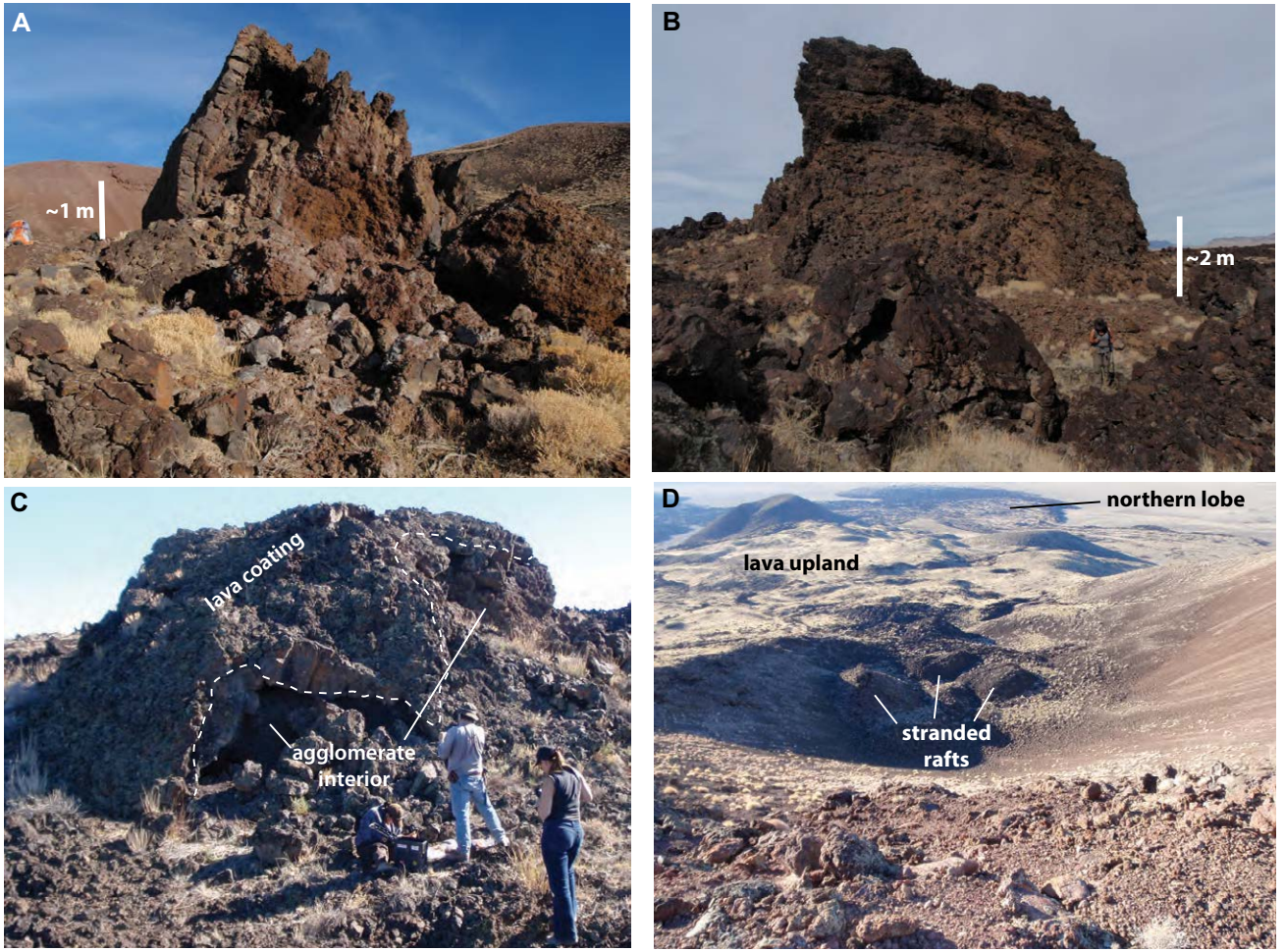

Figure 24. Agglomerate rafts on Marcath lavas. (A) Tilted raft of bedded lapilli and bombs with variable degrees of welding, occurring in proximal portion of channel that fed lava to the southern lobe. Walls of Marcath crater are in background. (B) Large, crudely bedded and partly welded agglomerate raft, within a few hundred meters of the distal end of the southern flow lobe. (C) Example of a partially lava-coated raft, with loose agglomerate interior. (D) View into crater from rim of the Marcath cone, showing rafts stranded just before exiting the crater.

Marcath cone, and the rugged paleotopography of the Reveille Range (Hintz and Valentine, 2012; Harp and Valentine, 2015). Note that effusion rate here is used as the lava volume flux feeding a flow, and does not imply that they were all fed by purely effusive activity. Many, if not most, of the lavas in the LCVF likely had significant clastogenic components fed by lava fountaining.

Proximal (cone, rampart) pyroclastic deposits. Pyroclastic deposits on inner crater walls of cones and ramparts are poorly bedded agglomerates and scoria lapilli. The deposits are dominated by juvenile clasts, many of which are recycled and/or composite bombs as evidenced by internal clastic textures (White and Houghton, 2006), while lithic clasts are generally sparse. Agglomerates include abundant fluidal and ragged bombs (e.g., Fig. 25A) with individual ribbon, spindle, and cowpat bombs as much as 5 m long. Welding ranges from nonwelded to densely welded, lava-like horizons a few meters thick and extending tens of meters laterally (Fig. 25B; Valentine and Cortés, 2013; Harp and

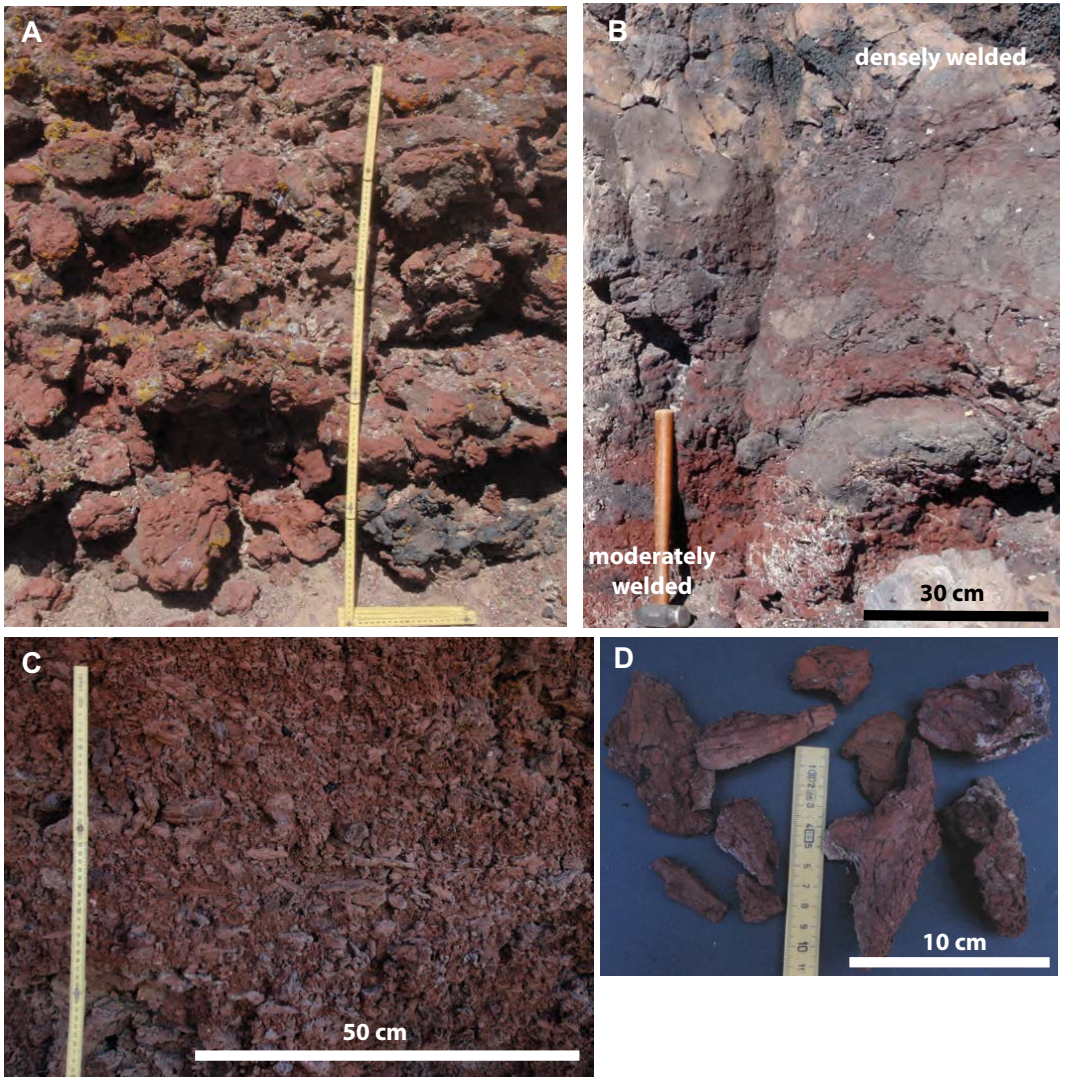

Figure 25. Proximal deposits of cones and ramparts. (A) Slightly welded (sintered) agglomerate consisting of fluidal bombs. Most are flattened parallel to bedding surface and many have ropy surface textures (Easy Chair volcano). Vertical stick is 1 m. (B) Transition from moderately welded (base of photo) to densely welded and lava-like (top) proximal agglomerate. Agglomerate rampart exposed in Lunar Crater maar wall (see Figs. 18C, 18D). Hammer is ~40 cm long. (C) Lapilli and small bomb bed, sintered. Horizontal fabric imparted by flat bombs and ribbon fragments. Measuring scale 50 cm. (D) Fluidal shapes of small bombs in same deposit as (C). Both C and D are from agglomerate rampart at Easy Chair.

Valentine, 2015). Small bomb and scoria lapilli beds (e.g., Figs. 25C, 25D) tend to be less welded than agglomerates. Deposits forming outer slopes of cones and ramparts are rarely exposed, but are generally better bedded with lenticular reverse-graded beds indicative of grain avalanches, and are mostly nonwelded and finer grained than the inner crater deposits. The eastern foot of the Marcath cone is littered with rounded bombs as much as 2 m in diameter that rolled down the slopes during cone growth. Many of these appear to be accretionary bombs, and their final size may not be indicative of the maximum bomb size that was ejected out of the crater. In general the characteristics of proximal cone and rampart deposits are consistent with Strombolian to Hawaiian eruptive styles driven by magmatic volatiles (e.g., Valentine and Connor, 2015).

Tephra fall. As with lavas, tephra associated with the Marcath eruption is the best preserved in the LCVF because younger volcanic deposits have not yet buried it, although eolian processes have modified the finer grained distal and

upper portions of its deposits. The Marcath tephra extends away from the cone in two lobes, a minor one to the south (Fig. 26A) and the more voluminous one to the east. The relationships between the two lobes, such as whether they were originally part of a broad single sheet, or if one preceded the other, are uncertain due to erosion and topography in the intervening area. Johnson et al. (2014) documented the eastern lobe, which consists of a single massive bed of well-sorted scoria lapilli in its proximal and medial reaches. Many clasts in relatively proximal areas are jigsaw pieces of bombs that broke apart upon landing. The proximal thickness of the eastern lobe (not including the cone) exceeds 4 m. The deposit is quite homogeneous at any given location, with no apparent grain-size grading, and appears to have formed during a single period of steady fountaining at the cone. Although the deposit is essentially free of lithics, megacrysts of plagioclase, olivine, clinopyroxene, and amphibole exist as free dense, unbroken clasts, which allowed estimation of eruption column height at ~7 km using the approach of Carey and Sparks (1986). This height is similar to the maximum modeled height of the 1959–60 Kilauea Iki eruption (Parfitt and Wilson, 1999), although the highest fountaining of that eruption as visually recorded was only reported as >660 m (it is not clear if this value includes a buoyant plume above the fountain; Richter et al., 1970). The bulk volume of the eastern Marcath tephra lobe is ~2×10^7 m^3. Its DRE volume is ~6×10^6 m^3, based upon a representative bulk deposit density of 750 kg/m^3 (Johnson et al., 2014). This compares with the DRE volumes of ~2×10^7 m^3 and ~8×10^7 m^3 for the cone-rampart and lava field, respectively. Thus most of the erupted mass fed lavas or was deposited proximally from fountaining, while the component of the eruption column that lofted clasts for distribution in the tephra blanket represented ~10% of the total mass. If the lavas are assumed to be mainly clastogenic (fountain fed) as well, this means that 90% or more of the erupted mass is associated with lava fountains; this aspect is also similar to the Kilauea Iki event.

Exposures of older tephra fall deposits are limited. A tephra quarry along Highway 6, near ephemeral streams that drain the Big Sand Springs Valley, exposes a >2-m-thick, well-sorted, massive scoria lapilli deposit (Fig. 26B). A bedded horizon of scoria and silt near its top suggests minor fluvial reworking prior to deposition of an overlying thinner tephra bed. The origins of the two tephra beds are uncertain, and could be from any of the several nearby scoria cones. They are overlain by bedded and cross-bedded deposits of silt, sand, lapilli, and bombs with cut-and-fill structures indicative of fluvial processes associated with the Big Sand Springs Valley drainage, and finally by a massive deposit of silt, sand, lapilli, and bombs that grades upward into a desert soil. This latter material is probably colluvium derived from degradation of a small cone that is only 300 m to the south. Such interlayering of tephra fall, fluvial deposits, and colluvium, along with other material such as playa deposits and lavas, is probably common in the subsurface of the Pancake Range. In the Reveille Range more advanced erosion has produced inverted topography, and tephra fall deposits are only rarely exposed beneath mesa-capping lavas (e.g., Fig. 26C). These locations were topographic lows at the time the tephras

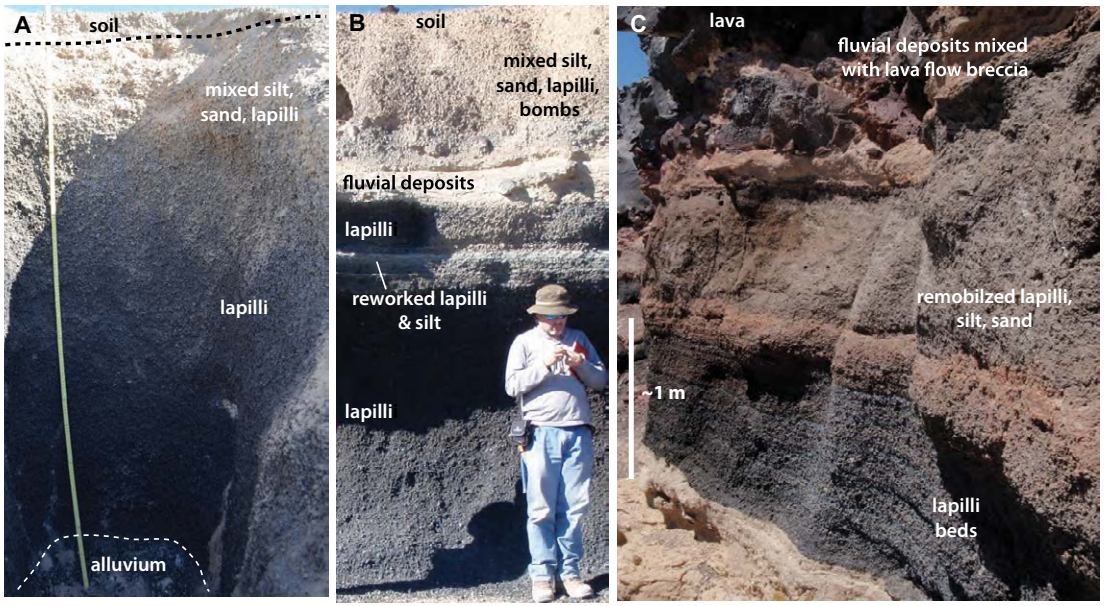

Figure 26. Example tephra fall deposits in the Lunar Crater volcanic field. (A) Southern lobe of ca. 35 ka Marcath tephra at a location 2.3 km south of the main cone (38°27′58″N, 115°58′41″W). Deposit consists of a single massive scoria lapilli bed on alluvium. It is capped by an eolian desert soil. The upper portion of the deposit contains silt and fine sand that has infiltrated from above, and the deposit is locally bioturbated (burrows). Vertical stick is 190 cm long. (B) Tephra quarry ~1 km north of the northern end of Easy Chair ramparts, along Highway 6. Lower portion is a single massive bed of well-sorted scoria lapilli, overlain by bedded silt and scoria interpreted to be reworked material, and overlain by an ~30-cm-thick massive scoria lapilli bed. Material labeled fluvial deposits is bedded and cross-bedded fine sand, silt, and lapilli, with scour and fill structures locally cutting into the underlying scoria lapilli bed. Uppermost mixed silt, sand, lapilli, and bombs are material from a nearby (~300 m to peak) eroded scoria cone mixed with eolian sediment. Desert soil (disturbed here by quarrying) with stone pavement caps the sequence. Location: 38°27′57″N, 116°01′12″W. (C) Tephra fall deposit in western Reveille Range. Planar parallel beds of well-sorted scoria lapilli in lower part of exposure are overlain by mixed silt, sand, and lapilli (reworked) and by fluvial deposits containing basalt and Oligocene ignimbrite clasts, all capped by episode 1 lava. Location: 38°01′25″N, 116°13′54″W.

were emplaced, so like the previous example they are variably reworked and interbedded with fluvial or colluvial deposits. The exposures, although limited, suggest that tephra-producing eruptions have been common throughout the history of the LCVF.

Maar-related deposits. Tephra ring deposits around the maars consist of lapilli tuffs that are dominated by shallow-derived lithics at all four maars, and isolated outsized blocks (Fig. 27). Lapilli tuffs preserve evidence of emplacement from pyroclastic density currents and ballistic curtains (Graettinger et al., 2015a), including (1) massive, poorly sorted beds (e.g., Figs. 27A, 27B); (2) thickening of deposits across pre-maar topographic lows; (3) lenticular block concentrations, likely recording ejecta rays (Graettinger et al., 2015b); and (4) local low-angle cross-stratification. Isolated outsized blocks were ejected and emplaced as individual ballistics. Block size data from Lunar Crater maar were used to estimate possible ejection velocities, which ranged between 50 and 195 m/s; the number of uncertain parameters in the calculations limited more refined estimates (Valentine et al., 2011). The general thinning of individual lapilli tuff beds upward in the section at the Easy Chair maar could be attributed to the tendency of the developing crater to focus eruption jets vertically (Taddeucci et al., 2013; Graettinger et al., 2014; Valentine et al., 2015), thus reducing the amount of material that was emplaced outside the crater for a given blast.

The dominant lithic clast types at all of the maars are previously erupted basalts either from nearby volcanoes or earlier phases of the same eruptive episode, which are also the shallowest seated (Figs. 27A, 27B). Ignimbrite clasts are most abundant at Lunar Crater, where they are sourced from as little as 30 m below the paleosurface, and at Bea's Crater (Figs. 27C, 27D). Amin (2013) estimated the depth to the top of the ignimbrite section to be ~250 m, but it is possible that ignimbrites are shallower, given the proximity of Bea's Crater to the inferred horst along which most episode 4 volcanoes erupted (see discussion of Relationships of Preexisting Structures, Vents, and Feeder Dikes in the Pancake Range). Ignimbrite lithics are sparse at Easy Chair and Middle

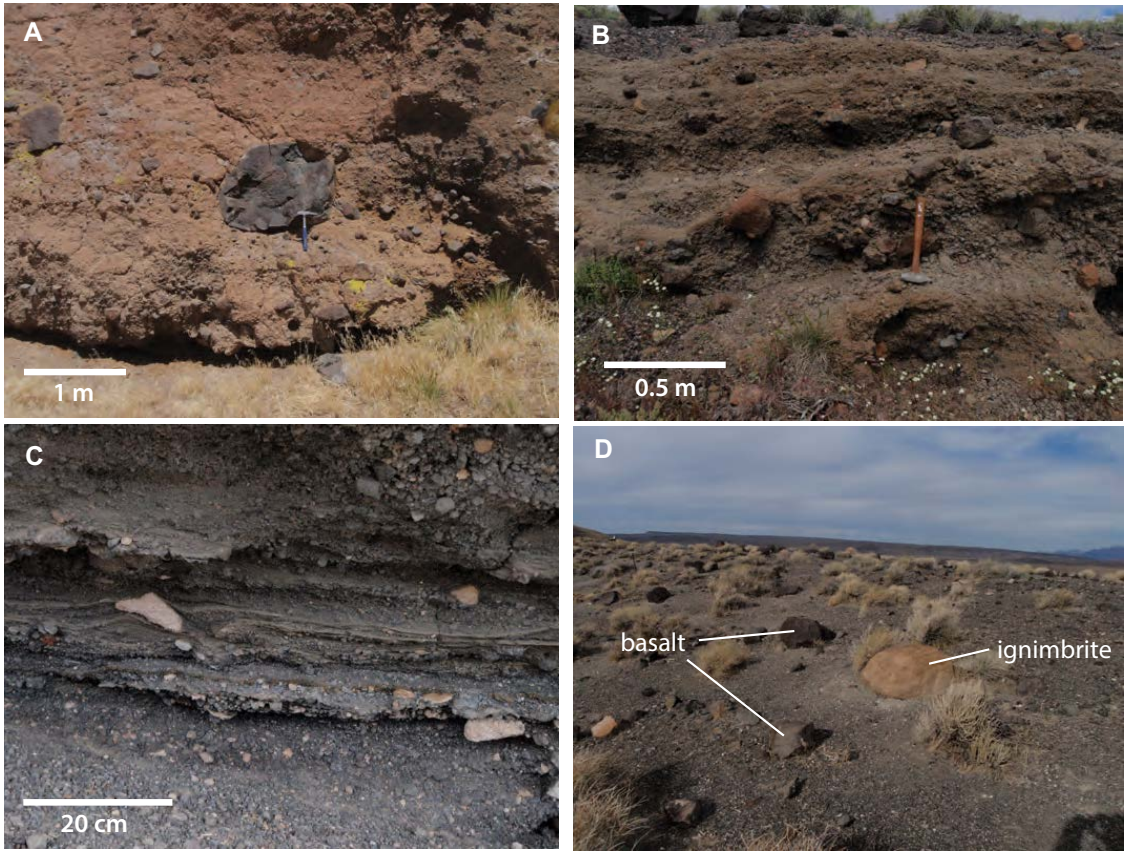

Figure 27. Maar eruption products. (A) Massive lapilli tuff at Easy Chair maar. (B) Crudely bedded lapilli tuff, Bea's Crater. Most large clasts in A and B are basaltic rocks derived from the subsurface. (C) Thinly bedded lapilli tuff with low-angle cross bedding, Lunar Crater. Light tan clasts are ignimbrite derived from the subsurface, while most other clasts are pre-maar basalts. (D) Blocks littering surface of Lunar Crater tephra ring. Ignimbrite bock is ~0.5 m in size.

Maar, where their depth is inferred to be 200–400 m (Valentine and Cortés, 2013). Traditionally, the deepest-seated lithic clasts in tephra rings have been interpreted to record the deepest level of subsurface phreatomagmatic explosions and therefore the bases of underlying diatremes (e.g., Lorenz, 1986; Jordan et al., 2013). Recent field, experimental, and modeling studies, however, indicate that these clasts only record a minimum depth of a diatreme beneath a maar (Valentine and White, 2012; LeFebvre et al., 2013; Graettinger et al., 2014; Valentine et al., 2014; Sweeney and Valentine, 2015). Deep (>200–250 m) explosions probably do not vent at the surface, but mix brecciated wall rock upward (and downward) within a developing diatreme until shallower explosions can eject the clasts. Thus the low abundances of relatively deep-seated ignimbrite clasts in Easy Chair and Middle Maar could be an artifact of: (1) the maars having undergone a relatively smaller number of subsurface explosions and less vertical mixing of the clasts, (2) generally shallower explosions, or (3) some combination of the two.

Geomorphic Evolution

The ~6 m.y. range of ages of volcanoes in the LCVF provides an excellent opportunity to improve our understanding of landform evolution in high-altitude, arid environments. The apparent similarity of dominant eruption sizes, processes, and products across that timespan further strengthens that potential, as we can assume some similarity in the initial conditions of various surfaces and landforms. Here we give a brief, qualitative overview of time evolution of topographic features (landforms) and surfaces as a starting point for more detailed and quantitative studies in the future.

Burial and Inverted Topography

Landforms evolve slowly in the high desert environment, and can be strongly influenced by structural subsidence or uplift. A number of volcanoes in the Pancake Range occur within the Lunar Lake basin (Fig. 5). Many cones and ramparts in that domain do not have associated mapped lava fields. It is likely that in most cases this is due to subsidence and alluvial filling of the basin that buries all but the youngest lavas, and eventually the cones. Similarly, as mentioned herein, we expect that there are a number of buried episode 1 and 2 volcanoes in the valleys adjacent to the Reveille Range. Lavas sourced from vents on the upthrown side of normal faults, such as may be inferred on the northwestern edge of the Pancake Range part of the LCVF, can also result in cones that have no mapped associated lava fields because the valley-filling lavas have been detached and buried in the adjacent basin.

Volcanic fields such as the LCVF produce both high-standing, relatively easily eroded landforms such as cones and ramparts, and valley-filling, erosionally resistant deposits in the form of lava fields. A common relative age indicator in volcanic fields is the development of inverted topography, and the LCVF provides excellent examples of this. The young Marcath cone rampart overlies an escarpment, and its lavas spread upon the floor of Big Sand Springs Valley to the west (Fig. 28A). Dark Peak volcano, which is several million years old (episode 1), produced a similar cone atop a paleotopographic high and a lava field that spread westward onto a valley floor that was underlain by easily eroded volcaniclastic material. Posteruption subsidence of the surrounding basins has lowered the erosional base level, such that the former valley-filling, erosionally resistant lava field now caps a high-standing mesa (Fig. 28B). While only a remnant of the Dark Peak cone is preserved, the lava field is largely intact with apparently only minor losses of material around its margins that locally expose its internal ‘a‘ā structure.

Another form of inverted topography occurs when a pyroclastic cone or rampart is partly or fully surrounded by lavas; the lavas might be associated with the cone or rampart or might be sourced at surrounding volcanoes. Cone degradation will first produce small debris fans on top of the lava. However, continued preferential erosion of the cone or rampart can eventually produce a small basin that corresponds approximately to the original footprint of the construct, surrounded by higher lava surfaces. The result is a moat-like basin with lava forming its outer wall, and a remnant of the cone or rampart in its center; this inverted topography is most pronounced where lavas from surrounding volcanoes have partly buried an earlier construct (e.g., Figs. 28C, 28D). Eventually the only remnant of the original volcano might be a plug that corresponds to its original conduit, resulting in the “neck-in-a-basin” landform of Aranda-Gómez et al. (2010).

Cone and Rampart Degradation

LCVF cones and ramparts undergo a sequence of posteruptive surficial processes in this arid environment that is similar to those documented in the broader region (Valentine et al., 2006, 2007; Valentine and Keating, 2007). If the last eruptions at a cone cover it with nonwelded lapilli and bombs, degradation at first advances very slowly as slope creep that is manifested by the development of clast garlands (Fig. 29A). During this phase most rainwater simply infiltrates into the porous cone slopes with little or no runoff. Over a time period on the order of tens of thousands of years, eolian silt and sand accumulate on the cone surface and infiltrate the interclast pore spaces of the uppermost decimeters of lapilli and bombs, while simultaneously building sand ramps at the base of some cones (Fig. 29B). Eventually this reduces the permeability of the surficial deposits and promotes nucleation of runoff, rilling, and gullying with attendant transport of cone material to debris fans that accumulate around the base of the cone or rampart. Cones with welded agglomerate beds on their outer slopes can immediately nucleate runoff and begin the rilling phase, without the time lag to accumulate eolian sediment. The fans merge through time to form a continuous debris apron composed of sand, silt, lapilli, and bombs that thickens and grows outward as the cone erodes (Fig. 29C). Continued erosion on a million-year time frame

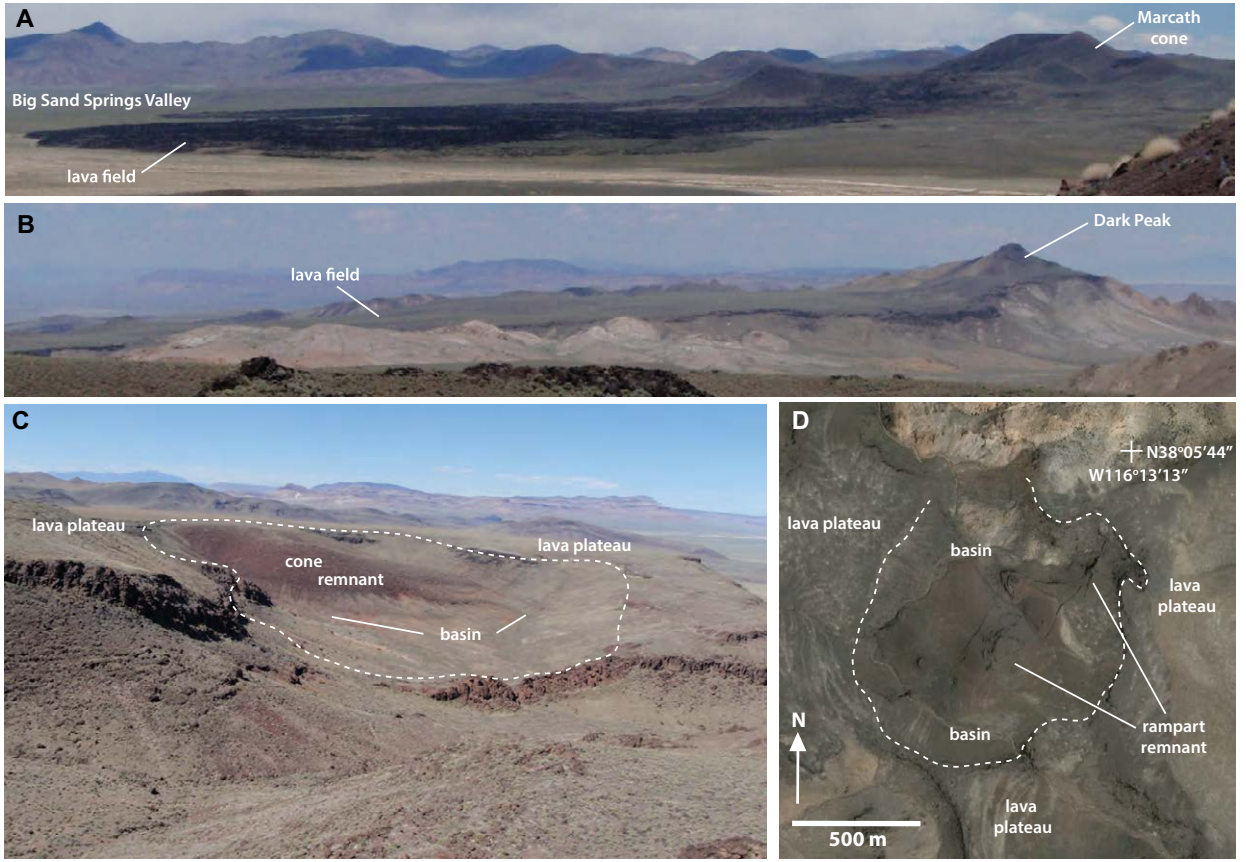

Figure 28. Examples of development of inverted topography in the Lunar Crater volcanic field. (A) View northward toward the Marcath cone (episode 4), perched on the top of an escarpment in the Pancake Range, with lava fields extending onto Big Sand Springs Valley floor. Distance from cone to distal end of lava is ~3.5 km. (B) View northward toward Dark Peak cone remnant (see Harp and Valentine, 2015) in the Reveille Range (episode 1). Distance from cone remnant to distal end of lava (near lava field label) is also ~3.5 km. Like Marcath, the Dark Peak cone formed on a topographic high and lavas flowed westward, partly filling a valley. Erosion and subsidence of valleys on either side of the range over the past few million years has resulted in inverted topography where the lava field now caps a high-standing mesa. (C, D) Examples of intermediate stages of neck-in-basin development in the Reveille Range. In C an episode 1 scoria cone was surrounded and nearly buried by episode 2 lavas. Preferential erosion of pyroclastic deposits has produced a circular drainage (moat) around the cone remnant, surrounded by lava plateaus. The diameter of the basin (edges shown by dashed line) is ~700 m. Location: 38°05′10″N, 116°07′16″W. (D) Google Earth image of a remnant of an elongate agglomerate rampart surrounded by a circular drainage and lava plateaus (dashed line shows outer edge of basin) in episode 1 deposits, western Reveille Range. In both C and D, the original footprints of the edifices are closely approximated by the outer diameter of the circular basins.

eventually removes all but the most resistant material in the cones, such as densely welded agglomerate horizons and dikes that compose a cone's internal plumbing (Fig. 29D), as discussed herein. In detail the rates of these cone degradation processes depend upon, in addition to the original pyroclastic facies (e.g., degree of welding), proximity to eolian sediment sources, post-eruptive climate variations, and local topographic setting.

Lava Surface Evolution

Lava surfaces in the LCVF, like those in other desert settings, undergo simultaneous breaking down of roughness and topographically high points (e.g., squeeze ups, agglomerate rafts), and accumulation of eolian sand and silt. In the absence of pyroclastic deposits on top of a lava, eolian sand and silt accumulate

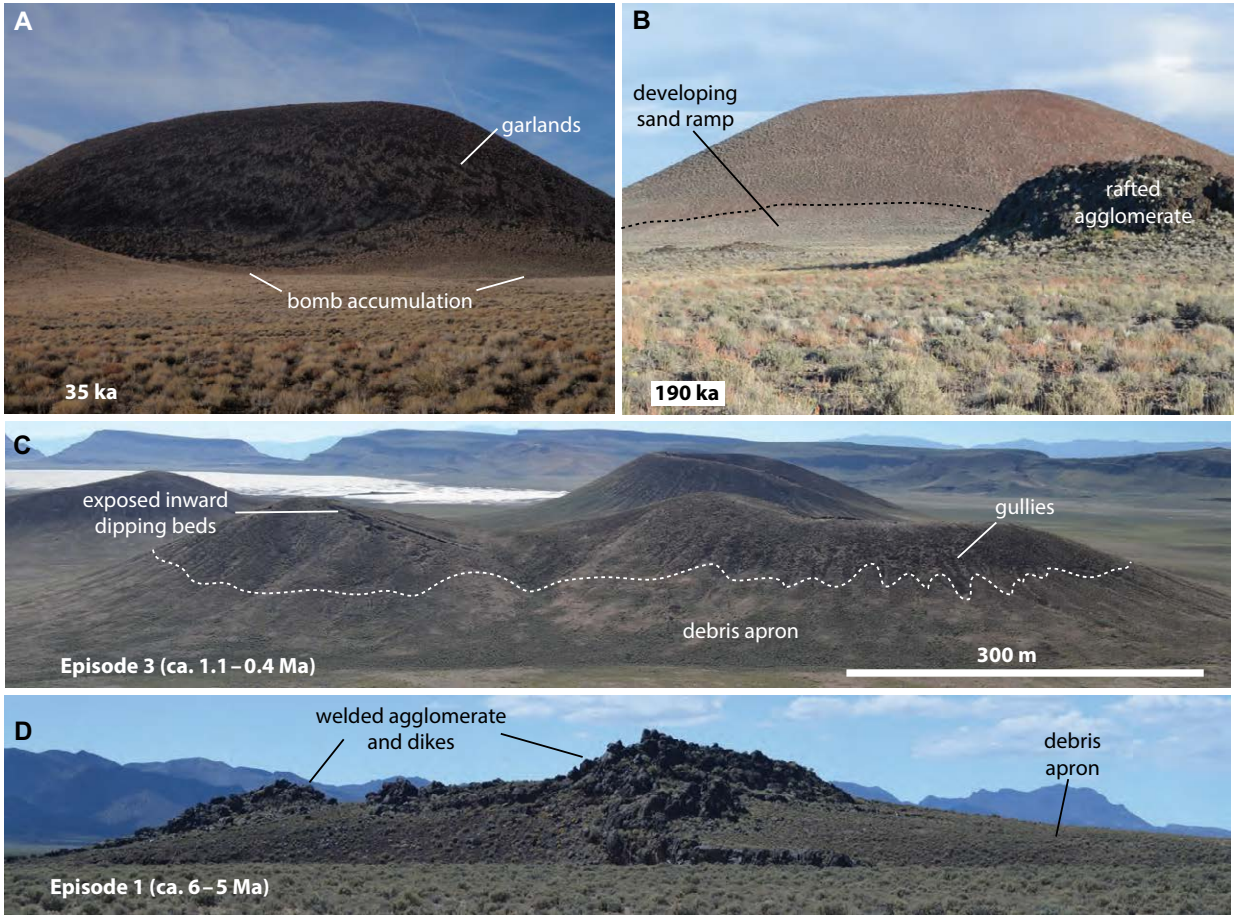

Figure 29. Changes in scoria cones through time. (A) The Marcath cone, viewed from the east, is nearly unchanged since its eruption. Its rim is slightly rounded and the cone has negligible rilling. Garland structures indicate slow creep of coarse lapilli and bombs downslope. Large (1–2 m) bombs (dominantly accretionary bombs) that accumulated around the base of the cone during eruption have not yet been buried by eolian accumulation or scoria fans. Ground surface in foreground is underlain by tephra fall. Field of view is ca. 500 m. (B) 190 ka cone near Lunar Crater maar has significant eolian accumulation on its slopes and a sand ramp draped onto its base; although not visible in this view, rills and gullies are well established on other parts of the cone's slopes and they feed small scoria fans that have accumulated at the cone base but have not yet merged to form a continuous debris apron. Field of view at distance of cone is ~300 m wide. Foreground is underlain by lava field with rafted agglomerate mounds. Mound in foreground is ca. 5 m high. (C) Episode 3 cones in Lunar Lake basin, with ages of several hundred thousand years. Gullies are well developed, and scoria fans have merged to form a continuous debris apron around the bases of the cones. Gully erosion has cut through the original outward dipping scoria beds, exposing crater-inward dipping beds, which are commonly better welded and more resistant. Lunar Lake playa and the Wall in the distance (view is to northeast). (D) Early Pliocene episode 1 scoria cone remnant in valley west of Reveille Range. Cone is mostly removed except for resistant dikes and welded agglomerate horizons. Cone remnant is ~250 m in diameter. Kawich Mountains in background.

in topographic lows, while highs gradually break down and provide clasts that become desert pavements (e.g., Valentine et al., 2007). Desert pavement in turn stabilizes eolian sediment and promotes soil development (McFadden et al., 1987). Thus lava surfaces that are initially very rough eventually evolve toward smooth surfaces (Fig. 30). During the initial tens of thousands of years after emplacement, the rates of these processes depend upon the local setting, in particular proximity to eolian sediment sources such as ephemeral streambeds and playas (cf. Figs. 30A and 23B). An additional factor is whether a lava surface starts its posteruptive evolution having been covered by tephra that provides a ready source of lapilli to form a desert pavement, beneath which eolian sediment is armored and soil formation can quickly begin (e.g., Fig. 23A; Valentine and Harrington, 2006). Carbonates precipitate in maturing soils and clay content increases with time, progressively reducing permeability and promoting runoff and development of drainage networks (Wells et al., 1985); this can be seen on many episode 3 and older lavas (Dohrenwend et al., 1987).

DISCUSSION

We have described and interpreted many individual aspects of the LCVF, from geochronology to geochemistry, spatial patterns, and physical volcanology. Here we return to the questions (posed in the Introduction) that integrate across multiple aspects of the field and have general implications for other volcanic fields.

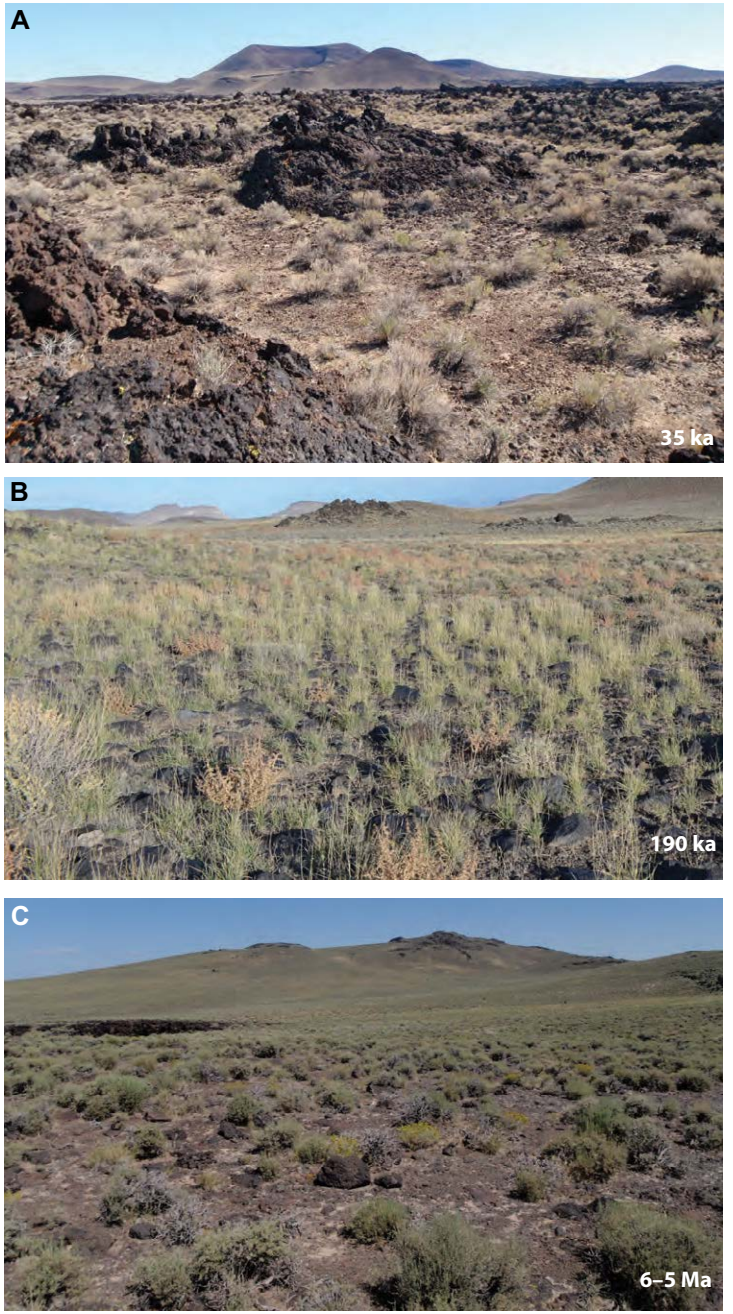

Figure 30. Lava surfaces of different ages. (A) The ca. 35 ka Marcath lava surface, looking eastward toward source cone. Photo location is near distal end of the southern lobe, where eolian sediment sourced from a dry streambed is abundant. Here eolian material has begun to fill swales between lava surface highs. The sediment is loosely covered by lapilli that either rolled off the high points and/or was lifted atop the accumulating sand and silt. High points are relatively unmodified. See Figure 23B for example of the surface farther away from the eolian sediment sources, in the interior of the lava field. (B) 190 ka lava surface. Some high points (rafted agglomerate) remain in the middle ground of this view, but most of the surface is relatively flat. Lava blocks and fragments of bombs derived from degraded high points litter the surface, while the spaces between are covered with a desert pavement of lapilli-sized fragments. The surface material is underlain by eolian sediment, which forms a developing soil. See also Figure 29B. (C) Episode 1 lava surface, looking toward the remnant of its source cone. The lava surface is completely devoid of original highs, which have all broken down, and is covered by a thick desert soil developed in eolian sediment that is armored on top by a desert pavement of lapilli and blocks.

Were the Mantle Magma Sources Homogeneous or Were They Heterogeneous in Time and Space?

The areal extent of the volcanic field–scale melting anomaly that feeds the LCVF appears to have been shrinking with time (Yogodzinski et al., 1996), although the progressive shrinking might be partly an artifact of the fact that we are only ~300 k.y. into episode 4. Previous episodes tended to have durations of ~1–1.5 m.y., thus it is possible that if episode 4 continues it will encompass a larger area. The apparent shrinking footprint of the volcanic field was accompanied by the north-northeast shifting of volcanism (Fig. 6; Foland and Bergman, 1992). The areas of episodes 2 and 3 partly overlap episodes 1 and 2, respectively, while episode 4, in its current level of development, is fully within the area of episode 3. Either (1) the different mantle source regions of episodes 1–3 only partially overlapped in plan view, or (2) if they did fully overlap their magmas were not evenly tapped in an areal sense to feed eruptions, or the magmas stalled in some areas in the lithosphere without erupting. We prefer the first, simpler interpretation, that the sources of episodes have been laterally offset from each other. This, along with the different source compositions for the episodes, implies lateral upper mantle heterogeneity on the spatial scales of the episodes (~20–40 km along the axis of the volcanic field). The asthenosphere might have advected as much as a few tens of kilometers upward and/or laterally relative to the lithosphere during the ~6 m.y. history of basaltic volcanism, distances of similar scale to the lateral shifts of episodes that could have affected the migration of volcanism. For example, different 20–40-km-scale compositional domains may have risen into the melting depth window (very loosely constrained to ~60–130 km; Cortés et al., 2015), possibly through a shear-driven upwelling mechanism (e.g., Ballmer et al., 2015). Volcanoes within a given episode, although scattered over tens of kilometers, tapped broadly similar mantle sources. However, subtle differences between the volcanoes indicate heterogeneity within episodes, on a range of scales down to hundreds of meters (Cortés et al., 2015; Rasoazanamparany et al., 2015). This makes sense in the context of the geochemistry of the source materials, which are expected to have small-scale variability due to preferential fluid and magma pathways during metasomatization. In addition, this inter-

pretation is consistent with the likely compositional origin of the seismically slow domain in the upper mantle beneath the LCVF (Fig. 2). The presence of an asthenospheric domain that is enriched in hydrous phases compared to surrounding upper mantle can also explain the unusual location of the volcanic field within the interior of the Basin and Range Province, although we do not speculate here about how the domain arrived in the area starting ca. 6 Ma.

Are There Relationships between Magma Sources, Clusters, and Preexisting Crustal Structures?

Volcano clusters and alignments in volcanic fields can be interpreted in two end-member ways in relation to their underlying mantle sources. The first end-member interpretation is that the clusters and alignments formed along preferred pathways for magma ascent. Implicit in this view is that melt production at depth may have been relatively uniformly dispersed beneath the volcanic field, but the distribution of volcanoes was determined by leaky crustal structures. This is perhaps the most common interpretation of clusters and alignments in the literature, especially when they are colocated with mappable structures (typically faults or joints) at the surface (e.g., Aranda-Gómez et al., 2003; Cebriá et al., 2011; Cimarelli et al., 2013). The leaky interpretation is problematic, however, because mechanical analyses show that it is more efficient for rising dikes to create their own paths than to occupy preexisting structures unless those structures are oriented within a narrow range of values relative to the principal stresses (see discussion of Relationships of Preexisting Structures, Vents, and Feeder Dikes in the Pancake Range; Delaney et al., 1986; Gaffney et al., 2007). This range of orientations narrows with depth; thus it is most likely for dikes to be captured within favorably oriented structures such as faults only in the uppermost hundreds of meters of the crust (Gaffney et al., 2007). In addition, to be captured by a preexisting fault at all, a rising dike must intersect it, or come within ~200 m of it (Le Corvec et al., 2013b). Dikes that ascend more than ~200 m from a fault can only follow their own paths and will not erupt along a fault. Thus, even if a fault influences the formation of a cluster, there must be a mechanism for sending dikes upward in close proximity to the fault.

A second end-member view is that clusters and alignments form over sites of relatively high melt fraction in the upper mantle; their length scales are related to the lateral length scales of these mantle source domains (so-called magmatic footprints; Valentine and Perry, 2006, 2007; Germa et al., 2013; Tadini et al., 2014). In this view the melt fraction is heterogeneous in space, and crustal structures provide secondary controls that affect rising dikes only in the uppermost kilometer or so of the crust. Our geochemical data support compositionally heterogeneous sources that could be manifested as melt-rich domains with length scales of hundreds to thousands of meters and that could be magma sources for individual volcanoes or clusters. However, we do not know of an a priori mechanism for a correlation between the map-view location of such sources in the asthenosphere and the locations of upper crustal structures at the surface. Individual volcano clusters in the LCVF had prolonged histories of several hundred thousand years or more, which has additional implications for magmatism in clusters and alignments. These time scales incorporate multiple episodes of volcanism within individual clusters. This raises questions with respect to the interpretation about source heterogeneity: if each episode was sourced from mantle with a unique geochemical signature that is internally heterogeneous (within the footprint of an episode), why would the smaller, relatively melt-rich domains that feed clusters share some locations from one episode to the next? Why would clusters be consistently elongated perpendicular to σ_3 and be closely related to crustal structure?

We suggest that LCVF feeder dikes were sourced from small melt-rich domains within the larger, episode-scale melting anomalies. Individual small-volume magma batches temporarily ponded within lithospheric mantle at or just below the crust-mantle boundary (see Cortés et al., 2015). The magma source domains might have released melt batches randomly or clustered in time and space, and the overlying small reservoirs or sills were similarly distributed (Fig. 31). Ductile deformation at the ponding interval beneath fault zones might have preferentially mobilized, or activated, magmas and triggered upward dike propagation and formation of vent clusters. These dikes ascended close enough to faults to allow for dike-fault interaction in the brittle upper crust. In map view the activation of these ponded magmas was elongate along the trends of fault zones, promoting alignments of vents at the surface and elongation of clusters. Magmas that ponded beneath locations that did not undergo deformation also sometimes ascended to the surface, but less frequently, and were not necessarily closely associated with near-surface structures. In both situations some magma batches ascended straight from their deep reservoirs near the crust-mantle boundary (e.g., episode 3), while others underwent additional temporary ponding at mid-crustal levels (episode 4).

This overall conceptual model for magma ascent, volcano clustering, and alignments (Fig. 31) is a sort of hybrid of the two views of clustering and alignments summarized in the preceding two paragraphs, but rather than faults providing leaky pathways, they are associated with preferential mobilization of ponded magmas. The fault zones are long-lived features compared to the time scales of individual eruptions or magmatic episodes, and thus could promote magma mobilization and resulting volcano clustering across episodes. It is consistent with analysis of clusters and alignments in 37 volcanic fields in a range of tectonic settings that showed that "the mechanisms of magma generation are similar to those controlling its propagation through the lithosphere" (Le Corvec et al., 2013a, p. 112), with the modification that we are suggesting mechanical activation of magmas ponded in the lithosphere rather than associating the locations of clusters with deeper mantle source domains (i.e., magma generation).

What Are the Characteristics of the Transition from Crustal Magma Transport to Eruptions at the Surface?

Exposures in the LCVF indicate that each volcano was fed by a dike or dike set; individual dike thicknesses are ~0.5–3 m. Estimated magma overpressures range from ~5 to 20 MPa; the lower end of this range is probably the most

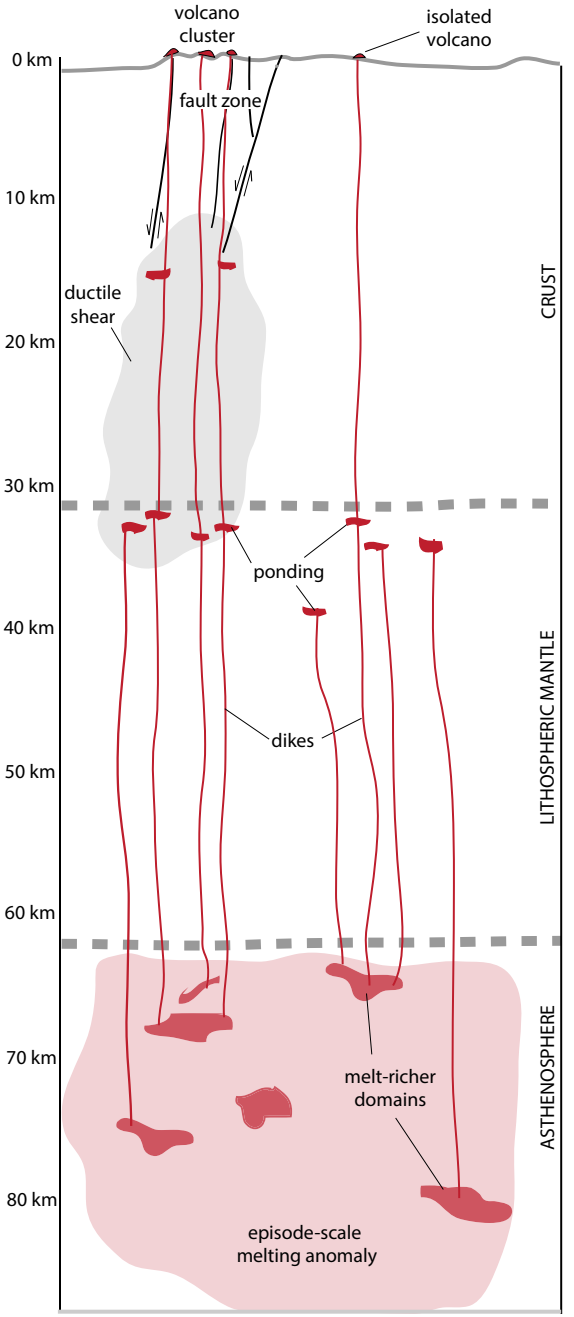

Figure 31. Diagrammatic cross section from the surface to the upper asthenosphere, illustrating hypothesized links between volcano locations and clusters, near-surface structure, and melt collection at depth for episodes 3 and 4. Diagram is roughly to drawn to scale (dike and fault widths are exaggerated). Strain in the upper crust is accommodated by brittle faulting (e.g., analogous to the graben-like domain in the northern part of the Lunar Crater volcanic field), and by ductile shear at depth (gray shaded area). A broad melting anomaly (light red shade), with length scale similar to the extent of a given episode of magmatism, contains domains with higher melt fraction (darker red areas at asthenosphere depth in diagram) due to compositional heterogeneity. Some of these domains have sufficient melt fraction on their own to propagate dikes upward. These dikes stall near the crust-mantle boundary to form small, temporary magma reservoirs (sills). Host rocks for reservoirs beneath fault zones might undergo ductile deformation (light gray area) that preferentially mobilizes magmas that feed dikes upward into the crust. These crustal dikes ascend near the faults and can interact with them in the shallow crust. Resulting volcano clusters then correlate with fault locations and are elongate parallel to the faults. Some magmas stalled at depth at locations where there is less deformation can still rise to the surface, but are less likely to for dense clusters.

realistic. The caveats mentioned above about overpressure calculations are very important to keep in mind: we are basing them on preserved dike widths and lengths, and the calculations do not account for the effects of multiple magma pulses, inelastic country-rock accommodation, or relaxation of country rock after overpressure has waned. It is not clear how meaningful the estimates are.

For magmatic-volatile–driven eruptions (Strombolian, Hawaiian, effusive), most eruptions began when a dike or dike segment intersected the surface, after which localized widening occurred that promoted focused flow and formation of individual vents. Eroded examples in the LCVF, although few in number, all show that this widening occurred only in the uppermost 10 m beneath a preeruptive paleosurface, similar to (but on the shallow side of) depths reported from other studies around the world. Magma and bubble ascent was mostly through narrow, planar dikes and dike sets until the last meters, where it was focused toward small (meters wide and deep) conduits. Genareau et al. (2010) suggested that progressive focusing of flow from a fissure vent to a central vent was responsible for increased magma speed, and therefore decreased gas segregation, and relatively sustained discharge with attendant tephra deposits at the Lathrop Wells cone, ~200 km to the south of the LCVF. Some agglomerate ramparts in the northern LCVF, vented from fissures, appear to have been dominated by relatively weak Strombolian activity consistent with efficient gas segregation and formation of gas slugs in the feeder system. At Marcath, sustained fountaining and tephra deposition were related to central vent activity after an initial phase of Strombolian activity along a fissure, which produced partly welded to nonwelded agglomerate. This suggests processes similar to the Lathrop Wells case; however, it is difficult to determine whether they were consistent across other LCVF centers due to the nature (or lack) of exposures.

These essentially three-dimensional feeding systems supported Strombolian to Hawaiian explosive and effusive activity for weeks to years, consistent with the lifespans of historical scoria cone eruptive episodes (Wood, 1980; Luhr and Simkin, 1993). Such geometry, let alone more complex examples (e.g., Valentine and Krogh, 2006; Re et al., 2015, 2016; Muirhead et al., 2016), is not what we normally think of when we describe conduit models of volcanic systems. It is likely that the very localized dike to conduit transition may, for example, have an important role in gas segregation processes that determine eruption dynamics.

How Do Individual Volcanoes Grow and Feed Various Eruptive Processes?

Individual basaltic volcanoes in the LCVF had a range of eruptive processes. For example, the Marcath volcano was constructed by relatively weak (Strombolian) fountaining along a fissure, followed by sustained high fountaining (Hawaiian) similar to that observed at Kilauea Iki (Hawaii) in 1959–1960 (Richter et al., 1970; Johnson et al., 2014). Lava flows were apparently in part concurrent with high fountaining and were probably fed by it. Growth of the main cone was a competition between accumulation of coarse pyroclastic de-

posits and localized collapses that were rafted away by the lavas. Easy Chair also transitioned from fissure-fed activity to two main vents around which high central cones developed and from which lava was emitted (also clastogenic; Valentine and Cortés, 2013). All of this took place within the context of the feeding systems discussed here. Part of the agglomerate ramparts associated with the early eruptive phase was destroyed by subsequent phreatomagmatic, crater-excavating explosions. We assume that a small diatreme extends beneath the maar crater and completely overprints the feeder dike there, at least to the base of the inferred diatreme. Internal structures in eroded cones such as Kimana and Dark Peak (Hintz and Valentine, 2012; Harp and Valentine, 2015) show that lateral intrusions within the edifices fed bocas and lava fields. This was likely promoted by the presence of dense, degassed magma in the feeding systems. The lateral intrusions both weakened their parent cones, promoting rafting of material on the lavas during eruptions, and provided resistant material that partially preserves the cones during posteruptive degradation.

Are There Relationships between Source Characteristics (e.g., Scales of Heterogeneity), the Scales and Eruptive Styles of Individual Volcanoes, and the Time-Volume Behavior of the Volcanic Field?

Geochemical and petrologic data have shown that the sources and, to some extent, ascent histories in terms of temporary crustal ponding, of LCVF magmas varied between the four episodes of magmatism. In some volcanic fields, partial melting is crudely related to volumes of individual eruptions in that larger degrees of melting (e.g., indicated by trace elements) produced larger eruption volumes (e.g., southwest Nevada volcanic field; Valentine and Perry, 2007). We do not have enough information at the LCVF to constrain whether the degree of partial melting has varied systematically, but, to the extent that we can determine given that older volcanoes are partly eroded and/or buried, the range of eruption volumes appears to have been similar across the episodes. Similarly, eruption styles have been similar with the exception of the three small evolved centers during episode 2 that formed lava domes and small coulees. Thus in the case of the LCVF we do not see relationships between eruptive scales and styles, and the magma source and ascent characteristics.

Total Eruptive Volume and Time-Volume Relationships

A key parameter in defining the long-term dynamics of volcanic systems is their time-volume behavior, normally presented as a plot of cumulative eruptive volume versus time for a volcanic field (e.g., Bacon, 1982; Kuntz et al., 1986) that in turn requires well-constrained eruption ages and reliable eruption volume estimates. Existing age data (Table 1) cover only 22%–25% of the known volcanoes in the LCVF. Volumes can only be reliably constrained for ~10 individual volcanoes; others have been partly buried by later volcanic products, are partly buried by basin-filling sediments, or, especially in the Reveille Range, have been significantly eroded. This is compounded by the possible occurrence of an unknown number of completely buried volcanoes (e.g., in the Railroad, Kawich, and Big Sand Springs Valleys, and in the Lunar Lake basin). Buried volcanoes also reduce the percentage of centers for which eruption ages have been determined, by some unknown amount.

Previous publications that compiled long-term eruptive volume fluxes for volcanic systems around the world listed the LCVF as having a total volume of 100 km^3 (Crisp, 1984; White et al., 2006). This value is based on the total area of the volcanic field (~400 km^2) and an assumed average of the volcanic products of 250 m (Bergman, 1982); no basis is provided for that assumed thickness. Given that the Marcath DRE eruption volume totals ~1.1 × 10^8 m^3 (~0.1 km^3), and that it appears to be representative of larger eruptions in the volcanic field, which contains ~142–161 mappable vents, the published total volume might be too large by a factor of ~5 (but this does not include possible buried volcanoes).

Thus while we know that the LCVF must have a long-term eruptive flux that is between the two type end members of volcanic fields (southwest Nevada volcanic field and eastern Snake River Plain; Kuntz et al., 1986; Valentine and Perry, 2007), the age and volume uncertainties are such that we cannot quantify time-volume behavior beyond estimating that the long-term flux was probably between ~3 and 5 km^3/m.y. averaged over the lifetime of the field. Tadini et al. (2014) also noted this problem, but suggested that isolated volcanoes around the periphery of the LCVF (Pancake Range) might be driven by processes akin to tectonically controlled fields that have very low long-term magma fluxes.

Comparison with Nearby Volcanic Fields

Most studies of volcanic fields in the interior southwestern United States have focused on petrogenesis; only a few have also been the subject of physical volcanological studies. Here we very briefly compare magma source, ascent, and volcanology (where it has been studied) between the LCVF and volcanic fields in the region, keeping in mind that the LCVF is relatively isolated even from those fields.

The Big Pine volcanic field (Fig. 1) is located ~200 km west-southwest of the LCVF, at the boundary between the Basin and Range Province and the Sierra Nevada. The Big Pine field includes ~24 basaltic volcanoes with abundant mantle xenoliths, and one silicic center, with ages ranging from 1.2 to 0.035 Ma (Blondes et al., 2008). Many of the volcanoes occupy young normal faults. The basaltic volcanoes comprise scoria cones with lava fields and are similar in size to those of the LCVF. Gazel et al. (2012) concluded that the asthenospheric melting interval has shifted upward (from 60–80 km to 30–55 km) during volcanism in concert with the shallowing asthenosphere-lithosphere boundary (defined seismically); younger (post–500 ka) magmas also bear evidence of having interacted with lithospheric mantle. Gazel et al. (2012) suggested that relationships between magmatism, vents, and structures are related to lithospheric deformation (faulting at the surface), perhaps similar to our interpretation of at least some aspects of the LCVF (Fig. 31). Blondes et al. (2008) concluded from

isotopic studies that the source mantle was heterogeneous. It is interesting that one of the eruptions captured the full range of source characteristics that are represented in the field as a whole; this might reflect vertical heterogeneity that could be variably captured as magmas collected within ~20-km-thick melting intervals.

The Buffalo Valley volcanic field (Fig. 1; Cousens et al., 2013), like the LCVF ~230 km to the south-southeast, is located in the interior of the Basin and Range Province rather than near its edge. It consists of ~15–20 basaltic scoria cones and lava fields with compositions from alkali-rich basalt to trachybasalt. The field had two episodes of magmatism, both of which were sourced in asthenospheric mantle. The Pliocene episode (4.02–2.75 Ma) erupted magmas that originated at relatively shallow depths in the asthenosphere, indicated by the absence of a garnet signature in trace element compositions. Quaternary episode (1.99–0.07 Ma) products, however, have a compositional signature consistent with garnet in the source mantle. Thus melting appears to have deepened with time (Cousens et al., 2013). Volcanoes of Quaternary age are clearly colocated with faults that bound the Fish Creek Mountains, potentially supporting our conceptual model linking crustal faulting with melt collection at depth.

The Hurricane volcanic field is located ~250 km east-southeast of the LCVF, just in the Colorado Plateau Province (Fig. 1; Smith et al., 1999). Colorado Plateau lithosphere and crust is much thicker (>120 km and 40–50 km, respectively; e.g., West et al., 2004) than in most of the Basin and Range because it has not been extended and thinned. The small field contains ~10 scoria cone volcanoes with attendant lava fields, with individual volumes of 0.05–0.3 km^3. Pyroclastic deposits are consistent with Hawaiian and Strombolian explosive styles, accompanied by lava effusion. Compositions are basanites and alkali basalts. Age dates range between 353 and 258 ka (Smith et al., 1999), although eroded remnants suggest some older volcanism as well. Hurricane magmas are inferred to have originated by partial melting of heterogeneous lithospheric mantle (Smith et al., 1999), differently from the LCVF asthenospheric sources. The lithospheric mantle source was compositionally heterogeneous at scales of ~1 km (or less) in plan view. The volcanoes are closely associated with faults and one of them is cut by the Hurricane fault, a major normal fault associated with the transition from Colorado Plateau to Basin and Range tectonics to the west.

The southwest Nevada volcanic field (Fig. 1) includes 17 Pliocene–Quaternary monogenetic volcanoes (Valentine and Perry, 2007). Compositions include alkali basalts to trachyandesites, and are consistent with most of the volcanoes having been fed by magmas that ascended relatively directly from their source depths to the surface (one exception has evidence for storage and fractionation in the crust prior to eruption). Trace elements define two major magmatic episodes. The first one produced three volcanoes of relatively large volumes (~2.5, 1.2, and 0.6 km^3), and several smaller volume centers that are now buried beneath basin fill. Ages for this first episode are between 4.63 and 3 Ma. Younger volcanoes are all smaller than 0.1 km^3 with 2 exceptions at 0.84 and 0.12 km^3. Trace elements indicate that the older episode was related to a larger degree of partial melting than the younger one. All of the magmas were sourced in enriched, old (Precambrian), and compositionally heterogeneous lithospheric mantle, which extends to depths of ~125 km (Schulte-Pelkum et al., 2011). Note that this area, referred to as the central Basin and Range, began extending significantly later than most of the province, such that its crust and lithosphere has not thinned as much. Apparently all of the feeder dikes were captured by north-south–trending, Miocene-age faults as they approached the surface. This volcanic field was proposed as the type example of a tectonically controlled field, where melt collection in relatively melt richer domains of lithospheric mantle was dominantly in response to regional tectonic deformation (Valentine and Perry, 2007). The Quaternary long-term eruptive magma flux is extremely small, ~0.5 km^3/m.y. Eruption styles included Hawaiian, Strombolian, and violent Strombolian explosive activity, as well as lava effusion.

Of the volcanic fields summarized here, two (Big Pine and Hurricane) are at or near the margins of the Basin and Range Province. The Buffalo Valley and southwest Nevada fields are in the interior of the province. Like the LCVF, all of these fields were fed by magmas sourced in heterogeneous upper mantle, be it asthenospheric or lithospheric, with heterogeneities extending to small scales such that closely spaced volcanoes have slightly different source compositions. As shown in McGee and Smith (2016), small-scale compositional heterogeneity of source mantle appears to be a common characteristic of small-volume volcanoes fed by low degrees of partial melting. These heterogeneities produce small-volume domains of partial melt that in turn feed small-volume volcanoes. In many cases the magmas ascend relatively quickly; even if they temporarily pond in the crust, their small thermal budgets work against significant assimilation of host rock (see Cortés et al., 2015). In this way the volcanoes are able to preserve the subtle source variability. All of the fields exhibit close links between surface faulting and volcano location, consistent with our conceptual model (Fig. 31).

SUMMARY AND CONCLUSIONS

The LCVF is similar to many volcanic fields in the interior western United States. It is dominated by monogenetic basaltic volcanoes (in this case with a very minor component of lava domes and flows with evolved compositions). The volcanoes number 142–161 and span ~6 m.y. in age, with the most recent only ca. 35 ka, indicating that the field is likely to produce future eruptions. The most common volcanic landforms are scoria cones, agglomerate ramparts, and ʻaʻā lava fields. The volcanoes were fed at depth by dikes that occur in en echelon sets and that preserve evidence of multiple pulses of magma. The dikes locally flared in the upper ~10 m of the crust to form shallow conduits that fed eruptions. Volumes of individual eruptions were typically ~0.1 km^3 and smaller. Eruptive styles were dominantly Strombolian to Hawaiian, the latter producing tephra fallout blankets, with effusive activity (although many lavas were likely clastogenic and associated with lava fountains). Phreatomagmatic maar volcanoes compose a small percentage of the landform types; we are unable to identify any clear hydrologic or climatic driver for the phreatomagmatic activity, suggesting that intrinsic factors such as magma flux played an important role.

Volcanism in the LCVF occurred in four magmatic episodes; each successive episode shifted northward but partly overlapped the area of its predecessor. The areas encompassed by the episodes appear to be progressively shrinking, although this may be partly an artifact of episode 4 having not yet fully unfolded. Asthenospheric mantle was the source throughout LCVF volcanism, but each episode was derived from a specific source composition. Thus the episodes record large-scale (length scales of tens of kilometers) heterogeneities in the upper mantle. The longevity of the volcanic field is such that advection of different compositional domains into the melting region might have been important. Geochemical evidence suggests subtle source heterogeneity at the scales of hundreds of meters to kilometers within each episode-scale area of activity; episode 1 magmas also underwent contamination by Paleozoic carbonates during temporary ponding in the crust. The LCVF, like most volcanic fields, exhibits clustering of vents that we relate to domains of elevated partial melt content in the asthenosphere, consistent with the heterogeneous source compositions. Magmas underwent temporary ponding near the crust-mantle boundary, and we infer that these were preferentially mobilized by ductile deformation of host rocks; this is in turn represented by faulting at the surface. Thus clusters could persist from one episode to the next, and their locations are closely related to crustal structures. Clusters result in overlapping and colocated monogenetic volcanoes that are separated by variable amounts of time, but that record different mantle sources (between episodes) without having shared, sustained crustal reservoirs. The total volume and time-volume behavior of the LCVF cannot be determined by surface observations due to erosion and to burial by basin-fill sediments and subsequent eruptive products. However, previous estimates of a total volume of 100 km^3 are likely too high by a factor of ~5.

Monogenetic volcanic fields are areas of active investigation around the world. Linking physical volcanological, structural, geochemical, and petrologic data are key in advancing our understanding of these systems. High-resolution geophysical studies that identify crustal structures and potential kilometer-scale domains of elevated melt, the inferred sources of individual volcanoes and clusters, could provide important tests of the conceptual model we have suggested for relating surface expressions of volcanism with deep magma sources, as will numerical modeling. Such work is needed to improve our understanding of the full spectrum of volcanism on Earth and, by analogy, the other terrestrial planets.

ACKNOWLEDGMENTS

This work was supported by U.S. National Science Foundation collaborative grants EAR-1016100 (Valentine), 1016042 (Widom), and 1016104 (Smith). We thank Duane Champion for making us aware of certain age dates provided by Brent Turrin, and Brandon Schmandt for providing the tomographic image. Dave Kuentz provided valuable support in sampling and geochemical analyses. We also thank the following students who assisted in the field: Nicole Shufelt, Peter Johnson, Amanda Hintz, Jamal Amin, Alessandro Tadini, Matthew Sweeney, Dayana Schonwalder, Marissa Mnich, Christine Sumner, Patrick Whelley, Mai Sas, Amber Ciravolo, and Hugo Belmontes. We thank Jan Lindsay, Marco Brenna, and Nicolas Le Corvec for their helpful reviews of the manuscript.

REFERENCES CITED

Amin, J., 2013, Lateral Variations in Strata Competence and Alternating Eruption Styles in Time and Space as Morphological Controls on a Maar Crater in the Lunar Crater Volcanic Field, Nevada, USA [M.S. thesis]: Buffalo, State University of New York University at Buffalo, 102 p.

Aranda-Gómez, J.J., Luhr, J.F., Housh, T.B., Connor, C.B., Becker, T., and Henry, C.D., 2003, Syn-extensional Pliocene–Pleistocene eruptive activity in the Camargo volcanic field, Chihuahua, México: Geological Society of America Bulletin, v. 115, p. 298–313, doi:10.1130/0016-7606(2003)115<0298:SPPEAI>2.0.CO;2.

Aranda-Gómez, J.J., Housh, T.B., Luhr, J.F., Noyola-Medrano, C., and Rojas-Beltrán, M.A., 2010, Origin and formation of neck in a basin landform: Examples from the Camargo volcanic field, Chihuahua (México): Journal of Volcanology and Geothermal Research, v. 197, p. 123–132, doi:10.1016/j.jvolgeores.2009.08.004.

Bacon, C.R., 1982, Time-predictable bimodal volcanism in the Coso Range, California: Geology, v. 10, p. 65–69, doi:10.1130/0091-7613(1982)10<65:TBVITC>2.0.CO;2.

Ballmer, M.D., Conrad, C.P., Smith, E.I., and Johnsen, R., 2015, Intraplate volcanism at the edges of the Colorado Plateau sustained by a combination of triggered edge-driven convection and shear-driven upwelling: Geochemistry, Geophysics, Geosystems, v. 16, p. 366–379, doi:10.1002/2014GC005641.

Bergman, S.C., 1982, Petrogenetic Aspects of the alkali basaltic Lavas and Included Megacrysts and Nodules from the Lunar Crater Volcanic Field, Nevada, U.S.A. [Ph.D. thesis]: Princeton, New Jersey, Princeton University, 432 p.

Bergman, S.C., Foland, K., and Spera, F., 1981, On the origin of an amphibole-rich vein in a peridotites inclusion from the Lunar Crater Volcanic Field, Nevada, U.S.A.: Earth and Planetary Science Letters, v. 56, p. 343–361, doi:10.1016/0012-821X(81)90139-4.

Best, M.G., Gromme, S., Deino, A.L., Christianson, E.H., Hart, G.L., and Tingey, D.G., 2013, The 36–18 Ma central Nevada ignimbrite field and calderas, Great Basin, USA: Multicyclic supereruptions: Geosphere, v. 9, p. 1562–1636, doi:10.1130/GES00945.1.

Best, M.G., Christiansen, E.H., de Silva, S., and Lipman, P.S., 2016, Slab-rollback ignimbrite flareups in the southern Great Basin and other Cenozoic American arcs: A distinct style of arc volcanism: Geosphere, v. 12, p. 1097–1135, doi:10.1130/GES01285.1.

Blondes, M.S., Reiners, P.W., Ducca, M.N., Singer, B.D., and Chesley, J., 2008, Temporal-compositional trends over short and long time-scales in basalts of the Big Pine Volcanic Field, California: Earth and Planetary Science Letters, v. 269, p. 140–154, doi:10.1016/j.epsl.2008.02.012.

Bolós, X., Barde-Cabusson, S., Pedrazzi, D., Martí, J., Casas, A., Himi, M., and Lovera, R., 2012, Investigation of the inner structure of La Crosa de Sant Dalmai maar (Catalan Volcanic Zone, Spain): Journal of Volcanology and Geothermal Research, v. 247–248, p. 37–48, doi:10.1016/j.jvolgeores.2012.08.003.

Brown, R.J., and Valentine, G.A., 2013, Physical characteristics of kimberlite and basaltic intraplate volcanism, and implications of a biased kimberlite record: Geological Society of America Bulletin, v. 125, p. 1224–1238, doi:10.1130/B30749.1.

Carey, S., and Sparks, R.S.J., 1986, Quantitative models of the fallout and dispersal of tephra from volcanic eruption columns: Bulletin of Volcanology, v. 48, p. 109–125, doi:10.1007/BF01046546.

Cebriá, J.M., Martín-Escorza, C., Lópes-Ruiz, J., Morán-Zenteno, D.J., and Martiny, B.M., 2011, Numerical recognition of alignments in monogenetic volcanic areas: Examples from the Michoacán-Guanajuato Volcanic Field in Mexico and Calatrava in Spain: Journal of Volcanology and Geothermal Research, v. 201, p. 73–82, doi:10.1016/j.jvolgeores.2010.07.016.

Cimarelli, C., Di Traglia, F., de Rita, D., Gimeno Torrente, D., and Fernandez Turiel, J.-L., 2013, Space-time evolution of monogenetic volcanism in the mafic Garrotxa Volcanic Field (NE Iberian Peninsula): Bulletin of Volcanology, v. 75, p. 758, doi:10.1007/s00445-013-0758-6.

Conway, F.M., Ferrill, D.A., Hall, C.M., Morris, A.P., Stamatakos, J.A., Connor, C.B., Halliday, A.N., and Condit, C., 1997, Timing of basaltic volcanism along the Mesa Butte fault in the San Francisco Volcanic Field, Arizona, from $^{40}Ar/^{39}Ar$ dates: Implications for longevity of cinder cone alignments: Journal of Geophysical Research, v. 102, p. 815–824, doi:10.1029/96JB02853.

Cortés, J.A., Smith, E.I., Valentine, G.A., Johnsen, R., Rasoazanamparany, C., Widom, E., Sas, M., and Ruth, D., 2015, Intrinsic conditions of magmas from the Lunar Crater Volcanic Field (Nevada): Implications for internal plumbing and magma ascent: American Mineralogist, v. 100, p. 396–413, doi:10.2138/am-2015-4812.

Cousens, B., Wetmore, S., and Henry, C.D., 2013, The Pliocene–Quaternary Buffalo Valley volcanic field, Nevada: Post-extension, intraplate magmatism in the north-central Great Basin, USA: Journal of Volcanology and Geothermal Research, v. 268, p. 17–35, doi:10.1016/j.jvolgeores.2013.10.006.

Crisp, J.A., 1984, Rates of magma emplacement and volcanic output: Journal of Volcanology and Geothermal Research, v. 20, p. 177–211, doi:10.1016/0377-0273(84)90039-8.
Daniels, K.A., Kavanaugh, J.L., Menand, T., and Sparks, R.S.J., 2012, The shapes of dikes: Evidence for the influence of cooling and inelastic deformation: Geological Society of America Bulletin, v. 124, p. 1102–1112, doi:10.1130/B30537.1.
Delaney, P.T., and Gartner, A.E., 1997, Physical processes of shallow mafic dike emplacement near the San Rafael Swell, Utah: Geological Society of America Bulletin, v. 109, p. 1177–1192, doi:10.1130/0016-7606(1997)109<1177:PPOSMD>2.3.CO;2.
Delaney, P.T., Pollard, D.D., Ziony, J.I., and McKee, E.H., 1986, Field relations between dikes and joints: Emplacement processes and paleostress analysis: Journal of Geophysical Research, v. 91, p. 4920–4938, doi:10.1029/JB091iB05p04920.
Delcamp, A., van Wyk de Vries, B., Stéphane, P., and Kervyn, M., 2014, Endogenous and exogenous growth of the monogenetic Lemtégy volcano, Chaîne des Puys, France: Geosphere, v. 10, p. 998–1019, doi:10.1130/GES01007.1.
Dickson, L.D., 1997, Volcanology and geochemistry of Pliocene and Quaternary basalts on Citadel Mountain, Lunar Crater Volcanic Field, Pancake Range, Nevada [M.S. thesis]: Las Vegas, University of Nevada, 146 p.
Dohrenwend, J.C., Abrahams, A.D., and Turrin, B.D., 1987, Drainage development on basaltic lava flows, Cima volcanic field, southeast California, and Lunar Crater volcanic field, south-central Nevada: Geological Society of America Bulletin, v. 99, p. 405–413, doi:10.1130/0016-7606(1987)99<405:DDOBLF>2.0.CO;2.
Ekren, E.B., Hinrichs, E.N., and Dixon, G.L., 1972, Geologic map of The Wall quadrangle, Nye County, Nevada: U.S. Geological Survey Miscellaneous Investigations Map I-719, scale 1:48,000.
Ekren, E.B., Quinlivan, W.D., Snyder, R.P., and Kleinhampl, F.J., 1974, Stratigraphy, structure, and geologic history of the Lunar Lake caldera of northern Nye County, Nevada: U.S. Geological Survey Journal of Research, v. 2, p. 599–608.
Emery, C., 2012, Volcanic Evolution of the Southern Quinn Canyon Range: Implications for Regional Correlation of Volcanic Units [M.S. thesis]: Las Vegas, University of Nevada, 90 p.
Erlund, E.J., Cashman, K.V., Wallace, P.J., Pioli, L., Rosi, M., Johnson, E., and Delgado Grenados, H., 2010, Compositional evolution of magma from Parícutin Volcano, Mexico: The tephra record: Journal of Volcanology and Geothermal Research, v. 197, p. 167–187, doi:10.1016/j.jvolgeores.2009.09.015.
Farmer, G.L., Perry, F.V., Semken, S., Crowe, B., Curtis, D., and DePaolo, D.J., 1989, Isotopic evidence on the structure and origin of subcontinental lithospheric mantle in southern Nevada: Journal of Geophysical Research, v. 94, p. 7885–7898, doi:10.1029/JB094iB06p07885.
Fisher, R.V., and Schmincke, H.-U., 1984, Pyroclastic Rocks: Berlin, Springer-Verlag, 472 p., doi:10.1007/978-3-642-74864-6.
Foland, K.A., and Bergman, S.C., 1992, Temporal and spatial distribution of basaltic volcanism in the Pancake and Reveille Ranges north of Yucca Mountain, *in* Proceedings of the International Nuclear Waste Symposium, Volume 2: La Grange Park, Illinois, American Nuclear Society, p. 2366–2371.
Friese, N., Bense, F.A., Tanner, D.C., Gústafsson, L.E., and Siegesmund, S., 2013, From feeder dykes to scoria cones: The tectonically controlled plumbing system of the Rauohólar volcanic chain, Northern Volcanic Zone, Iceland: Bulletin of Volcanology, v. 75, 717, doi:10.1007/s00445-013-0717-2.
Gaffney, E.S., Damjanac, B., and Valentine, G.A., 2007, Localization of volcanic activity: 2. Effects of pre-existing structure: Earth and Planetary Science Letters, v. 263, p. 323–338, doi:10.1016/j.epsl.2007.09.002.
Gazel, E., Plank, T., Forsyth, D.W., Bendersky, C., Lee, C.-T.A., and Hauri, E.H., 2012, Lithospheric versus asthenospheric mantle sources at the Big Pine Volcanic Field, California: Geochemistry, Geophysics, Geosystems, v. 13, Q0AK06, doi:10.1029/2012GC004060.
Genareau, K., Valentine, G.A., Moore, G., and Hervig, R.L., 2010, Mechanisms for transition in eruptive style at a monogenetic scoria cone revealed by microtextural analysis (Lathrop Wells volcano, Nevada, U.S.A.): Bulletin of Volcanology, v. 72, p. 593–607, doi:10.1007/s00445-010-0345-z.
Germa, A., Connor, L.J., Cañon-Tapia, E., and Le Corvec, N., 2013, Tectonic and magmatic controls on the location of post-subduction monogenetic volcanoes in Baja California, Mexico, revealed through spatial analysis of eruptive vents: Bulletin of Volcanology, v. 75, 782, doi:10.1007/s00445-013-0782-6.
Geshi, N., and Neri, M., 2014, Dynamic feeder dyke systems in basaltic volcanoes: The exceptional example of the 1809 Etna eruption (Italy): Frontiers of Earth Science, v. 2, 13, doi:10.3389/feart.2014.00013.
Geshi, N., Kusumoto, S., and Gudmundsson, A., 2010, Geometric difference between non-feeder and feeder dikes: Geology, v. 38, p. 195–198, doi:10.1130/G30350.1.
Graettinger, A.H., Valentine, G.A., Sonder, I., Ross, P.-S., White, J.D.L., and Taddeucci, J., 2014, Maar-diatreme geometry and deposits: Subsurface blast experiments with variable explosion depth: Geochemistry, Geophysics, Geosystems, v. 15, p. 740–764, doi:10.1002/2013GC005198.
Graettinger, A.H., Valentine, G.A., Sonder, I., Ross, P.-S., and White, J.D.L., 2015a, Facies distribution of ejecta in analog tephra rings from experiments with single and multiple subsurface explosions: Bulletin of Volcanology, v. 77, 66, doi:10.1007/s00445-015-0951-x.
Graettinger, A.H., Valentine, G.A., and Sonder, I., 2015b, Circum-crater variability of deposits from discrete, laterally and vertically migrating volcanic explosions: Experimental evidence and field implications: Journal of Volcanology and Geothermal Research, v. 308, p. 61–69, doi:10.1016/j.jvolgeores.2015.10.019.
Gutmann, J.T., 2002, Strombolian and effusive activity as precursors to phreatomagmatism: Eruptive sequence at maars of the Pinacate volcanic field, Sonora, Mexico: Journal of Volcanology and Geothermal Research, v. 113, p. 345–356, doi:10.1016/S0377-0273(01)00265-7.
Harp, A.G., and Valentine, G.A., 2015, Shallow plumbing and eruptive processes of a scoria cone built on steep terrain: Journal of Volcanology and Geothermal Research, v. 294, p. 37–55, doi:10.1016/j.jvolgeores.2015.02.008.
Harris, A.J.L., and Rowland, S.K., 2015, Lava flows and rheology, *in* Sigurdsson, H., et al., eds., The Encyclopedia of Volcanoes (second edition): London, Elsevier, p. 321–342, doi:10.1016/B978-0-12-385938-9.00017-1.
Hart, S.R., 1984, A large-scale isotope anomaly in the Southern Hemisphere mantle: Nature, v. 309, p. 753–757, doi:10.1038/309753a0.
Heidbach, O., Tingay, M., Barth, A., Reinecker, J., Kurfeß, D., and Müller, B., 2008, The World Stress Map Database Release 2008: WSM release, doi:10.1594/GFZ.
Heiken, G., 1978, Characteristics of tephra from Cinder Cone, Lassen Volcanic National Park, California: Bulletin Volcanologique, v. 41, p. 119–130, doi:10.1007/BF02597025.
Heizler, M., 2013, $^{40}Ar/^{39}Ar$ geochronology results for Lunar Crater Volcanic Field basalts: New Mexico Geochronological Research Laboratory report NMGRL-IR-792, https://vhub.org/resources/2503 (last accessed June 2016).
Heizler, M., 2014, $^{40}Ar/^{39}Ar$ geochronology results for Lunar Crater Volcanic Field basalts: New Mexico Geochronological Research Laboratory report NMGRL-IR-844, https://vhub.org/resources/2503 (June 2016).
Hintz, A.R., and Valentine, G.A., 2012, Complex plumbing of monogenetic scoria cones: New insights from the Lunar Crater Volcanic Field (Nevada, USA): Journal of Volcanology and Geothermal Research, v. 239–240, p. 19–32, doi:10.1016/j.jvolgeores.2012.06.008.
Holm, R.F., 1987, Significance of agglutinate mounds on lava flows associated with monogenetic cones: An example at Sunset Crater, northern Arizona: Geological Society of America Bulletin, v. 99, p. 319–324, doi:10.1130/0016-7606(1987)99<319:SOAMOL>2.0.CO;2.
Houghton, B.F., and Schmincke, H.-U., 1986, Mixed deposits of simultaneous strombolian and phreatomagmatic volcanism: Rothenberg volcano, east Eifel volcanic field: Journal of Volcanology and Geothermal Research, v. 30, p. 117–130, doi:10.1016/0377-0273(86)90069-7.
Houghton, B.F., Wilson, C.J.N., and Smith, I.E.M., 1999, Shallow-seated controls on styles of explosive basaltic volcanism: A case study from New Zealand: Journal of Volcanology and Geothermal Research, v. 91, p. 97–120, doi:10.1016/S0377-0273(99)00058-X.
Houghton, B.F., Bonadonna, C., Gregg, C.E., Johnston, D.M., Cousins, W.J., Cole, J.W., and Del Carlo, P., 2006, Proximal tephra hazards: recent eruption studies applied to volcanic risk in the Auckland volcanic field, New Zealand: Journal of Volcanology and Geothermal Research, v. 155, p. 138–149, doi:10.1016/j.jvolgeores.2006.02.006.
Jiménez-Moreno, G., Anderson, R.S., and Fawcett, P.J., 2007, Orbital- and millennial-scale vegetation and climate changes of the past 225 ka from Bear Lake, Utah-Idaho (USA): Quaternary Science Reviews, v. 26, p. 1713–1724, doi:10.1016/j.quascirev.2007.05.001.
Johnson, P.J., Valentine, G.A., Cortés, J.A., and Tadini, A., 2014, Basaltic tephra from monogenetic Marcath Volcano, central Nevada: Journal of Volcanology and Geothermal Research, v. 281, p. 27–33, doi:10.1016/j.jvolgeores.2014.05.007.
Jordan, S.C., Cas, R.A.F., and Hayman, P.C., 2013, The origin of a large (>3 km) maar volcano by coalescence of multiple shallow craters: Lake Purrumbete maar, southeastern Australia:

Journal of Volcanology and Geothermal Research, v. 254, p. 5–22, doi:10.1016/j.jvolgeores.2012.12.019.

Kargel, J.S., 1987, The Geochemistry of Basalts and Mantle Inclusions from the Lunar Crater Volcanic Field, Nevada; Petrogenetic and Geodynamic Implications [M.S. thesis]: Columbus, Ohio State University, 393 p.

Keating, G.N., Valentine, G.A., Krier, D.J., and Perry, F.V., 2008, Shallow plumbing systems for small-volume basaltic volcanoes: Bulletin of Volcanology, v. 70, p. 563–582, doi:10.1007/s00445-007-0154-1.

Kempton, P.D., Harmon, R.S., Hawkesworth, C.J., and Moorbath, S., 1990, Petrology and geochemistry of lower crustal granulites from the Geronimo Volcanic Field, southeastern Arizona: Geochimica Cosmochimica Acta, v. 54, p. 3401–3426, doi:10.1016/0016-7037(90)90294-U.

Kuntz, M.A., Champion, D.E., Spiker, E.C., and Lefebvre, R.H., 1986, Contrasting magma types and steady-state, volume-predictable basaltic volcanism along the Great Rift, Idaho: Geological Society of America Bulletin, v. 97, p. 579–594, doi:10.1130/0016-7606(1986)97<579:CMTASV>2.0.CO;2.

Le Corvec, N., Spörli, K.B., Rowland, J., and Lindsay, J., 2013a, Spatial distribution and alignments of volcanic centers: clues to the formation of monogenetic volcanic fields: Earth-Science Reviews, v. 124, p. 96–114, doi:10.1016/j.earscirev.2013.05.005.

Le Corvec, N., Menand, T., and Lindsay, J., 2013b, Interaction of ascending magma with pre-existing crustal fractures in monogenetic basaltic volcanism: An experimental approach: Journal of Geophysical Research, v. 118, p. 1–17, doi:10.1002/jgrb.50142.

Le Corvec, N., Bebbington, M.S., Lindsay, J.M., and McGee, L.E., 2013c, Age, distance, and geochemical evolution within a monogenetic volcanic field: Analyzing patterns in the Auckland Volcanic Field eruption sequence: Geochemistry, Geophysics, Geosystems, v. 14, p. 3648–3665, doi:10.1002/ggge.20223.

Le Maitre, R.W., ed., 2002, Igneous Rocks: A Classification and Glossary of Terms. Recommendations of the International Union of Geological Sciences (subcommission of the systematics of igneous rocks): Cambridge, UK, Cambridge University Press, 256 p., doi:10.1017/CBO9780511535581.

LeFebvre, N.S., White, J.D.L., and Kjarsgaard, B.A., 2013, Unbedded diatreme deposits reveal maar-diatreme-forming eruptive processes: Standing Rocks West, Hopi Buttes, Navajo Nation, USA: Bulletin of Volcanology, v. 75, 739, doi:10.1007/s00445-013-0739-9.

Levander, A., and Miller, M.S., 2012, Evolutionary aspects of lithospheric discontinuity structure in the western U.S.: Geochemistry, Geophysics, Geosystems, v. 13, Q0AK07, doi:10.1029/2012GC004056.

Li, X., Yuan, X., and Kind, R., 2007, The lithosphere-asthenosphere boundary beneath the western United States: Geophysical Journal International, v. 170, p. 700–710, doi:10.1111/j.1365-246X.2007.03428.x.

Lockwood, J.P., and Hazlett, R.W., 2010, Volcanoes: Global Perspectives: Chichester, John Wiley & Sons, Ltd., 539 p.

Lorenz, V., 1986, On the growth of maars and diatremes and its relevance to the formation of tuff rings: Bulletin of Volcanology, v. 48, p. 265–274, doi:10.1007/BF01081755.

Luhr, J.F., and Simkin, T., eds., 1993, Parícutin, the Volcano Born in a Mexican Cornfield: Phoenix, Arizona, Geoscience Press, Inc., 427 p.

Luhr, J.F., Aranda-Gómez, J.J., and Housh, T.B., 1995, San Quintín volcanic field, Baja California Norte, México: Geology, petrology and geochemistry: Journal of Geophysical Research, v. 100, p. 10,353–10,380, doi:10.1029/95JB00037.

Lum, C.C.L., Leeman, W.P., Foland, K.A., Kargel, J.A., and Fitton, J.G., 1989, Isotopic variations in continental basaltic lavas as indicators of mantle heterogeneity: Examples from the western U.S. Cordillera: Journal of Geophysical Research, v. 94, p. 7871–7884, doi:10.1029/JB094iB06p07871.

Martí, J., Planagumà, L., Geyer, A., Canal, E., and Pedrazzi, D., 2011, Complex interaction between Strombolian and phreatomagmatic eruptions in the Quaternary monogenetic volcanism of the Catalan Volcanic Zone (NE of Spain): Journal of Volcanology and Geothermal Research, v. 201, p. 178–193, doi:10.1016/j.jvolgeores.2010.12.009.

Martin, M.W., and Naumann, T.R., 1995, Geologic Map of the Reveille Quadrangle, Nevada: Nevada Bureau of Mines and Geology Map 104, scale 1:24,000.

Mathieu, L., van Wyk de Vries, B., Holohan, E.P., and Troll, V.R., 2008, Dykes, cups, saucers and sills: Analog experiments on magma intrusion into brittle rocks: Earth and Planetary Science Letters, v. 271, p. 1–13, doi:10.1016/j.epsl.2008.02.020.

McFadden, L.D., Wells, S.G., and Jercinovich, M.J., 1987, Influences of eolian and pedogenic processes on the origin and evolution of desert pavements: Geology, v. 15, p. 504–508, doi:10.1130/0091-7613(1987)15<504:IOEAPP>2.0.CO;2.

McGee, L.E., and Smith, I.E.M., 2016, Interpreting chemical compositions of small scale basaltic systems: A review: Journal of Volcanology and Geothermal Research, v. 325, p. 45–60, doi:10.1016/j.jvolgeores.2016.06.007.

Menand, T., and Phillips, J.C., 2006, Gas segregation in dykes and sills: Journal of Volcanology and Geothermal Research, v. 159, p. 393–408, doi:10.1016/j.jvolgeores.2006.08.003.

Menzies, M.A., 1989, Cratonic, circumcratonic and oceanic mantle domains beneath the western United States: Journal of Geophysical Research, v. 94, p. 7899–7915, doi:10.1029/JB094iB06p07899.

Muirhead, J.D., Van Eaton, A.R., Re, G., and White, J.D.L., 2016, Monogenetic volcanoes fed by interconnected dikes and sills in the Hopi Buttes volcanic field, Navajo Nation, USA: Bulletin of Volcanology, v. 78, 11, doi:10.1007/s00445-016-1005-8.

Murcia, H., Lindsay, J.M., Németh, K., Smith, I.E.M., Cronin, S.J., Moufti, M.R.H., El-Masry, N.N., and Niedermann, S., 2016, Geology and geochemistry of late Quaternary volcanism in northern Harrat Rahat, Kingdom of Saudi Arabia: Implications for eruption dynamics, regional stratigraphy, and magma evolution, *in* Németh, K., et al., eds., Monogenetic Volcanism: Geological Society of London Special Publication 446, doi:10.1144/SP446.2.

Nakamura, K., 1977, Volcanoes as possible indicators of tectonic stress orientation—Principle and proposal: Journal of Volcanology and Geothermal Research, v. 2, p. 1–16, doi:10.1016/0377-0273(77)90012-9.

Naumann, T.R., Smith, E.I., Shafiqullah, M., and Damon, P.E., 1991, New K-Ar ages for Pliocene mafic to intermediate volcanic rocks in the Reveille Range, Nevada: Isochron-West, no. 57, p. 12–16.

Németh, K., 2010, Monogenetic volcanic fields: Origin, sedimentary record, and relationship with polygenetic volcanism, *in* Cañón-Tapia, E., and Szakács, A., eds., What Is a Volcano?: Geological Society of America Special Paper 470, p. 43–66, doi:10.1130/2010.2470(04).

Németh, K., and Martin, U., 2007, Shallow sill and dyke complex in western Hungary as a possible feeding system of phreatomagmatic volcanoes in "soft-rock" environment: Journal of Volcanology and Geothermal Research, v. 159, p. 138–152, doi:10.1016/j.jvolgeores.2006.06.014.

Németh, K., Cronin, S.J., Smith, I.E.M., and Agustin Flores, J., 2012, Amplified hazard of small-volume monogenetic eruptions due to environmental controls, Orakei Basin, Auckland Volcanic Field, New Zealand: Bulletin of Volcanology, v. 74, p. 2121–2137, doi:10.1007/s00445-012-0653-6.

Ort, M.H., and Carrasco-Nuñez, G., 2009, Lateral vent migration during phreatomagmatic and magmatic eruptions at Tecuitlapa Maar, east-central Mexico: Journal of Volcanology and Geothermal Research, v. 181, p. 67–77, doi:10.1016/j.jvolgeores.2009.01.003.

Ort, M.H., Elson, M.D., Anderson, K.C., Duffield, W.A., Hooten, J.A., Champion, D.E., and Waring, G., 2008, Effects of scoria-cone eruptions upon nearby human communities: Geological Society of America Bulletin, v. 120, p. 476–486, doi:10.1130/B26061.1.

Parcheta, C., Houghton, B.F., and Swanson, D.A., 2012, Hawaiian fissure fountains 1: Decoding deposits—Episode 1 of the 1969–1974 Mauna Ulu eruption: Bulletin of Volcanology, v. 74, p. 1729–1743, doi:10.1007/s00445-012-0621-1.

Parcheta, C., Fagents, S., Swanson, D.A., Houghton, B.F., and Ericksen, T., 2015, Hawaiian fissure fountains: quantifying vent and shallow conduit geometry, Episode 1 of the 1969–1974 Mauna Ulu eruption, *in* Carey, R., et al., eds., Hawaiian Volcanoes: From Source to Surface: American Geophysical Union Geophysical Monograph 208, p. 369–391, doi:10.1002/9781118872079.ch17.

Parfitt, E.A., and Wilson, L., 1999, A Plinian treatment of fallout from Hawaiian lava fountains: Journal of Volcanology and Geothermal Research, v. 88, p. 67–75, doi:10.1016/S0377-0273(98)00103-6.

Parsons, T., 1995, The Basin and Range Province, *in* Olsen, K., ed., Continental rifts: Evolution, Structure and Tectonics: Amsterdam, Elsevier, p. 277–324.

Pedrazzi, D., Bolós, X., Barde-Cabusson, S., and Martí, J., 2016, Reconstructing the eruptive history of a monogenetic volcano through a combination of fieldwork and geophysical surveys: The example of Puig d'Àdri (Garrotxa Volcanic Field): Journal of the Geological Society [London], v. 173, p. 875–888, doi:10.1144/jgs2016-009.

Poland, M.P., Moats, W.P., and Fink, J.H., 2008, A model for radial dike emplacement in composite cones based on observations from Summer Coon volcano, Colorado, USA: Bulletin of Volcanology, v. 70, p. 861–875, doi:10.1007/s00445-007-0175-9.

Pollard, D.D., 1987, Elementary fracture mechanics applied to the structural interpretation of dykes, *in* Halls, H.C., and Fahrig, W.H., eds., Mafic Dike Swarms: Geological Association of Canada Special Paper 34, p. 5–24.

Rasoazanamparany, C., Widom, E., Valentine, G.A., Smith, E.I., Cortés, J.A., Kuentz, D., and Johnsen, R., 2015, Origin of chemical and isotopic heterogeneity in a mafic, monogenetic volcanic field: A case study of the Lunar Crater volcanic field, Nevada: Chemical Geology, v. 397, p. 76–93, doi:10.1016/j.chemgeo.2015.01.004.

Re, G., White, J.D.L., and Ort, M.H., 2015, Dikes, sills, and stress-regime evolution during emplacement of the Jagged Rocks complex, Hopi Buttes Volcanic field, Navajo Nation, USA: Journal of Volcanology and Geothermal Research, v. 295, p. 65–79, doi:10.1016/j.jvolgeores.2015.01.009.

Re, G., White, J.D.L., Muirhead, J.D., and Ort, M.H., 2016, Subterranean fragmentation of magma during conduit initiation and evolution in the shallow plumbing system of the small-volume Jagged Rocks volcanoes (Hopi Buttes Volcanic Field, Arizona, USA): Bulletin of Volcanology, v. 78, 55, doi:10.1007/s00445-016-1050-3.

Reynolds, P., Brown, R.J., Thordarson, T., and Llewellin, E.W., 2016, The architecture and shallow conduits of Laki-type pyroclastic cones: Insights into a basaltic fissure eruption: Bulletin of Volcanology, v. 78, 36, doi:10.1007/s00445-016-1029-0.

Richardson, J.A., Connor, C.B., Wetmore, P.H., Connor, L.J., and Gallant, E.A., 2015, Role of sills in the development of volcanic fields: Insights from lidar mapping surveys of the San Rafael Swell, Utah: Geology, v. 43, p. 1023–1026, doi:10.1130/G37094.1.

Richter, D.H., Eaton, J.P., Murata, K.J., Ault, W.U., and Krivoy, H.L., 1970, Chronological narrative of the 1959–60 eruption of Kilauea Volcano, Hawaii: U.S. Geological Survey Professional Paper 537-E, 73 p.

Riggs, N.R., and Duffield, W.A., 2008, Record of complex scoria cone activity at Red Mountain, Arizona, USA, and implications for monogenetic mafic volcanoes: Journal of Volcanology and Geothermal Research, v. 178, p. 763–776, doi:10.1016/j.jvolgeores.2008.09.004.

Rubin, A.M., 1995, Propagation of magma-filled cracks: Annual Review of Earth and Planetary Sciences, v. 23, p. 287–336, doi:10.1146/annurev.ea.23.050195.001443.

Sass, J.H., Lachenbruch, A.H., Galanis, S.P., Jr., Morgan, P., Priest, S.S., Moses, T.H., Jr., and Munroe, R.J., 1994, Thermal regime of the southern Basin and Range Province: 1. Heat flow data from Arizona and the Mojave Desert of California and Nevada: Journal of Geophysical Research, v. 99, p. 22,093–22,119, doi:10.1029/94JB01891.

Schmandt, B., and Lin, F.C., 2014, P and S wave tomography of the mantle beneath the United States: Geophysical Research Letters, v. 41, p. 6342–6349, doi:10.1002/2014GL061231.

Schulte-Pelkum, V., Biasi, G., Sheehan, A., and Jones, C., 2011, Differential motion between upper crust and lithospheric mantle in the central Basin and Range: Nature Geoscience, v. 4, p. 619–623, doi:10.1038/ngeo1229.

Scott, D.H., and Trask, N.J., 1969, Geology of the Lunar Crater Volcanic Field, Nye County, Nevada: U.S. Geological Survey Professional Paper 599-I, 122 p.

Self, S., Keszthelyi, L., and Thordarson, T., 1998, The importance of pāhoehoe: Annual Review of Earth and Planetary Sciences, v. 26, p. 81–110, doi:10.1146/annurev.earth.26.1.81.

Shepard, M.K., Arvidson, R.E., Caffee, M., Finkel, R., and Harris, L., 1995, Cosmogenic exposure ages of basalt flows: Lunar Crater volcanic field, Nevada: Geology, v. 23, p. 21–24, doi:10.1130/0091-7613(1995)023<0021:CEAOBF>2.3.CO;2.

Smith, R.L., and Luedke, R.G., 1984, Potentially active volcanic lineaments and loci in western conterminous United States, *in* Geophysics Study Committee, eds., Explosive Volcanism: Inception, Evolution, and Hazards: Studies in Geophysics: Washington, D.C., National Academy Press, p. 47–66.

Smith, E.I., Sánchez, A., Walker, D.J., and Wang, K., 1999, Geochemistry of mafic magmas in the Hurricane Volcanic field, Utah: Implications for small- and large-scale chemical variability of the lithospheric mantle: Journal of Geology, v. 107, p. 433–448, doi:10.1086/314355.

Snyder, R.P., Ekren, E.B., and Dixon, G.L., 1972, Geologic Map of the Lunar Crater Quadrangle, Nye County, Nevada: U.S. Geological Survey Miscellaneous Investigations Map I-700, scale 1:48,000.

Spera, F.J., and Fowler, S.J., 2009, Conceptual model for small-volume alkali basalt petrogenesis: Implications for volcanic hazards at the proposed Yucca Mountain Nuclear Waste Repository, *in* Connor, C.B., et al., eds., Volcanic and Tectonic Hazard Assessment for Nuclear Facilities: Cambridge, Cambridge University Press, p. 195–228, doi:10.1017/CBO9780511635380.009.

Stickney, E.K., 2004, The Volcanology and Petrogenesis of the Northern Lunar Crater Volcanic Field, Nye County, Nevada [M.S. thesis]: Las Vegas, University of Nevada, 93 p.

Sumner, J.M., 1998, Formation of clastogenic lava flows during fissure eruption and scoria cone collapse: The 1986 eruption of Izu-Oshima Volcano, eastern Japan: Bulletin of Volcanology, v. 60, p. 195–212, doi:10.1007/s004450050227.

Sun, S.S., and McDonough, W.F., 1989, Chemical and isotopic systematics of oceanic basalts: Implications for mantle composition and processes, *in* Saunders, A.D., and Norry, M.J., eds., Magmatism in the Ocean Basins: Geological Society of London Special Publication 42, p. 313-345, doi:10.1144/GSL.SP.1989.042.01.19.

Swanson, D.A., 1966, Tieton Volcano, a Miocene eruptive center in the southern Cascade Mountains, Washington: Geological Society of America Bulletin, v. 77, p. 1293–1314, doi:10.1130/0016-7606(1966)77[1293:TVAMEC]2.0.CO;2.

Sweeney, M.R., and Valentine, G.A., 2015, Transport and mixing dynamics from explosions in debris-filled volcanic conduits: Numerical results and implications for maar-diatreme volcanoes: Earth and Planetary Science Letters, v. 425, p. 64–76, doi:10.1016/j.epsl.2015.05.038.

Taddeucci, J., Valentine, G.A., Sonder, I., White, J.D.L., Ross, P.-S., and Scarlato, P., 2013, The effect of pre-existing craters on the initial development of explosive volcanic eruptions: An experimental investigation: Geophysical Research Letters, v. 40, p. 507–510, doi:10.1002/grl.50176.

Tadini, A., Bonali, F.L., Corazzato, C., Cortés, J.A., Tibaldi, A., and Valentine, G.A., 2014, Spatial distribution and structural analysis of vents in the Lunar Crater Volcanic Field (Nevada, USA): Bulletin of Volcanology, v. 76, 877, doi:10.1007/s00445-014-0877-8.

Thompson, G.A., and Burke, D.B., 1974, Regional geophysics of the Basin and Range Province: Annual Review of Earth and Planetary Sciences, v. 2, p. 213–238, doi:10.1146/annurev.ea.02.050174.001241.

Valentine, G.A., 2012, Shallow plumbing systems for small-volume basaltic volcanoes, 2: Evidence from crustal xenoliths at scoria cones and maars: Journal of Volcanology and Geothermal Research, v. 223–224, p. 47–63, doi:10.1016/j.jvolgeores.2012.01.012.

Valentine, G.A., and Connor, C.B., 2015, Basaltic volcanic fields, *in* Sigurdsson, H., et al., eds., The Encyclopedia of Volcanoes (second edition): London, Elsevier, p. 423–439, doi:10.1016/B978-0-12-385938-9.00023-7

Valentine, G.A., and Cortés, J.A., 2013, Time and space variations in magmatic and phreatomagmatic eruptive processes at Easy Chair (Lunar Crater Volcanic Field, Nevada, USA): Bulletin of Volcanology, v. 75, 752, doi:10.1007/s00445-013-0752-z.

Valentine, G.A., and Gregg, T.K.P., 2008, Continental basaltic volcanoes—Processes and problems: Journal of Volcanology and Geothermal Research, v. 177, p. 857–873, doi:10.1016/j.jvolgeores.2008.01.050.

Valentine, G.A., and Harrington, C.D., 2006, Clast size controls and longevity of Pleistocene desert pavements at Lathrop Wells and Red Cone volcanoes, southern Nevada: Geology, v. 34, p. 533–536, doi:10.1130/G22481.1.

Valentine, G.A., and Keating, G.N., 2007, Eruptive styles and inferences about plumbing systems at Hidden Cone and Little Black Peak scoria cone volcanoes (Nevada, U.S.A.): Bulletin of Volcanology, v. 70, p. 105–113, doi:10.1007/s00445-007-0123-8.

Valentine, G.A., and Krogh, K.E.C., 2006, Emplacement of shallow dikes and sills beneath a small basaltic volcanic center—The role of pre-existing structure (Paiute Ridge, southern Nevada, USA): Earth and Planetary Science Letters, v. 246, p. 217–230, doi:10.1016/j.epsl.2006.04.031.

Valentine, G.A., and Perry, F.V., 2006, Decreasing magmatic footprints of individual volcanoes in a waning basaltic field: Geophysical Research Letters, v. 33, L14305, doi:10.1029/2006GL026743.

Valentine, G.A., and Perry, F.V., 2007, Tectonically controlled, time-predictable basaltic volcanism from a lithospheric mantle source (central Basin and Range Province, USA): Earth and Planetary Science Letters, v. 261, p. 201–216, doi:10.1016/j.epsl.2007.06.029.

Valentine, G.A., and Perry, F.V., 2009, Volcanic risk assessment at Yucca Mountain, NV, USA: Integration of geophysics, geology, and modeling, *in* Connor, C., et al., eds., Volcanism, Tectonism, and Siting Nuclear Facilities: Cambridge, Cambridge University Press, p. 452–480, doi:10.1017/CBO9780511635380.020.

Valentine, G.A., and White, J.D.L., 2012, Revised conceptual model for maar-diatremes: Subsurface processes, energetics, and eruptive products: Geology, v. 40, p. 1111–1114, doi:10.1130/G33411.1.

Valentine, G.A., Perry, F.V., Krier, D., Keating, G.N., Kelley, R.E., and Cogbill, A.H., 2006, Small-volume basaltic volcanoes: Eruptive products and processes, and post-eruptive geomorphic evolution in Crater Flat (Pleistocene), southern Nevada: Geological Society of America Bulletin, v. 118, p. 1313–1330, doi:10.1130/B25956.1.

Valentine, G.A., Krier, D.J., Perry, F.V., and Heiken, G., 2007, Eruptive and geomorphic processes at the Lathrop Wells scoria cone volcano: Journal of Volcanology and Geothermal Research, v. 161, p. 57–80, doi:10.1016/j.jvolgeores.2006.11.003.

Valentine, G.A., Shufelt, N.L., and Hintz, A.R.L., 2011, Models of maar volcanoes, Lunar Crater (Nevada, USA): Bulletin of Volcanology, v. 73, p. 753–765, doi:10.1007/s00445-011-0451-6.

Valentine, G.A., Graettinger, A.H., and Sonder, I., 2014, Explosion depths for phreatomagmatic eruptions: Geophysical Research Letters, v. 41, p. 3045–3051, doi:10.1002/2014GL060096.

Valentine, G.A., Graettinger, A.H., Macorps, E., Ross, P.-S., White, J.D.L., Döhring, E., and Sonder, I., 2015, Experiments with vertically and laterally migrating subsurface explosions with applications to the geology of phreatomagmatic and hydrothermal explosion craters and diatremes: Bulletin of Volcanology, v. 77, 15, doi:10.1007/s00445-015-0901-7.

van Otterloo, J., Cas, R.A.F., and Sheard, M.J., 2013, Eruption processes and deposit characteristics at the monogenetic Mt. Gambier Volcanic Complex, SE Australia: Implications for alternating magmatic and phreatomagmatic activity: Bulletin of Volcanology, v. 75, 737, doi:10.1007/s00445-013-0737-y.

van Wyk de Vries, B., Máquez, A., Herrera, R., Granja Bruña, J.L., Llanes, P., and Delcamp, A., 2014, Craters of elevation revisited: Forced-folds, bulging and uplift of volcanoes: Bulletin of Volcanology, v. 76, 875, doi:10.1007/s00445-014-0875-x.

Wells, S.G., Dohrenwend, J.C., McFadden, L.D., Turrin, B.D., and Mahrer, K.D., 1985, Late Cenozoic landscape evolution on lava flow surfaces of the Cima volcanic field, Mojave Desert, California: Geological Society of America Bulletin, v. 96, p. 1518–1529, doi:10.1130/0016-7606(1985)96<1518:LCLEOL>2.0.CO;2.

West, M., Ni, J., Baldridge, W.S., Wilson, D., Aster, R., Gao, W., and Grand, S., 2004, Crust and upper mantle shear wave structure of the southwest United States: Implications for rifting and support for high elevation: Journal of Geophysical Research, v. 109, B03309, doi:10.1029/2003JB002575.

White, J.D.L., and Houghton, B.F., 2006, Primary volcaniclastic rocks: Geology, v. 34, p. 677–680, doi:10.1130/G22346.1.

White, J.D.L., and Ross, P.-S., 2011, Maar-diatreme volcanoes: A review: Journal of Volcanology and Geothermal Research, v. 201, p. 1–29, doi:10.1016/j.jvolgeores.2011.01.010.

White, S.M., Crisp, J.A., and Spera, F.J., 2006, Long-term volumetric eruption rates and magma budgets: Geochemistry, Geophysics, Geosystems, v. 7, Q03010, doi:10.1029/2005GC001002.

Winograd, I.J., Landwehr, J.M., Ludwig, K.R., Coplen, T.B., and Riggs, A.C., 1997, Duration and structure of the past four interglaciations: Quaternary Research, v. 48, p. 141–154, doi:10.1006/qres.1997.1918.

Witt-Eickschen, G., and Kramm, U., 1998, Evidence for multiple stage evolution of the subcontinental lithospheric mantle beneath the Eifel (Germany) from pyroxenite and composite pyroxenite/peridotites xenoliths: Contributions to Mineralogy and Petrology, v. 131, p. 258–272, doi:10.1007/s004100050392.

Wood, C.A., 1980, Morphometric evolution of cinder cones: Journal of Volcanology and Geothermal Research, v. 7, p. 387–413, doi:10.1016/0377-0273(80)90040-2.

Wörner, G., Zindler, A., Staudigel, H., and Schmincke, H.-U., 1986, Sr, Nd, and Pb isotope geochemistry of Tertiary and Quaternary alkaline volcanics from West Germany: Earth and Planetary Science Letters, v. 79, p. 107–119, doi:10.1016/0012-821X(86)90044-0.

Yogodzinski, G.M., Naumann, T.R., Smith, E.I., Bradshaw, T.K., and Walker, J.D., 1996, Evolution of a mafic volcanic field in the central Great Basin, south central Nevada: Journal of Geophysical Research, v. 101, p. 17,425–17,445, doi:10.1029/96JB00816.

Zoback, M.L., Anderson, R.E., and Thompson, G.A., 1981, Cainozoic evolution of the state of stress and style of tectonism of the Basin and Range province of the western United States: Royal Society of London Philosophical Transactions, ser. A, v. 300, p. 407–434, doi:10.1098/rsta.1981.0073.